

Ionic Liquid Based Field Effect Studies on $\text{La}_{2-x}\text{Sr}_x\text{CuO}_4$ Films and Related Materials

THÈSE N° 6133 (2014)

PRÉSENTÉE LE 27 MARS 2014

À LA FACULTÉ DES SCIENCES DE BASE
LABORATOIRE DE PHYSIQUE DE LA MATIÈRE COMPLEXE
PROGRAMME DOCTORAL EN PHYSIQUE

ÉCOLE POLYTECHNIQUE FÉDÉRALE DE LAUSANNE

POUR L'OBTENTION DU GRADE DE DOCTEUR ÈS SCIENCES

PAR

Guy Joseph Günter DUBUIS

acceptée sur proposition du jury:

Prof. F. Mila, président du jury
Prof. D. Pavuna, Prof. I. Božović, directeurs de thèse
Prof. N. Barišić, rapporteur
Prof. M. Gioni, rapporteur
Prof. J.-M. Triscone, rapporteur



ÉCOLE POLYTECHNIQUE
FÉDÉRALE DE LAUSANNE

Suisse
2014

Our greatest weakness lies in giving up.
The most certain way to succeed is always
to try just one more time.
—Thomas A. Edison

This thesis is dedicated to my parents. . .
(and to the future discoverer of room temperature superconductivity!)

Acknowledgements

I would like to thank my colleagues at Brookhaven National Laboratory who through numerous discussions and help in the laboratory made my work possible: Dr. Adrian Gozar, Dr. Juan Pereiro, Dr. Jie Wu, Dr. Joonah Yoon, Nicholas Litombe, Dr. Oshri Pelleg, Dr. Jure Strle, Dr. Xiang Leng, Dr. Yujie Sun, Federico Baiutti, Fran Loeb. . . The work done at the Advance Photon Source is the result of a collaboration with Dr. Ronald Pindak, Prof. Yizhak Yacoby and Dr. Hua Zhou. Stimulating discussion with Prof. László Forró and numerous colleagues at EPFL are also acknowledged.

A special thanks to Dr. Anthony Bollinger who was heavily involved in this project and always there to answer my questions. He was also responsible of the lithography of the samples we used. Finally, a particular warm thank you to both my co-advisers Prof. Ivan Božović, BNL and Prof. Davor Pavuna, EPFL. They made this work possible through shared ideas, visions and discussions.

I also would like to acknowledge Prof. Jean-Marc Triscone, Prof. Neven Barišić, Prof. Marco Grioni and Prof. Frédéric Mila for accepting to review and examine my doctoral thesis.

Thanks to Noelia Cotón Sánchez et Davide Innocenti for critical reading of the manuscript.

This work was supported by the Laboratory of Complex Matter - EPFL, and the Swiss National Science Foundation. Work at Brookhaven National Laboratory was made possible by the generous support of the US Department of Energy.

Lausanne, December 2013

G. D.

Abstract

The motivation of my thesis work was to develop a new approach that should ideally enable us to avoid the intrinsic disorder while researching novel superconducting materials. To this end I combined state of the art growth of ultra-thin superconducting cuprate films with advances made in a different field, electric energy storage, where supercapacitors have recently made tremendous progress. One of their key components are ionic liquids (IL), molten organic salts that allow for much higher induced charge densities than previously possible. Using novel Electric Double Layer Gating (EDLG) methods, I have first developed a laboratory method of sample sandwich preparation, as well as materials characterisation and transport measurements. Subsequently, I demonstrated the electric field effect on a single CuO_2 plane in $\text{La}_{2-x}\text{Sr}_x\text{CuO}_4$ grown by Molecular Beam Epitaxy (MBE). I succeeded in continuously driving it from insulator to superconductor by slowly and reversibly inducing large electric fields at the interface with the IL and consequent changes in the carrier density.

While the idea of using field effect to probe the properties of superconductors was not new, the EDLG gave us the ability to perform it on a much larger scale than was possible earlier. We measured shifts in critical temperature, T_c , up to 30K. Rescaling allowed us to replot whole sequences of measurements onto a single function, as expected for a two-dimensional (2D) Superconductor-to-Insulator Transition (SIT). This resulted in a curve that showed a critical point at the quantum resistance for pairs of $6.45\text{k}\Omega$. The evidence from preliminary scaling analysis implies a phase transition driven by quantum phase fluctuations, and Cooper pair (de)localization. However, further experiments at lower temperatures are needed to strengthen this finding.

Abstract

Specifically, our key findings are:

1. The EDLG technique was successfully adapted to high- T_c cuprates, and specifically to $\text{La}_{2-x}\text{Sr}_x\text{CuO}_4$ thin films grown by MBE.
2. Shifts in T_c of up to 30 K were induced in these $\text{La}_{2-x}\text{Sr}_x\text{CuO}_4$ films, reversibly driving their state from insulator to superconductor. This allowed preliminary scaling studies that should be extended to lower temperatures.
3. We have seen evidence of a quantum critical point at the underdoped end of the superconducting dome where we observe the quantum resistance for pairs: $R_Q = \frac{h}{(2e)^2} = 6.45 \text{ k}\Omega$. Similar values have been measured independently by other groups.
4. We extended our studies to other quasi-2D systems: graphene, WO_3 , diamond, $\text{FeTe}\dots$ and these studies are still very much in progress. However, they already allowed us to make a tremendous progress in understanding the subtleties on how to apply EDLG to a variety of samples, and how to make high quality contacts. This also resulted in several improvements of experimental setups that significantly ease further research.
5. We have also developed a method to apply Coherent Bragg Rod Analysis (COBRA) to our MBE grown $\text{La}_{2-x}\text{Sr}_x\text{CuO}_4$ samples while they are exposed to EDLG. This should eventually allow us to directly determine the effect of EDLG on the $\text{La}_{2-x}\text{Sr}_x\text{CuO}_4$ crystalline structure. Initial results are promising and experiments are still ongoing.

As is often the case in research, our results opened a multitude of new questions, and thus I conclude my thesis with some proposed further work.

Keywords : Superconductivity, cuprate, $\text{La}_{2-x}\text{Sr}_x\text{CuO}_4$ thin film, molecular beam epitaxy, field effect, ionic liquid gating, quantum critical point, scaling, shift in T_c

Résumé

La motivation de mon travail de thèse était de développer une nouvelle approche permettant idéalement d'étudier les matériaux supraconducteurs tout en dépassant les effets du désordre qui leur est inhérent. Pour cela, j'ai combiné les progrès faits en croissance de couches ultra-minces des cuprates avec les avancées faites dans un champ différent, le stockage d'énergie, où les supercondensateurs en particulier ont évolué de façon remarquable récemment. Un de leurs ingrédients clés sont les liquides ioniques, des sels organiques liquides à température ambiante permettant d'induire des densités de charges nettement plus importantes que ce qui était possible auparavant. J'ai premièrement développé les techniques de laboratoire pour l'application à des échantillons en couches minces de l'architecture novatrice du gating par double couches électriques (Electric Double Layer Gating, EDLG). Par la suite, j'ai démontré l'effet de champ sur un simple plan de CuO_2 dans une couche mince de $\text{La}_{2-x}\text{Sr}_x\text{CuO}_4$ créée par jet moléculaire (Molecular Beam Epitaxy, MBE), le poussant, de manière continue, contrôlée et réversible, d'isolant à supraconducteur. Tout cela en contrôlant précisément la densité surfacique de charge induite par effet de champ sur l'échantillon à son interface avec le liquide ionique.

L'idée d'utiliser l'effet de champ pour étudier les propriétés de matériaux supraconducteurs n'est pas nouvelle en soi, mais la technique de l'EDLG nous permet maintenant d'induire des changements d'une amplitude qui n'était pas possible dans le cas d'expériences antérieures. Nous avons observé des décalages de température critique, T_c , atteignant jusqu'à 30 K. Une renormalisation de ces courbes résulte en une fonction unique, comme attendu pour une transition supraconducteur-isolant en 2D. La courbe résultante met en évidence un point critique à la résistance quantique de paires, $6.45 \text{ k}\Omega$. Cela suggère que l'on a affaire à une transition de phase entraînée par des fluctuations de champs quantiques, et une possible (dé)localisation de paires de Cooper. Mais des expériences complémentaires à plus basse température sont nécessaires afin de confirmer cette conclusion.

Voici les résultats principaux de cette thèse :

1. La technique EDLG a été adaptée avec succès aux cuprates supraconducteurs à haute température critique, en particulier à des couches minces de $\text{La}_{2-x}\text{Sr}_x\text{CuO}_4$ créées par épitaxie par MBE.
2. Des décalages de T_c jusqu'à 30K ont été induits dans ces films de $\text{La}_{2-x}\text{Sr}_x\text{CuO}_4$, en poussant leur état de manière réversible d'isolant à supraconducteur. Cela a permis une étude préliminaire de renormalisation, qui devrait être étendue à des températures plus basses.
3. Nous avons observé des indices d'une présence d'un point critique à l'extrémité sous-dopée du dôme supraconducteur, où nous observons la résistance quantique de paires $R_Q = \frac{h}{(2e)^2} = 6.45\text{k}\Omega$. Des valeurs similaires ont été mesurées indépendamment par d'autres groupes.
4. Par la suite, nous avons étendu nos études à d'autres matériaux quasi-2D : graphène, WO_3 , diamant, FeTe. . . Ces mesures sont encore en cours. Néanmoins, ces expériences nous ont déjà fait faire d'important progrès dans notre compréhension des subtilités de l'application de l'EDLG à une variété de matériaux. De plus, cela nous a permis d'améliorer nos installations expérimentales, ce qui facilitera grandement les futures recherches.
5. Finalement, nous avons développé une méthode pour appliquer la Coherent Bragg Rod Analysis (COBRA) sur nos échantillons de $\text{La}_{2-x}\text{Sr}_x\text{CuO}_4$ pendant leur exposition au EDLG. Cela devrait nous permettre de mesurer directement les effets sur la structure cristalline de $\text{La}_{2-x}\text{Sr}_x\text{CuO}_4$ du EDLG. Les résultats initiaux sont prometteurs, mais ces expériences sont encore en cours.

Comme cela est souvent le cas en recherche, nos résultats posent une multitude de nouvelles questions. Pour cette raison, je conclus cette thèse par quelques suggestions de direction de recherche à approfondir dans le futur.

Mots-clés : Supraconductivité, cuprate, couches minces de $\text{La}_{2-x}\text{Sr}_x\text{CuO}_4$, épitaxie par jet moléculaire, effet de champ, liquide ionique, point critique, renormalisation, décalage de T_c

Zusammenfassung

Die Motivation meiner Dissertation war die Entwicklung eines neuen Ansatzes zur Erforschung supraleitender Materialien zu entwickeln, der uns im Idealfall erlauben wird denen inhärente Unordnung zu umgehen. Um dies zu erreichen habe ich Fortschritte im Bereich des Wachstums ultra-dünnschichtiger Cuprat-Supraleiter mit solchen aus einem völlig unterschiedlichem Feld, dem der Energiespeicherung, kombiniert. In letzterem hat sich die Superkondensatoren-Technologie gewaltig entwickelt. Einer Schlüsselkomponenten sind dabei ionische Flüssigkeiten, d.h. geschmolzene organische Salze, die es erlauben viel höhere Ladungsdichten zu erzeugen als dies vorher möglich war. Mit der neuen Methode des Electric Double Layer Gating (EDLG) habe ich zuerst Labormethoden zur Vorbereitung, sowie Charakterisierung der Elektronischen Transporteigenschaften unserer Proben entwickelt. Danach habe ich den elektrischen Feldeffekt auf einer einzelnen CuO_2 Ebene in mittels Molecular Beam Epitaxy (MBE) gezüchtetem $\text{La}_{2-x}\text{Sr}_x\text{CuO}_4$ demonstriert. Es gelang mir dieses stufenlos von Isolator zu Supraleiter zu treiben, indem ich langsam und reversibel einen grossen elektrischen Feldeffekt an der Grenzfläche mit der ionischen Flüssigkeit, und somit auch Änderungen in der Ladungsträgerdichte, erzeugte.

Die Idee den Feldeffekt zur Untersuchung der Eigenschaften von Supraleitern zu benutzen ist nicht neu, aber EDLG erlaubt es uns dies auf einer deutlich grösseren Skala zu tun, als es früher möglich war. Wir haben Verschiebungen der kritischen Temperatur T_c um bis zu 30K gemessen. Maßstabsänderungen erlaubten es ganze Messungssequenzen auf einer einzelnen Funktion darzustellen, wie es von einem 2D Supraleiter zu Isolator Phasenübergang erwartet wird. Diese Kurve zeigte einen kritischen Punkt bei dem Quantenwiderstand für Paare, $6.45\text{k}\Omega$. Diese Erkenntnis erster Skalierungsanalysen legt nahe, dass es sich hier um einen Quanten Phasenübergang getrieben von Quanten Phasen Fluktuationen, und Cooper Paare (De-)Lokalisierung handelt. Aber weitere Experimente bei tieferen Temperaturen sind nötig, um diese Ergebnis zu untermauern.

Die Schlüsselerkenntnisse dieser Dissertation sind :

1. Die EDLG-Technik wurde erfolgreich auf Cuprat-Hochtemperatursupraleiter angewandt, namentlich auf mittels MBE gezüchteten $\text{La}_{2-x}\text{Sr}_x\text{CuO}_4$ Dünnschichten.
2. Verschiebungen von T_c um bis zu 30K wurden in diesen $\text{La}_{2-x}\text{Sr}_x\text{CuO}_4$ Dünnschichten erzeugt. Dadurch wurden diese vom Isolator- zum Supraleiterzustand getrieben. Dies erlaubte erste Skalierungsstudien, die aber auf tiefere Temperaturen ausgeweitet werden sollten.
3. Es gibt Hinweise für einen quantenkritischen Punkt am unteren Ende des supraleitenden Doms, wo wir den Kollaps nahe des Quantenwiderstands für Paare $R_Q = \frac{h}{(2e)^2} = 6.45\text{k}\Omega$ beobachten konnten. Ähnliche Werte wurden unabhängig durch andere Forschungsgruppen gemessen.
4. Danach erforschten wir einige andere Quasi-2D Systeme: Graphene, WO_3 , Diamant, FeTe. . . Diese Studien sind noch in Gange. Sie haben uns jedoch schon jetzt erlaubt, ein viel klareres Verständniss der Feinheiten in der Anwendung von EDLG zu entwickeln. Dies führte auch zur Verbesserung von Versuchsanordnungen die uns die weitere Forschung erleichtern werden.
5. Des Weiteren haben wir eine Methode entwickelt, um Coherent Bragg Rod Analysis (COBRA) an unseren $\text{La}_{2-x}\text{Sr}_x\text{CuO}_4$ Filmen zu messen, während sie dem EDLG ausgesetzt sind. Diese sollte es erlauben, direkt den Effekt von EDLG auf deren Kristallstruktur zu bestimmen. Erste Messungen sind vielversprechend, jedoch sind diese Experimente noch nicht abgeschlossen.

Wie es oft der Fall in der Forschung ist, regen unsere Resultate eine Vielfalt an neuen Fragen an. Daher schliesse ich diese Dissertation mit einigen Vorschlägen für weitere Experimente.

Stichwörter : Supraleitung, Cuprat-Supraleiter, $\text{La}_{2-x}\text{Sr}_x\text{CuO}_4$ Dünnschichten, Molecular Beam Epitaxy, Feldeffekt, ionische Flüssigkeiten, Quantenkritischer Punkt, Verschiebung von T_c

Contents

Acknowledgements	v
Abstract (English/Français/Deutsch)	vii
List of Figures	xv
List of Tables	xvii
List of Symbols and Abbreviations	xix
1 Introduction and Background	1
1.1 Basics on Superconductivity	1
1.1.1 Specifics of High- T_c Cuprates	3
1.2 The $\text{La}_{2-x}\text{Sr}_x\text{CuO}_4$ Cuprates	4
1.3 On the Electric Field Effect	6
1.3.1 Classical MISFET Architecture	6
1.3.2 The Electrical Double Layer Concept	7
1.3.3 Dielectric Gating Applied to Other Systems	10
2 Experimental Section	13
2.1 On Molecular Beam Epitaxy of Cuprate Films	13
2.2 Experimental Measurements	15
2.2.1 Transport Measurement Setup	15
2.2.2 Magnetic Susceptibility Measurements	16
2.2.3 Automation of Transport Measurements	16
2.2.4 EDLG Sample Preparation	18
2.2.5 The Contact Challenge	23
2.2.6 Dielectric Gating Procedure	24
2.2.7 Summary on Dielectric Gating	28

Contents

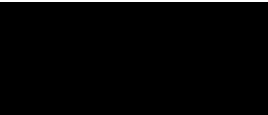
3	Field Effect Results	31
3.1	Field Effect on Underdoped $\text{La}_{2-x}\text{Sr}_x\text{CuO}_4$	31
3.1.1	Magnetic Susceptibility and EDLG	36
3.1.2	Alternative Determination of the Critical Exponents $z\nu$	37
3.2	Field Effect on Overdoped $\text{La}_{2-x}\text{Sr}_x\text{CuO}_4$	38
4	Discussion	39
4.1	Experimental Challenges	39
4.2	On Thin Film Studies by Other Groups	41
4.3	On Single Crystal Studies by Other Groups	44
4.4	Concluding Remarks and Outlook	45
5	Other Explored Avenues	47
5.1	Low Temperature Measurements	47
5.2	Field Effect on other Materials, Illustrated by WO_3	48
5.2.1	On WO_3 Sample Preparation	48
5.2.2	Transport Results	50
5.2.3	Discussion	51
5.3	Differential COBRA	52
5.3.1	Wet Chemical Sample Cell	52
5.3.2	Experimental Procedure	55
5.3.3	Concluding Remarks	60
6	Conclusions and Outlook	63
6.1	Conclusions	63
6.2	Outlook for Future Studies	64
A	Ultra-Stabilization of a Cryocooler	67
A.1	Technical Realization	69
A.2	Experimental Results	72
A.3	Conclusion	73
B	Wet Chemical Cell: Drawings	77
	Bibliography	93
	Photographic Credits	94
	Curriculum Vitae	97

List of Figures

1.1	Timeline of discovery of superconductors.	2
1.2	Major electrical resistivity models in 1900.	2
1.3	$\text{La}_{2-x}\text{Sr}_x\text{CuO}_4$ crystal structure.	4
1.4	Schematic electronic phase diagram of $\text{La}_{2-x}\text{Sr}_x\text{CuO}_4$	5
1.5	Record T_c in $\text{La}_{2-x}\text{Sr}_x\text{CuO}_4$	5
1.6	Behaviour of correlated materials in relation to sheet carrier density. . . .	6
1.7	Schematic view of a MISFET transistor.	7
1.8	Solvation force profile on mica.	8
1.9	Solvation force profile on Au(111).	9
2.1	AFM of typical sample.	13
2.2	Oxide MBE system.	14
2.3	RHEED of typical sample.	14
2.4	Transport measurement setup.	15
2.5	Typical thermal cycling.	17
2.6	Lithographic patterns 1.	19
2.7	Lithographic patterns 2.	20
2.8	Lithographic patterns 3.	21
2.9	Device numbering convention.	21
2.10	Example of various devices with IL.	22
2.11	Contact damage due to EDLG.	24
2.12	Device covered by IL.	25
2.13	Typical charging behaviour of a device.	26
2.14	Effect of charging at various charging temperatures.	26
3.1	Schematic view of $\text{La}_{2-x}\text{Sr}_x\text{CuO}_4$ film.	32
3.2	Tuning of resistivity through field effect.	34
3.3	Critical point in $\text{La}_{2-x}\text{Sr}_x\text{CuO}_4$	35
3.4	Collapse around the critical point.	35
3.5	Magnetic susceptibility.	36
3.6	Alternative vz analysis.	37
3.7	Field effect on overdoped $\text{La}_{2-x}\text{Sr}_x\text{CuO}_4$	38

List of Figures

4.1	SIT in $\text{YBa}_2(\text{Cu}_{1-x}\text{Zn}_x)_3\text{O}_{7-\delta}$	42
4.2	SIT in $\text{YBa}_2\text{Cu}_3\text{O}_{7-\delta}$ thin films.	43
4.3	SIT in $\text{Bi}_2\text{Sr}_2\text{Y}_x\text{Ca}_{1-x}\text{Cu}_2\text{O}_8$	43
4.4	SIT in $\text{YBa}_2\text{Cu}_3\text{O}_{7-\delta}$ single crystals.	45
5.1	Diced sample on miniaturised sample holder.	48
5.2	Sputtering setup.	49
5.3	Picture of WO_3 nanowire device.	50
5.4	WO_3 transport measurements.	51
5.5	COBRA sample installed, first beamtime.	53
5.6	Beam damage.	54
5.7	3D rendering of wet chemical sample cell for X-ray.	56
5.8	Wet chemical sample cell.	57
5.9	Wet chemical sample cell (Detail).	58
5.10	Beam damage.	58
5.11	Differential COBRA preliminary results.	60
A.1	Engineering drawing of the damper.	70
A.2	3D rendering of the damping device.	71
A.3	Stabilization device installed on cryocooler.	71
A.4	Temperature oscillation envelope.	72
A.5	Cooling behaviour of the stabilized cryocooler.	73
A.6	Effect of stabilization on ramping.	74
A.7	Damping of temperature oscillations $T \leq 10\text{ K}$	75
A.8	Damping of temperature oscillations $10\text{ K} < T \leq 50\text{ K}$	76
B.1	Wet chemical cell (central part).	78
B.2	Wet chemical cell (backing plate).	79
B.3	Wet chemical cell (washer).	80



List of Tables

1.1	Materials studied using dielectric gating.	11
2.1	List of gate dielectrics used.	27

List of Symbols & Abbreviations

AC	Alternating Current
AF	Antiferromagnetic
AFM	Atomic Force Microscopy
APS	Advanced Photon Source
ARPES	Angle-Resolved Photoemission
BCS	Bardeen, Cooper & Schrieffer Theory
BNL	Brookhaven National Laboratory
COBRA	Coherent Bragg Rod Analysis
2Δ	Superconducting Energy Gap
DEME-TFSI	N,N-diethyl-N-methyl-N-(2-methoxyethyl)ammonium bis (trifluoromethylsulphonyl)imide
e	Electron, or Charge of the Electron
EDL	Electric Double Layer
EDLG	Electric Double Layer Gating
EDLT	Electric Double Layer Transistor
FET	Field Effect Transistor
FM	Ferromagnetic
FQHE	Fractional Quantum Hall Effect
GM	Gifford-McMahon
\hbar	Reduced Planck Constant
I	Insulator
IL	Ionic Liquid
I_G	Gate Current
m	Mass
M	Metal
MBE	Molecular Beam Epitaxy
MISFET	Metal–Insulator–Semiconductor Field-Effect Transistor
n	Carrier Concentration
n_{\square}	Sheet Carrier Concentration
OCP	Open Circuit Potential
OP	Optimally Doped
PEG-NaF	Sodium Fluoride salt dissolved in Polyethylene Glycol
PCB	Printed Circuit Board

Symbols & Abbreviations

Q2D	Quasi-Two-Dimensional
QPT	Quantum Phase Transition
R_{\square}	Resistance per Square
R_c	Critical Resistance
RHEED	Reflection High Energy Electron Diffraction
R_Q	Quantum Resistance
SC	Superconductivity
SIT	Superconductor-to-Insulator Transition
T_c	Superconducting Critical Temperature
T_{charge}	Charging Temperature
UC	Unit Cell
V_g	Gate Voltage
x	usually used for Carrier Concentration

1 Introduction and Background

1.1 Basics on Superconductivity

Since its discovery in mercury in 1911 by H. Kamerlingh Onnes, superconductivity has occupied many minds and dreams. More than half a century after this original discovery, superconductivity was still a phenomenon limited to low temperatures, with a record T_c of 23K in Nb_3Ge reached in 1973.[6, 7] It was only with the discovery in 1986 of the new family of cuprate superconductors that significantly higher T_c were achieved. (See figure 1.1) However, even now, more than a century after the initial discovery, this quantum phenomenon still leaves many open questions. For example, in 2006 yet another completely new family of superconductors was discovered: iron pnictides.[8] This was especially remarkable as up to then it had been generally considered that magnetic elements such as iron would be detrimental to superconductivity. While these materials did not yet reach higher T_c than what has been possible within the cuprate family, they will prove themselves invaluable in finally trying to understand the underlying phenomenon of unconventional superconductivity.

Superconductivity is above all defined by two properties. First of all, zero-resistivity, or as Kammerlingh Onnes described in his original experiment “near-enough nul.”[9] At the time of the original discovery, this was something no theory had predicted. (See figure 1.2) In 1900, leading researchers like Lord Kelvin considered that the resistance would go to infinity at 0K, i.e. a perfect insulator. Matthiessen correctly assumed that impurities will determine the residual resistivity of typical normal metals at 0K, while Dewar at Cambridge expected perfect normal conductivity of electrons. (See figure 1.2) The second distinguishing characteristic is perfect diamagnetism. This was discovered by Meissner and Ochsenfel in 1933[10], and is now named after its discoverers. They observed that when a cylinder of superconducting material such as tin or lead is introduced into a homogeneous magnetic field, above T_c , the field lines can cross without any major distortion through the cylinder. But when the sample is cooled below T_c the field lines are severely perturbed, and the field is expelled from the superconductor. This effect has

Chapter 1. Introduction and Background

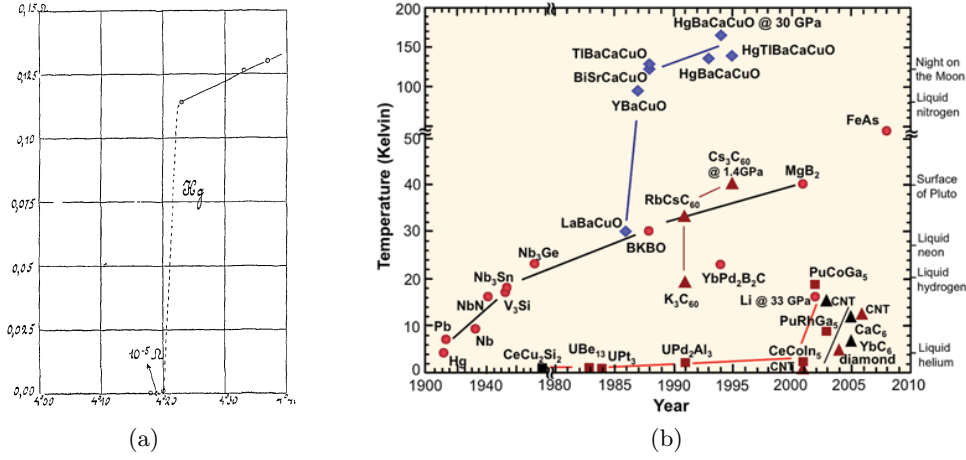


Figure 1.1 – (a) Original discovery of superconductivity in Hg; reproduced from [11]. Copyright 1912 by Royal Netherlands Academy of Arts and Sciences
(b) Timeline of the discovery of superconductors. Reproduced from Wikipedia.

been made popular by related levitation experiments, with the biggest being the creation of a maglev train based on this effect in Japan.

It was a difficult task for theoretical physicists to come up with models that would explain superconductivity. Namely it is a very subtle cooperative quantum phenomenon in many body physics, within often complex materials.

Inspired by the Meissner-Ochsenfeld effect, the brothers F. and H. London proposed a first phenomenological model in 1935.[12] The subsequent very successful phenomenological approach was proposed by V. Ginzburg and L. Landau in 1950. This approach was able to explain the phenomenology of many superconducting materials, but left the origin of superconductivity unexplained.

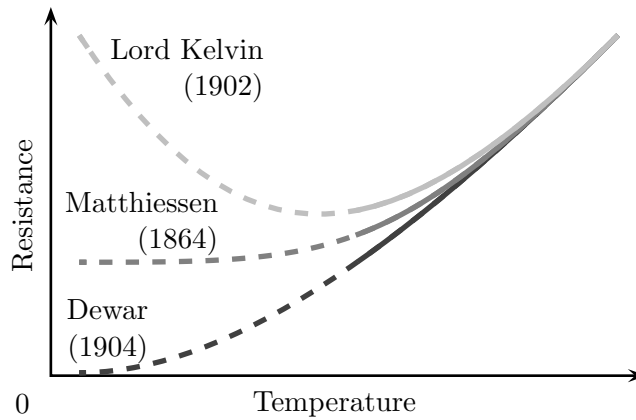


Figure 1.2 – Major electrical resistivity models in 1900.

Finally in 1957, the BCS theory by J. Bardeen, L. Cooper and R. Schrieffer emerged.[13] This theory succeeded remarkably to explain conventional superconductivity from a microscopic point of view. Its major breakthrough was to take into account the attraction between electrons in many body electron liquids. Cooling the superconducting material below T_c leads to pairing of electrons to *Cooper pairs* and to condensation into the superconducting state. The binding energy of the Cooper pairs represents the energy gap 2Δ , at the Fermi level in the superconducting state. It must be noted that in this gap, no single particle states are possible in the superconducting state. Contrary to the normal state, in the superconducting state, all pairs move coherently and are described by a single wave function:

$$\psi = |\psi|e^{i\varphi} \tag{1.1}$$

with the density of superconducting electrons given by $n_s = |\psi|^2$ and $\varphi = \varphi(\vec{r})$ being a spatially varying phase.

The main implication of this single wave function is that Cooper pairs can not be scattered by impurities in the material, and thus the resistivity of the material is null. The BCS theory was very successful in explaining the characteristic properties of most known superconducting materials at the time of its introduction, and even today it is our reference theory for superconductivity.

Today, there are numerous theories and models for high- T_c superconductors, but none is yet generally accepted. However, it is important to note that there is also the concept of Bose-Einstein condensation, in which pairs can exist in real space, and even extension models of bipolaronic superconductivity. At present, there are still a lot of challenges for theory, as we will also see in this thesis: see chapter 3. Namely, it is very difficult to include into one theory all the striking phenomena that we experimentally measure in the laboratory.

1.1.1 Specifics of High- T_c Cuprates

High- T_c cuprates differ from low T_c or conventional superconductors in a few key points. Firstly, conventional superconductors are usually reasonably metallic materials, while the undoped high- T_c cuprates are in general stable insulators, actually ceramics. Furthermore in conventional superconductors, the pairing mechanism exhibits a *s*-wave pairing symmetry, while the hole doped cuprates possess a *d*-wave symmetry. Cuprates can be considered quasi-two-dimensional (Q2D) materials, as superconductivity takes place in the CuO_2 layer. This layer is neighboured by a charge reservoir layer that stabilises the structure and dopes electrons or holes into the CuO_2 layer.

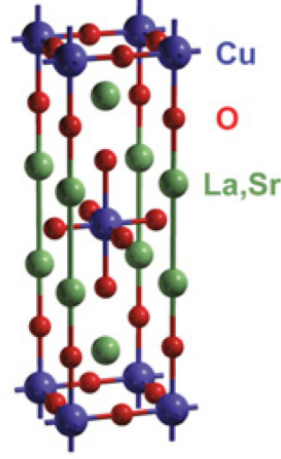


Figure 1.3 – $\text{La}_{2-x}\text{Sr}_x\text{CuO}_4$ crystal structure. Adapted from Barišić *et al.* [14].

1.2 The $\text{La}_{2-x}\text{Sr}_x\text{CuO}_4$ Cuprates

In this thesis, we focused mainly on $\text{La}_{2-x}\text{Sr}_x\text{CuO}_4$ thin films. This is one of the first high- T_c superconductors discovered in 1986. One of the reasons to focus on this material, is that the Oxide MBE group at BNL has refined its thin film growth.[2] This gives us access to a good set of samples. This material possesses a relatively simple structure compared to other cuprates as it contains only a single CuO_2 plane surrounded by charge reservoirs. Doping it by replacing La with Sr allows to change the carrier density. Alternatively, interstitial oxygen also has a doping effect, but for the sake of simplicity, our work focused on samples where interstitial oxygen was avoided, or at least limited, through careful annealing procedures after the sample growth.

In the case of bulk $\text{La}_{2-x}\text{Sr}_x\text{CuO}_4$, the highest T_c , 38K is reached under optimal doping (OP) with $x \approx 0.16$. Superconductivity is limited to a Sr-doping range from $x \sim 0.06$ to $x \sim 0.25$. (See figure 1.4) The undoped compound La_2CuO_4 is antiferromagnetic (AF), with a charge of $n = 1$ hole per copper atom. By replacing La^{3+} by Sr^{2+} during doping, a hole is induced in the CuO_2 plane thus for a given doping x the charge density in the CuO_2 plane is $n = 1 + x$ per unit cell (UC). The critical temperature T_c can be pushed to 51.5K in these films under epitaxial strain. (See figure 1.5)

As we can see in the electronic phase diagram (See figure 1.4), the typical undoped cuprate is an antiferromagnetic insulator that only by doping eventually becomes a superconductor and develops the characteristic dome. Obviously, there are many other striking complexities in the non-superconducting state, yet these are not the focus of this thesis.

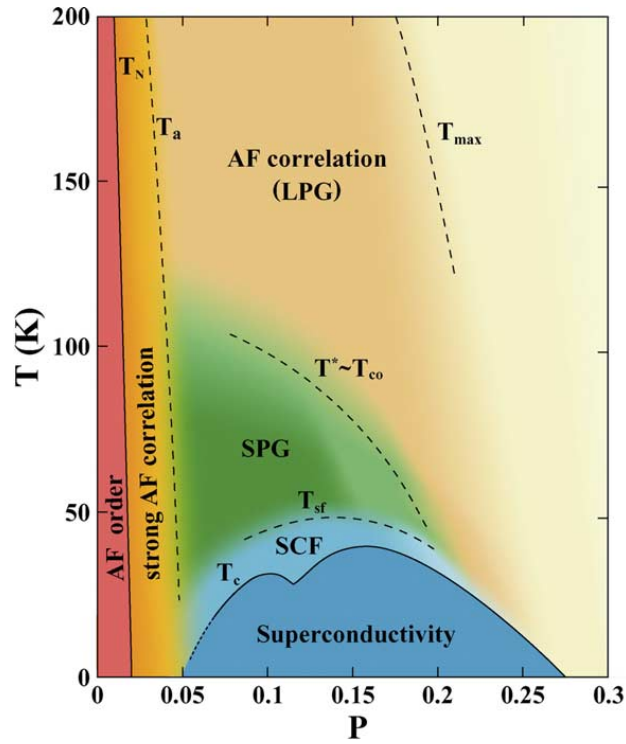


Figure 1.4 – Schematic electronic phase diagram of $\text{La}_{2-x}\text{Sr}_x\text{CuO}_4$. Reprinted from Journal of Physics and Chemistry of Solids 65 (2004), Oda *et al.* 1381–1390, [15]. Copyright 2004, with permission from Elsevier.

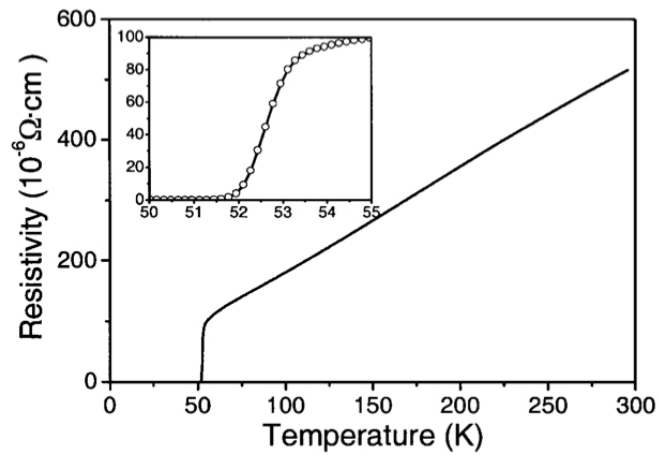


Figure 1.5 – Record $T_c = 51.5\text{K}$ for $\text{La}_{2-x}\text{Sr}_x\text{CuO}_4$ films under epitaxial stress. Reprinted from [16]. Copyright 2002 by the American Physical Society.

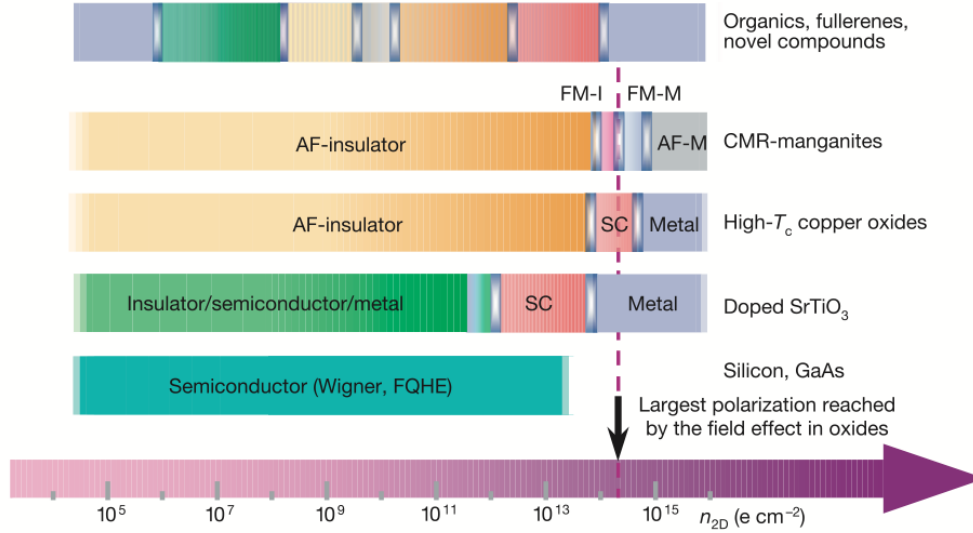


Figure 1.6 – At 0K, correlated materials show a wide variety of behaviours, as function of the sheet carrier density (n_{2D}). Field effect can allow access to these different phases by adjusting the carrier concentration. AF, antiferromagnetic; FM, ferromagnetic; I, insulator; M, metal; SC, superconductor; FQHE, fractional quantum Hall effect; Wigner, Wigner crystal. Reprinted by permission from Macmillan Publishers Ltd: Nature, Ahn *et al.* [17], copyright 2003.

1.3 On the Electric Field Effect

1.3.1 Classical MISFET Architecture

In electronics, the Metal–Insulator–Semiconductor Field-Effect Transistor (MISFET) is one of the most common applications of field effect. After a first patent for a FET filed in 1925 in Canada by J. E. Lilienfeld[18], it took until 1947 for a team from Bell Labs to build the first working transistor. For this work, J. Bardeen, W. H. Brattain and W. B. Shockley received the Nobel Prize in Physics in 1956 “for their researches on semiconductors and their discovery of the transistor effect”.[19] A MISFET is a four-terminal device with a source (S), drain (D), gate (G) and body (B) terminals. It can be implemented as a three-terminal device when the body and the drain are shorted.

A channel of semiconductor material connects the source and drain, and the carrier concentration in this channel is controlled by the voltage applied between the gate and the body. This allows to switch the current between the source and the drain On and Off. An insulator atop of the semiconducting channel avoids any short through the gate. Usually this insulator is an oxide, but different dielectric materials can be used.

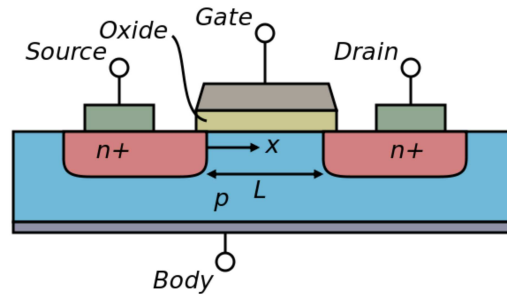


Figure 1.7 – Schematic view of a MISFET transistor. The current flow between source and drain is controlled by a voltage applied to the gate. Source: Wikipedia.

1.3.2 The Electrical Double Layer Concept

When an electrolyte solution touches a solid surface, an electrical double layer (EDL) forms. Just at the surface, a layer of ions is adsorbed due to chemical interaction between the fluid and the solid. To keep the liquid neutral, a second layer of ions of opposite polarity has to arrange itself atop of this first layer. This allows them to electrically shield the first layer. This can go on, with each subsequent layer more loosely attached to the solid surface. The thermal motion in the liquid implies that these layers have to be considered in a similar way to a chemical equilibrium, and not as rigid structures. By applying a voltage between the liquid and the solid, one can modulate the structure in this EDL.

A very early simple model of the EDL was already proposed by Helmholtz in 1853.[20, 21] In this model, he assumes that the layer forms a simple planar capacitor, with the adsorbed ions forming one plane of the capacitor, and the image charges in the solid forming the second plane. This region of the solid where the electrical charge is influenced is referred to as the space charge region.

A further model was introduced by L. Gouy and D. Chapman. In this case, one assumes a semi-infinite diffuse layer where anions and cations are mobile and distributed unequally. This model is not optimal in the case of highly charged layers, and thus it was improved by Stern by combining the Gouy-Chapman Model of a diffused layer with the Helmholtz model of a single more rigid layer. This Gouy-Chapman-Stern model assumes an internal Helmholtz layer (i.e. Stern layer), and an outer diffused Gouy-Chapman layer.

While these classical models are a good help for understanding what happens at the interface, it must be noted that in most cases they assume the solid to be either a metal or a semiconductor. In the case of highly correlated materials such as superconductors, not all results may stay valid.

In the case of IL-metal interface, a simple Gouy-Chapman-Stern model has been presented by K. B. Oldham.[22] This model assumes spherical anions and cations of equal size.

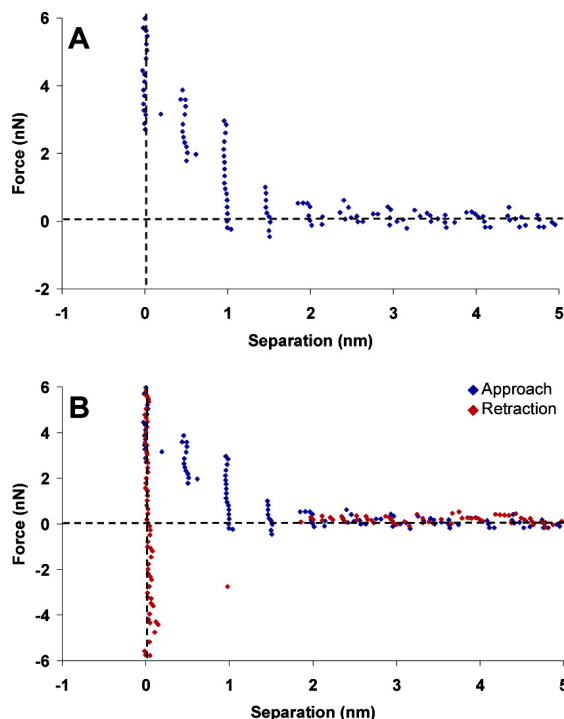


Figure 1.8 – Solvation force profile for an AFM tip on mica in the IL ethylammonium nitrate. **A** As the tip approaches the surface, one can observe at least 6 discrete jumps separated by approx. 5 Å, corresponding to rupturing through successive ion layers near the interface. **B** During the retraction of the AFM tip, a substantial adhesion force results in a zero force reached at a separation corresponding to four solvent layers. Reprinted with permission from Atkin *et al.* [24]. Copyright 2007 American Chemical Society.

This assumption contradicts the fact that typically ionic liquids do not have ions that are similar to this extent. This classic treatment has been shown to be in agreement in a limited way with a model by A. A. Kornyshev[23] based on modern statistical mechanics of dense Coulomb systems.

The ionic layers at the solid-IL interface have been observed by different means. One elegant way to probe it, is to use atomic force microscopy (AFM). In this case it is possible to use the tip of the AFM to poke through the layers of ions adsorbed near the surface. This directly measures the cohesion force of the different layers, and can be displayed in the form of a solvation force profile. (See fig.1.8) In all the systems studied by Atkin *et al.*[24], the force was never greater than 15 nN.

Further studies on the Au(111)-IL interface using the same technique have shown that it is even possible to directly measure the response of the layer structure to different gate voltages.[25] (See fig.1.9) “At the (slightly negative) open circuit potential, multiple ion layers are present, and the innermost layer, in contact with the Au(111) surface, is enriched in the cation due to electrostatic adsorption. Upon applying negative electrode

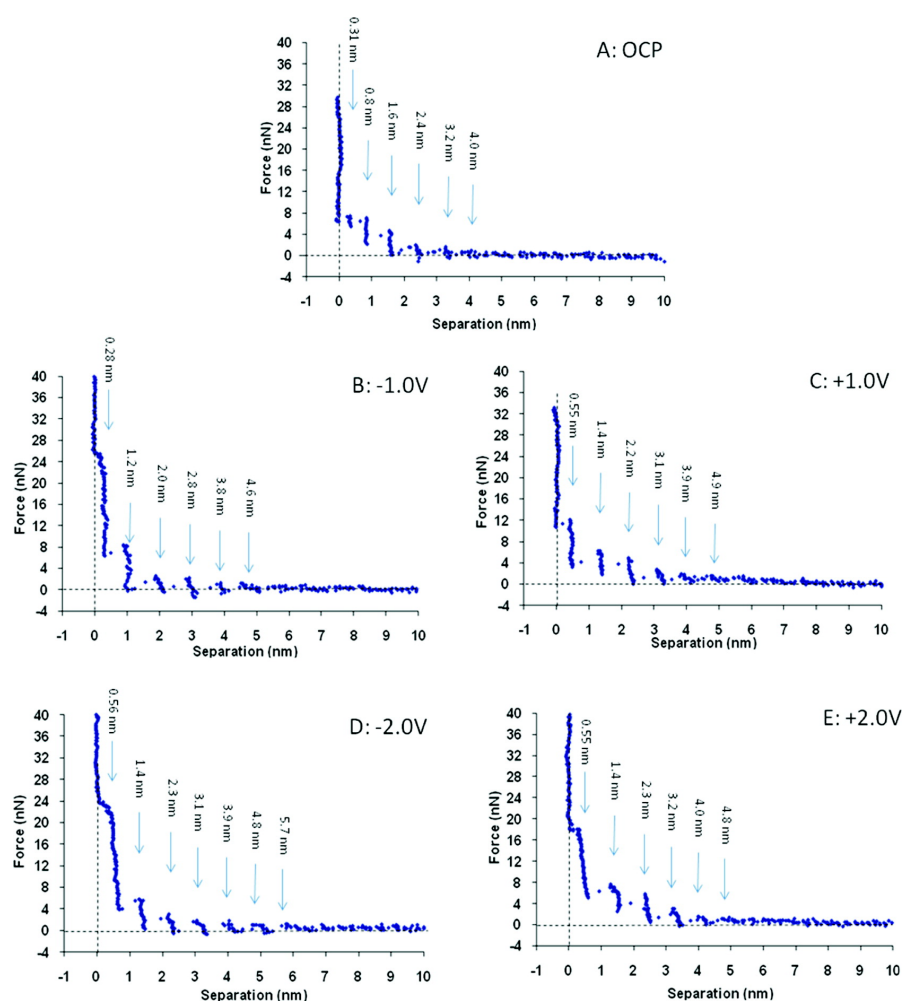


Figure 1.9 – Solvation force profile on Au(111) exposed to the IL 1-ethyl-3-methylimidazolium tris(pentafluoroethyl)trifluorophosphate. **A** At open circuit potential (-0.18V), multiple ion layers are visible. **B-D** For different voltage applied to the Au surface, in reference to a Pt electrode. Reprinted with permission from Hayes *et al.* [25]. Copyright 2011 American Chemical Society.

potentials (-1.0 V, -2.0 V), stronger IL near surface structure is detected: both the number of ion layers and the force required to rupture these layers increase. Positive electrode potentials (+1.0 V, +2.0 V) also enhance IL near surface structure, but not as much as negative potentials, because surface-adsorbed anions are less effective at templating structure in subsequent layers than cations”.[25] The distance between the steps of 0.83 nm corresponds to the ion pair diameter of the particular IL used in this case. It is remarkable to see that fig.1.9A shows two small steps 3 Å and 5 Å wide near the interface that likely corresponding to the sizes of the anion (5 Å) and the cation (3 Å). With an applied voltage, the magnitude of push-through force is higher than it is with OCP. And the number of observable layers increases with the applied potential. This indicates that the inner layers are more compact and more strongly bound. In this particular case of IL-Au(111) interface, the absence of a diffuse Gouy-Chapman layer shows that the Gouy-Chapman-Stern model is not adequate.[25] Instead this indicates a capacitive double layer with a decaying oscillating potential profile. This can be approximated to a series of plate capacitors with alternating decreasing polarity.

An alternative method to probe the ionic liquid at the solid-IL interface was demonstrated by Zhou *et al.*[26]. In this case they observed IL on uncharged graphene and charged mica surfaces using high resolution X-ray interface scattering. While in the case of uncharged graphene, they observed a densification of the first adsorbed IL layer, the “RTIL structure adjacent to the charged mica surface exhibits an alternating cation-anion layering extending 3.5 nm into the bulk fluid.”[26] It is interesting that with two different experimental methods, AFM as well as X-ray diffraction combined with modelization, and different systems, in both cases the observed depth of anion-cation layering reaches into the IL for a distance of the order of 3 – 4 nm.

1.3.3 Dielectric Gating Applied to Other Systems

In this work, we applied the dielectric gating technique to several Q2D materials. It is important to note that a similar technique was applied to superconducting materials among others by McDevitt, Haupt *et al.* already in the 90’s.[27–43] But since 2009, there has been an explosion of interest in the field following a couple publications by Iwasa, Kawasaki *et al.* [44, 45]. Up to 2014, the EDLG technique has been applied to a multitude of materials. In table 1.1 we show a non-exhaustive list of materials studied by using dielectric gating.

As we have seen in this introductory chapter, our main goal in this thesis is to introduce superconductivity in some novel Q2D materials by using EDLG concept. Indeed, as we shall see, this requires the development of several techniques, for suitable sample preparation, as well as advanced measurements discussed in the next chapter.

Table 1.1 – A few of the materials studied using dielectric gating, with non-exhaustive list of references.

Material	References
$\alpha - (\text{BDET} - \text{TTF})_2 \text{I}_3$ ^a	[46]
Au(111)	[25, 47]
$\text{Bi}_{2-x}\text{Mn}_x\text{Te}_{3-y}\text{Se}_y$	[48]
$(\text{Bi}_{1-x}\text{Sb}_x)_2\text{Te}_3$	[49]
Bi_2Se_3	[50–52]
Bi_2Te_3	[51, 53]
BiSbTeSe_2	[54]
Co	[55]
Diamond	[56, 57]
(Ga, Mn) As	[58]
$\text{GdBa}_2\text{Cu}_3\text{O}_{7-\delta}$	[29]
Graphene	[52, 59–61]
Graphene-tin nanohybrids	[62]
InO_x	[63]
KTaO_3	[64]
$\text{La}_{0.8}\text{Ca}_{0.2}\text{MnO}_3$	[65]
$\text{La}_2\text{CuO}_{4+\delta}$	[66]
$\text{La}_{0.75}\text{Sr}_{0.25}\text{MnO}_3$	[67]
MoS_2	[52, 68, 69]
$\text{Nb}_{76.1}\text{Al}_{17.7}\text{Ge}_{6.2}$	[27]
$\text{Nd}_{2-x}\text{Ce}_x\text{CuO}_{4-\delta}$	[27]
NdNiO_3	[70, 71]
$\text{Pb}_{0.3}\text{Bi}_{1.7}\text{Sr}_{1.6}\text{Ca}_{2.4}\text{Cu}_3\text{O}_{10}$	[29, 31]
$\text{Pr}_{1-x}\text{Sr}_x\text{MnO}_3$	[72]
Rubrene single-crystal ^b	[73]
Si	[74–76]
SmCoO_3	[77]
SnS_2	[78]
SrTiO_3	[45, 79]
$\text{SrTiO}_3(001)$	[80, 81]
$\text{TiO}_2(101, 001, 110 \text{ \& } 100)$	[81, 82]
$(\text{Ti, Co})\text{O}_2$	[83]
$\text{Tl}_2\text{Ba}_2\text{Ca}_2\text{Cu}_3\text{O}_{10}$	[27, 28, 33, 36]
$\text{Tl}_2\text{Ba}_2\text{CaCu}_2\text{O}_8$	[27, 28, 33]
$\text{Tl}_{1-x}\text{Pb}_x\text{Sr}_2\text{CaCu}_2\text{O}_{7-\delta}$	[27]
$(\text{Tl}_{0.5}\text{Pb}_{0.5})(\text{Sr}_{1.6}\text{Ca}_{0.4})\text{Ca}_2\text{Cu}_3\text{O}_9$	[42]
VO_2	[84–86]
$\text{YBa}_2\text{Cu}_3\text{O}_{7-\delta}$	[27, 29–32, 34, 35, 37–41, 43, 87–89]
ZrNCl	[52, 90–93]
ZnO	[44, 94, 95]

^a charge-ordered organic material

^b organic semiconductor used in organic light-emitting diodes

2 Experimental Section

2.1 On Molecular Beam Epitaxy of Cuprate Films

To synthesise cuprate films, we used an advanced oxide atomic-layer-by-layer molecular beam epitaxy system. (See figure 2.2) It is capable of reproducible fabrication of atomically smooth films of cuprates with control over the stoichiometry at the 1% level and digital control of layer thickness.[96–99] Since the electrostatic screening length for cuprates is of the order of one unit cell, it is imperative that the deposited films are continuous and defect-free on the same length scale. The crystal structure of films was monitored in situ during growth by reflection high energy electron diffraction (RHEED) (See figure 2.3) and after growth studied by X-ray diffraction. Both techniques as well as atomic force microscopy (See figure 2.1) showed the films to be of high quality and without secondary-phase precipitates.^a

^a This paragraph was adapted from [3].

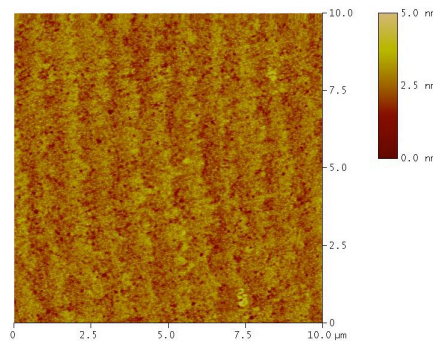


Figure 2.1 – A typical AFM image of the surface of a sample directly after MBE growth. Originally published in [1]: Supplementary Information.

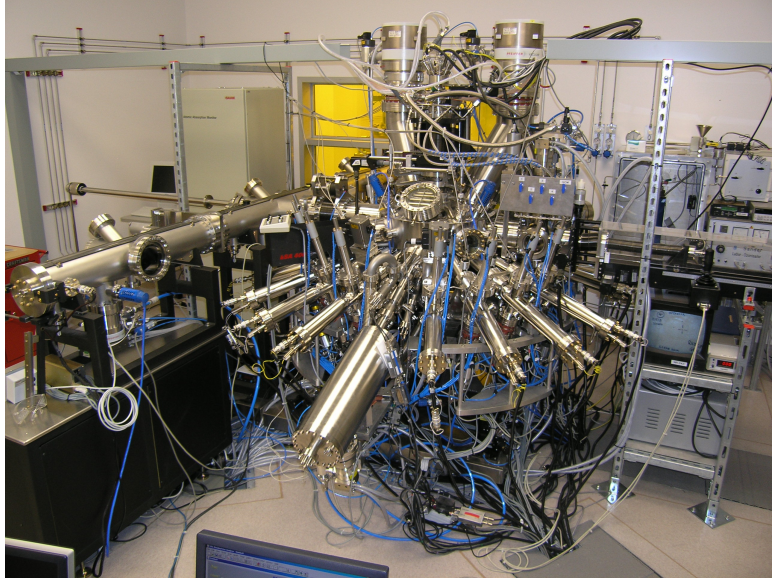


Figure 2.2 – Oxide Molecular Beam Epitaxy system used to grow the $\text{La}_{2-x}\text{Sr}_x\text{CuO}_4$ films studied in this thesis.

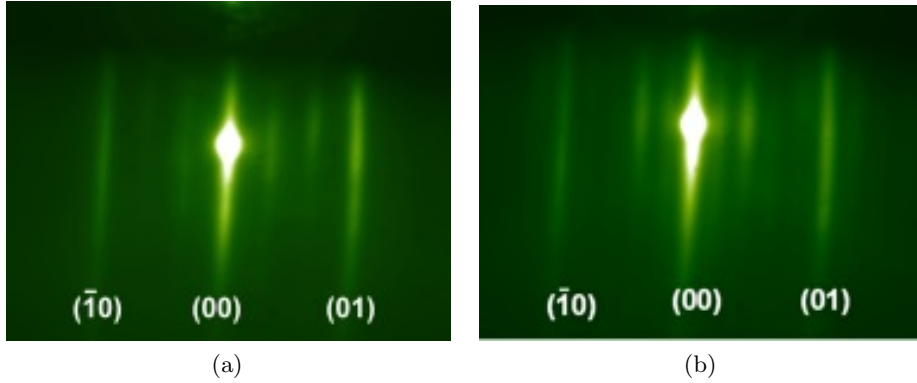


Figure 2.3 – RHEED image of a typical $\text{La}_{2-x}\text{Sr}_x\text{CuO}_4$ film. (a) after LaO layer. (b) after CuO_2 layer. Very strong specular reflection indicates that the surface is very flat even on the scale of the electron wavelength (0.1\AA). Long diffraction streaks indicate high surface crystallinity (with some terracing that originates from a slight miscut of the substrate). Absence of any transmission spots indicates absence of secondary-phase precipitates. Originally published in [1]: Supplementary Information.



Figure 2.4 – One of the two automated liquid helium dipsticks used for the transport measurement setups. Photo credit: Dr. Xi He.

2.2 Experimental Measurements

2.2.1 Transport Measurement Setup

Resistance was measured as the samples were cooled while keeping the applied V_g constant. To switch to a different gate voltage, V_g was set to 0V at the lowest temperature and then the sample was heated to T_{charge} where the new gate voltage was applied. For PEG-NaF we chose $T_{\text{charge}} = 302\text{K}$, whereas for DEME-TFSI $T_{\text{charge}} = 210\text{K}$. For DEME-TFSI, this corresponds to 20K above the lowest temperature for which a discernible change could be detected in the resistance of the device due to charging. The usual charging time was 30 minutes, which was sufficient for the ion motion in the electrolytes to decay and a new charging state to be established.^b

The Hall bars were current-biased with $1\text{--}10\mu\text{A}$ using a source-meter. A dual channel nanovoltmeter measured the longitudinal and transverse voltage. Delta-mode measurements were used to eliminate offsets. The gate voltage was applied and the gate current was measured by an electrometer source-measure unit. (See figure 2.12) The typical cooling rate was $\sim 3\text{K/min}$.^c

^b This paragraph was adapted from [1].

^c This paragraph was adapted from [1].

2.2.2 Magnetic Susceptibility Measurements

Magnetic susceptibility was measured by using a two-coil mutual inductance technique in a transmission geometry. Since the mutual inductance measurement does not require any photolithographic processing, contamination of the $\text{La}_{2-x}\text{Sr}_x\text{CuO}_4$ film by photoresist was avoided and formation of electric double layer via gate electrolyte was facilitated. Ti/Au contacts were deposited on $\text{La}_{2-x}\text{Sr}_x\text{CuO}_4$ samples through a shadow mask instead. Top gate geometry was utilised to apply gate voltages. A thin cover glass with evaporated gold was inserted between the $\text{La}_{2-x}\text{Sr}_x\text{CuO}_4$ film and the pickup coil. A drop of ionic liquid DEME-TFSI was applied on top of the $\text{La}_{2-x}\text{Sr}_x\text{CuO}_4$ film and the gate cover glass was placed on top of the film at a fixed height. The gate cover glass held the ionic liquid in place. The measurements were done in helium exchange gas to ensure a good temperature control. For each run, the $\text{La}_{2-x}\text{Sr}_x\text{CuO}_4$ film was charged at a chosen gate voltage for 30 minutes while maintaining the charging temperature, $T_{\text{charge}} = 210\text{K}$. Magnetic susceptibility was typically measured while the sample was cooled down slowly at a rate of 0.1K/min . An AC signal with amplitude of $5\mu\text{A}$ and frequency of 10kHz was applied to the driving coil and an induced voltage in the pickup coil was measured by a lock-in amplifier.^d

2.2.3 Automation of Transport Measurements

While the ionic liquid gating technique has the advantage over conventional gating techniques to allow for much larger induced carrier concentrations, up to $8 \cdot 10^{14} \text{cm}^{-2}$ reported in Yuan *et al.*[94], it is inherently a slow technique. Charging times are of the order of minutes and hours, not sub-millisecond as we experience it from electronic devices used in our daily lives. This is due to the need for ions to move in the liquid. This also means that a change in the gate voltage has no effect for temperatures under the melting point of the gate dielectric. In our case, where we mostly used DEME-TFSI as gate dielectric, the melting point, defined by the point where current started flowing through the gate to the source/drain, was at around 190 K. We are not aware of IL with significantly lower melting points. In a few cases we used PEG-NaF with a melting point at around 30°C . This means that one has to warm up the sample after each measurement in order to change the charge accumulated in the EDL. For this reason, the process is inherently slow. In order to effectively improve the throughput of our transport measurement, one of my first actions at the beginning of the work for this thesis was to automate as much as possible the work needed for our transport measurements. Starting from a pair of greatly similar existing dipsticks, used to manually lower the samples into a dewar of liquid helium, I automated them by mounting the sticks in fixtures that could be attached to the top flange of a transport dewar and that allowed linear movement of the sticks in to and out of the dewars by virtue of a threaded drive shaft coupled to a stepper motor. I integrated motor control electronics into our measurement setup in such

^d This paragraph was adapted from [1].

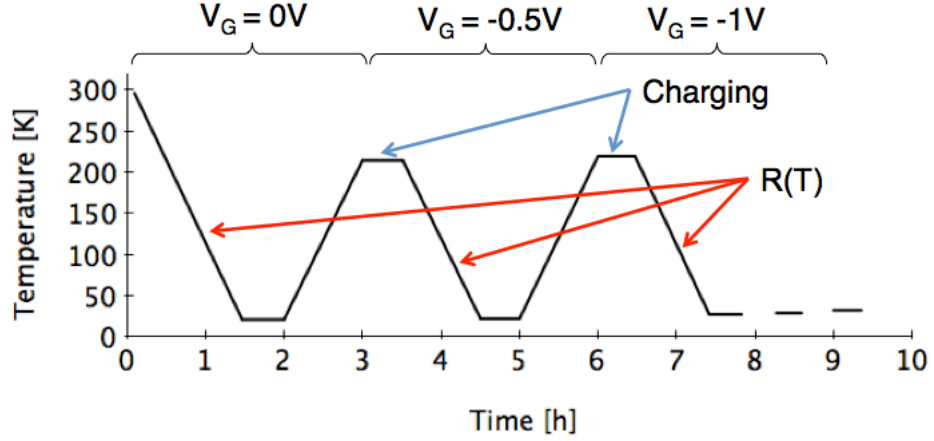


Figure 2.5 – Typical thermal cycling of sample for an EDLG experiment. After applying the IL, the sample is cooled from room temperature to 4 K at a constant cooling rate of $\sim 50 \text{ mK/s}$. During this cooling, the 4 point resistance, $R(T)$, is continuously measured. Once it reaches the base temperature, other measurements, such as $V(I)$ can be made. Then the sample is warmed up to T_{charge} . During this warm up, no measurements are taken, as the warming rate is less well controlled than the cooling rate in our setup. Once it reaches T_{charge} the temperature is stabilised for the duration of charging and a new gate voltage V_g is applied.

a way that allowed complete computer control of the stick motion while also eliminating electrical noise generated by the motor power supply. This allowed me to measure up to 14 thermal and charging cycles per day for each dipstick. Figure 2.5 shows such a typical thermal cycle sequence. The reliability is such that the measurement can be remotely controlled and that the operators presence is only required to refill the helium dewar and to change the sample.

In this quest to speed up the measurement cycles, we also made the deliberate choice to measure samples only during half of the thermal cycle, during the cool down. During the measurements we tried to keep a constant temperature ramping rate of around 50 mK/s . I soon realised that, with the existing dipstick system, the cooling rate during the lowering of the dipstick in the dewar was much easier to keep steady than the warming rate while pulling the dipstick out of the dewar. At the same time this limited excessive boiling off of liquid helium. Dipsticks as the ones we used, that rely on the physical position of a sample within the helium dewar to determine the sample temperature, are somewhat less controlled than other cryostats. In particular, the temperature ramping rate during cool down can experience sudden jumps after movements of the probe. The position and amplitude of these jumps is not very reproducible, as it depends on the current situation of the dewar, such as liquid helium level, pressure, etc. Often we observed a higher cooling rate in the range $130 - 150 \text{ K}$, reaching up to 200 mK/s over a short period of time. This was not considered problematic, as it was well above the transition temperature

T_c of $\text{La}_{2-x}\text{Sr}_x\text{CuO}_4$. Below 100K, the ramping rate was usually less than 60mK/s. At low temperatures ($<20\text{K}$) this rate steadily fell down to just 1mK/s. This was not considered an issue as slow cooling rates are preferred, as they reduce the temperature uncertainty due to the thermal lag between the sample and the thermometer. It is important to note that once the sample reached a temperature of around 7K often the sample experienced a short warm up period, despite being lowered into the liquid helium bath. Our working hypothesis is that at this point the aluminum can surrounding the sample space touches the surface of the liquid helium, and the resulting rapid evaporation leads to an increase of pressure, and thus of the temperature, in the sample space. These minor inconveniences resulting by the use of dipsticks were not deemed critical, as there was no observed effect on the various measurements taken. To reduce the effect of the single lowering steps changing the pressure and thus temperature in the dewar, it was fitted with a very low overpressure valve, basically staying at atmospheric pressure, but avoiding the build up of ice in the dewar that would be dangerous. The main advantage of direct dipping into helium is the large heat capacity of helium gas, and thus a relatively rapid cooling of the sample. Combined with the automation, this allowed us to reach a frequency of around 12 to 14 measurements and charging cycles per 24 hours. Without need of refilling a dewar, this means that a sample undergoes around 30 distinct charging cycles, without our intervention. As two similar systems were in place, this yielded a significant number of measurements, and allowed to weed through numerous sample architectures in order to find those right combination of films, contact and liquid, that reacted to the gating technique. We decided not to try to increase further more the measurement rate by increasing the nominal cooling rate to 100mK/s or more as this would have greatly reduced the density of measurement points per degree Kelvin.

Towards the end of the work on this thesis, in order to reduce our helium consumption, and to get much better temperature stability, we acquired a closed cycle cryocooler. While none of the data shown here were measured on this system, it will allow much more detailed studies, as with a few improvements we reached a temperature stability of $<1\text{mK}$ over the whole range from $<4\text{K}$ to room temperature. All this while the time for a whole temperature and charging cycle is just slightly increased from 2 h to approx. 3 h. This new capability should allow for much more detailed studies of the EDLG technique in our laboratory in a near future. (See Appendix A for details)

2.2.4 EDLG Sample Preparation

After MBE growth, the samples were patterned using standard photolithography, ion milling, and e-beam evaporation techniques. The films were patterned into sets of rectangular bars of various aspect ratios. This part of the work was done by Dr. Anthony Bollinger. The widths of the rectangular devices were 10 – 500 μm and the lengths were 500 – 900 μm , with multiple voltage contacts regularly distributed on both sides of the strip, 50 to 300 μm apart. Different device patterns (See figures 2.6, 2.7 and 2.8) were

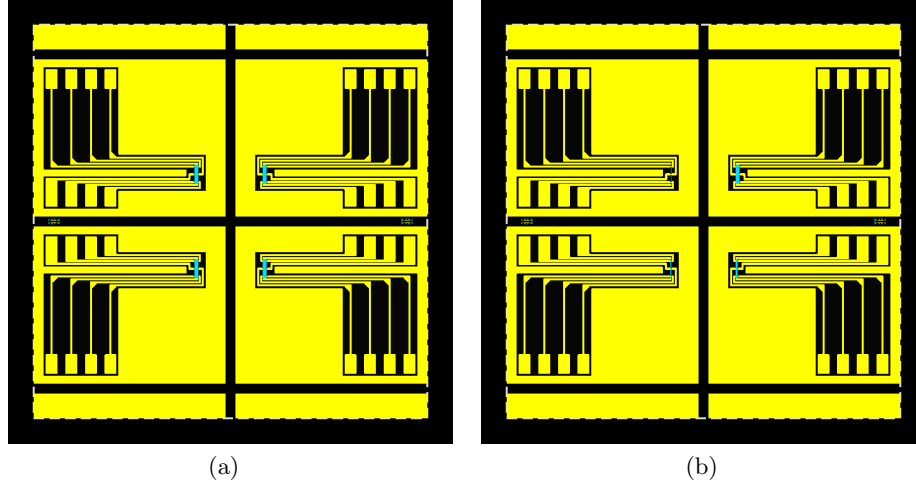


Figure 2.6 – View of several of the patterns used in our photolithographic process to prepare the samples for the transport measurements. These patterns were optimized for a small sample of $3\mu\text{m} \times 4\mu\text{m}$ that can be easily accommodated in a dilution fridge. In yellow the gold contacts are shown, black indicates where the sample film has been removed by etching down to the substrate, and in blue the film that is left. The dashed line indicates the contour of the 10mm by 10mm substrate most frequently used.

designed and used. Some of the wire bonds used to connect the device to the sample holder are clearly visible. The simplest devices were fabricated using our standard lithography masks and just adding a platinum foil top gate (See figure 2.10a and 2.10b) about 0.1 to 0.3 mm above the sample surface. The ionic liquid was kept in place between the gate and the sample by the capillary forces. In Figure 2.10a, the visible discolouration around the gate shows the part of the sample wetted by the ionic liquid. For highly resistive samples, a different mask was used with inverted aspect ratios, the width of 1 cm, and the length between $3\mu\text{m}$ and 1 mm. (See figure 2.10b) Parallel gold electrodes, separated by gaps of increasing width, were deposited subsequently. Optionally, the electrodes can be covered by a layer of insulator (Al_2O_3), except for the part not covered by ionic liquid, where the wire bonds are attached. This ensures that during charging, the electric double layer is mainly formed on top of the free surface of the sample, and not confined just to the gold contacts with a much larger surface. As for the previous pattern, a platinum top gate is added, and the ionic liquid, not visible here, is kept in place by the capillary forces. The patterns in Figures 2.10c and 2.10d, which include coplanar gates (the largest visible gold patterns), were designed specifically for gating with ionic liquid. Here, the ionic liquid is kept in place by the capillary force between the substrate surface and a microscope glass cover slide inserted just above the sample. The meniscus at the edge of the cover slide in Figure 2.10c is clearly visible.^e

^e This paragraph was adapted from [3].

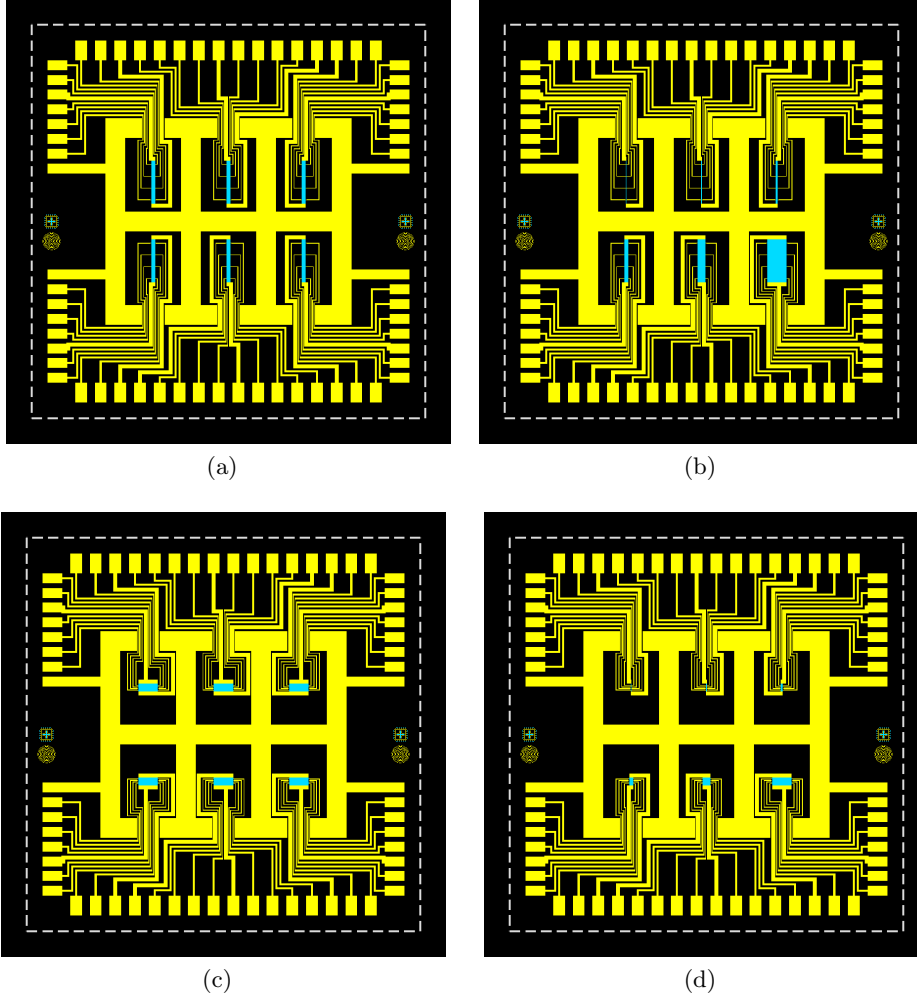


Figure 2.7 – View of several of the patterns used in our photolithographic process to prepare the samples for the transport measurements. These were the type of patterns most frequently used in this study. They allow to design 6 different devices comprising each two large current contacts and 4 voltage contacts on each side. This allows for the measurement in a simple 4 point configuration or in a Hall bar configuration. The width of the bars can be between $10\mu\text{m}$ and $500\mu\text{m}$, while the distance between voltage contacts is either $300\mu\text{m}$ or $100\mu\text{m}$. In yellow the gold contacts are shown, black indicates where the sample film has been removed by etching down to the substrate, and blue is representative of the film that is left. The dashed line indicates the contour of the 10mm by 10mm substrate most frequently used.

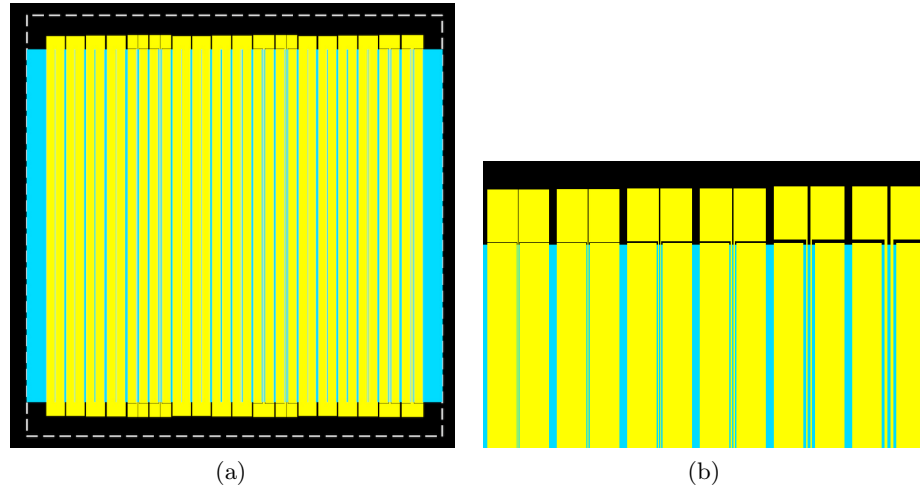


Figure 2.8 – Lithographic patterns used for high resistivity samples. In yellow the gold contacts are shown, black indicates where the sample film has been removed by etching down to the substrate, and blue is representative of the film that is left. (b) shows a zoomed view of a detail of the mask. All these 4 point devices are 10mm wide, while the length varies from 3 μm to 20 μm . Several other patterns with wider contacts were also used. The dashed line indicates the contour of the 10mm by 10mm substrate most frequently used.

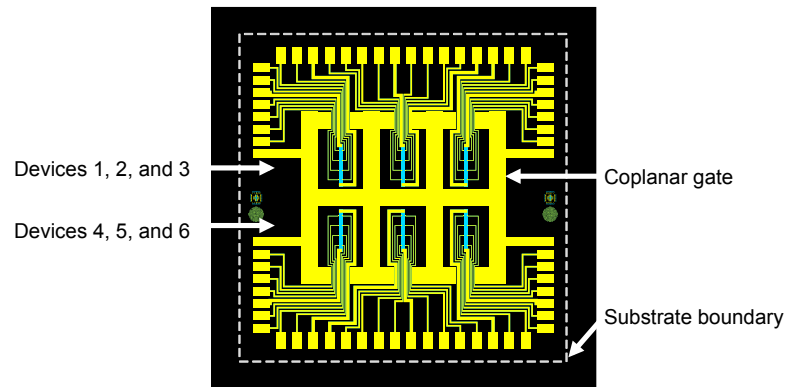


Figure 2.9 – The default numbering convention is from top to bottom, left to right. Thus devices 2 and 5 are the closest to the centre of the film, and should be in the most uniform part of the film. For most measurements, each device was subdivided into two devices, as our nano-voltmeter allowed for two measurement channels. The default convention is for channel 1 (Ch1) to measure the voltage between the pair of voltage contacts nearest to the centre of the film, while channel 2 (Ch2) connects to the voltage contacts near the edge of the film.

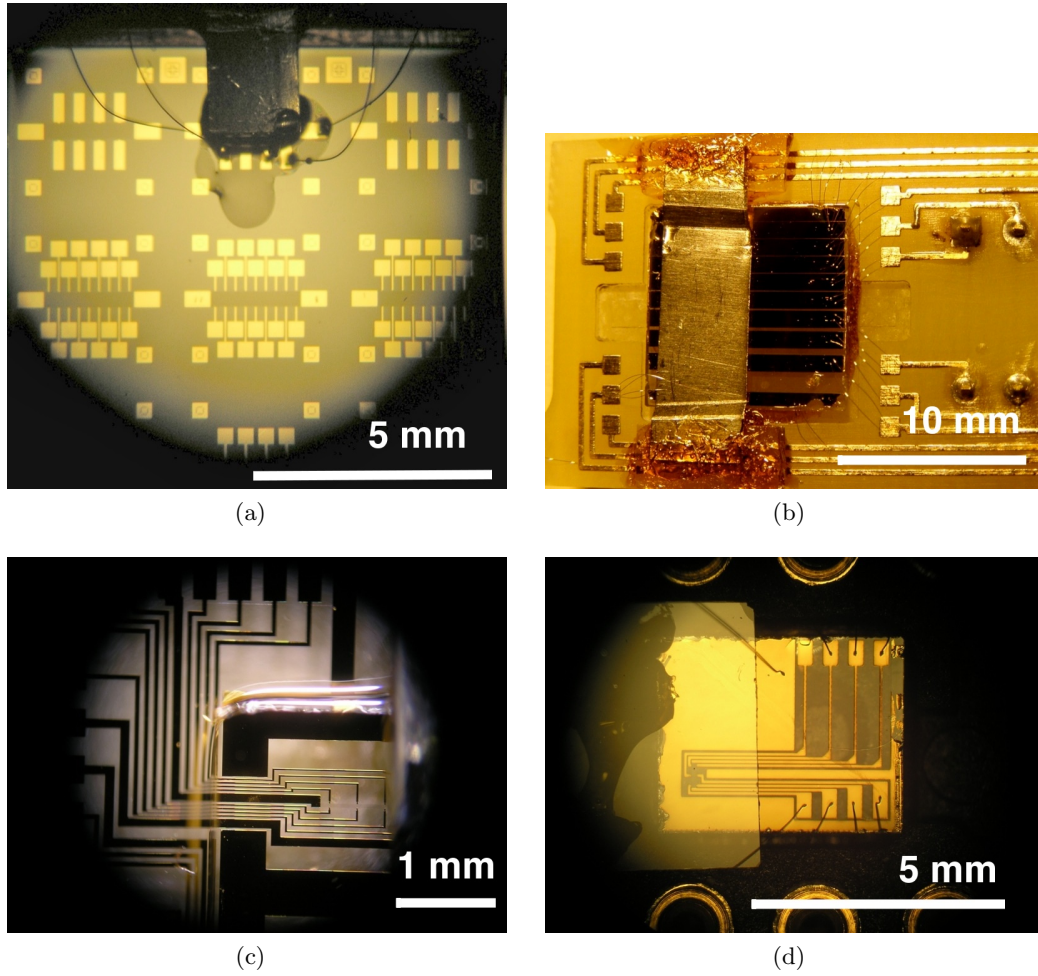


Figure 2.10 – Optical micrographs of various fabricated thin film devices used in this study; in all these samples, the ionic liquid used is DEME-TFSI. The resistance is measured using a 4-point configuration. (a) A simple 6-point contact strip pattern adapted to field effect studies. (b) A pattern used for highly resistive samples. (c) A pattern specifically designed in order to gate thin film samples with ionic liquid, with the devices surrounded by a larger coplanar gate. Only one out of six devices is visible in this picture. (d) Another pattern with four separate devices placed near the centre of a $10 \times 10 \text{ mm}^2$ film, designed to allow the sample to be diced. One of these four devices is mounted and wire-bonded; the gate is visible as the gold square at the top left of the sample. The glass cover slide is already in place, but the ionic liquid has not yet been deposited. Originally published in [3].

2.2.5 The Contact Challenge

When studying complex materials the key issue is how to create a good contact to the material under investigation. Earlier work had showed that for the $\text{La}_{2-x}\text{Sr}_x\text{CuO}_4$ and similar materials grown in the oxide MBE group at BNL, the best contact resistances were obtained when a thin layer of gold is evaporated on the sample by MBE just after it has been cooled to room temperature in the growth chamber. This in-situ layer creates a good contact to the cuprate and protects it from most surface contaminations that are the result of photolithographic processing. Using standard photolithographic patterning techniques, in a first step, devices are patterned from the film, and in a second step more gold (100-200 nm) is evaporated using e-beam evaporation to make foot contacts to the device and to define traces that will lead from the device to remote bonding pads. Up to this point the original in-situ gold layer is still in place on top of the device that is in preparation. The last step is to remove this in-situ gold layer by a short bath in gold etchant. This will leave a device that is perfectly clean, while only affecting the optical quality of the contacts with a little haze.[100]

This way of patterning contacts works well for $\text{La}_{2-x}\text{Sr}_x\text{CuO}_4$ samples for most transport measurements, but in our case we stumbled on an issue when we started gating our devices using ionic liquid. We realised that over a certain gate voltage, or after several cycles, sometimes more than 50, the IL would lift off the contacts to our device. (See figure 2.11) This would either result in lost contacts, or in shorts between contacts due to gold flakes floating in the IL. Once this had happened, no further measurement was possible. This situation is referred to as the death of the device. Usually, it is not actually the device itself that gets irreversibly damaged, but the contacts to the device that are broken due to a liftoff of the gold traces by the IL. Stripping of the gold contacts and patterning of new contacts has helped sometimes, but has proven not to be a reliable solution to the problem. Similar effects have been described in the literature, where it has been shown that IL can be used to functionalize and exfoliate graphene nano-sheets from graphite.[101]

Now, this was a really challenging problem that slowed us down for nearly 2.5 years. In fact, as contacts would break in a quasi random pattern, it was difficult to predict how long a device would be usable. Some survived over hundreds of cycles, while others did not live for more than a day. The random nature of these failures is not a problem when working with dipsticks and other more basic types of measurement setups, where one just needs to switch to the next device on the same film. But it makes it difficult to plan measurements requiring access to more complex instruments such as electromagnets or ^3He based cryogenic systems needed to reach sub-Kelvin temperature ranges. In these kinds of systems where the setup time is significant, it is crucial to have a reasonable prediction of survival of the device before attempting the experiment. It is only during the last few weeks of the experimental work leading to this thesis that the final breakthrough came. As in the group, thin film growth of strontium ruthenate, Sr_2RuO_4 ,

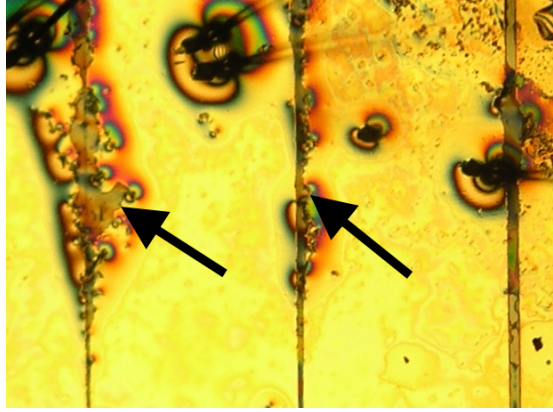


Figure 2.11 – This picture shows a typical case of damage to contacts after several EDLG cycles. In the example shown here, we used a high resistance mask on sample #1177. The contacts are simple gold bars $300\mu\text{m}$ wide and 1cm long separated by increasing gaps of 3, 5 and $10\mu\text{m}$. It can be clearly seen how under the applied gate voltage, the IL started to undercut and liftoff parts of the contacts. On narrower gold traces this can lead to either broken contacts or shorts due to floating gold flakes in the IL.

by sputtering had been studied for a significant time, we had access to a good conducting oxide. From our experience with its use as backside coating, we knew that these films adhere very well to our LaSrAlO_4 substrates. We wanted to keep the photolithographic capability, thus the attempt was made to grow amorphous Sr_2RuO_4 on a patterned sample. The results were exactly as we had hoped. Amorphous Sr_2RuO_4 contacts do not only show a very reasonable contact resistance, they also resist well to the EDLG technique, and the failure point is extremely reproducible. Finally, this will allow to open the next chapter of the EDLG technique applied to $\text{La}_{2-x}\text{Sr}_x\text{CuO}_4$. Now that reliable predictions can be made of the point where a sample will fail, it will be possible to undertake more demanding experiments with a reasonable expectation of success in the form of possible measurements, and not ending up with an unusable sample after days of preparation.

2.2.6 Dielectric Gating Procedure

In figure 2.13, the typical charging behaviour of a device is illustrated. During a set charging time, the device is kept at a stable temperature, 270K for 60 minutes in this case. Afterwards the sample is cooled at a steady rate of around 50mK/s by slowly lowering it into a helium dewar. At the beginning of the charging cycle, the gate current I_G is relatively important, but it decreases exponentially. Once the cooling starts, the gate dielectric (PEG-NaF in this case) freezes. More than an actual solidification, we observe the disappearance of all ionic conductivity in the gate dielectric. This dramatically reduces the measured gate current. Below the freezing point one can consider that the measured gate currents ($\sim 0.5\text{pA}$) are due to instrumental noise and to the movement of the dipstick. Qualitatively, this is a general behaviour for all dielectrics we used. It

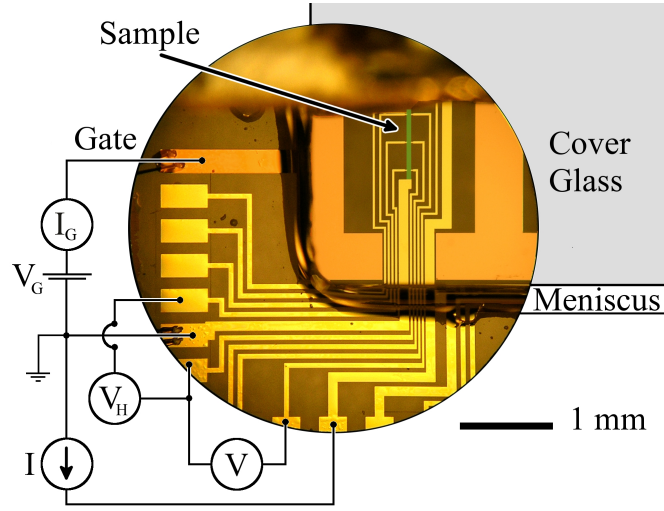


Figure 2.12 – Optical micrograph of a fabricated device. The measurement circuit is indicated. The electrolyte was held in place with a glass cover slip. The gate electrode and the Hall bar are in false colours for better contrast. Originally published in [4].

varies only slightly with the amplitude of gate voltage, the charging temperature, and the melting point of the dielectric used. I did not spend much effort in optimising the gate dielectrics used. There are millions of possible IL available. Investigating them was not the aim of this thesis. We focused on a few that we knew from the literature, or that were suggested through discussions with chemists. Table 2.1 indicates the dielectrics used during this work.

We determined the minimal charging temperature by cooling down a sample to 170K, well below the melting temperature of DEME-TFSI, used as illustration. At this point, changing V_G has no effect on the measured resistance of the sample. I then guided the sample through a series of temperature cycles while slightly increasing T_{charge} at each step. This allows to observe when an effective gating effect takes place, and there is an effect on the sample. In the case of DEME-TFSI, the gating effect sets in at a temperature between 185K and 190K. This lead to initial experiments with $T_{\text{charge}} = 192\text{K}$. (See figure 2.14) I later increased the temperature stepwise, as higher temperatures imply faster charging times, and a comfortable charging temperature range was 210 – 220K. When $T_{\text{charge}} > 230\text{K}$, empirically the devices would break faster. These temperatures depend on the purity of the gate dielectric. Both DEME-TFSI and PEG-NaF have a tendency to absorb water from the environment, as we did not prepare the sample in a controlled atmosphere. This impurity changes the optimal T_{charge} .

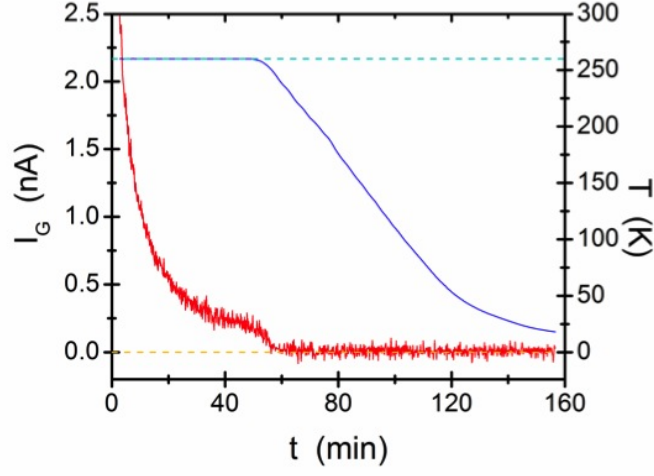


Figure 2.13 – Typical charging behaviour of a device. In red, the gate current (left scale), and in blue the temperature (right scale). The sample is charged at T_{charge} , in this case for 60 minutes, and then cooled to 4K. The gate current decreases exponentially, and then vanishes once the sample is cooled below the freezing temperature of the dielectric used.

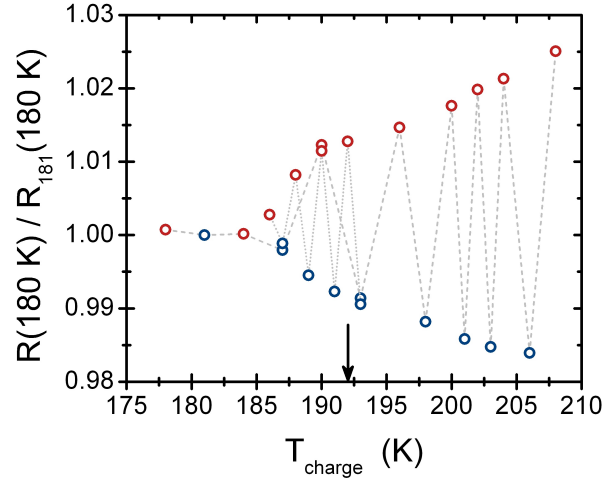
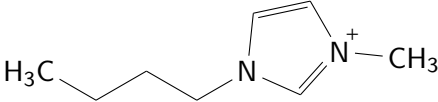
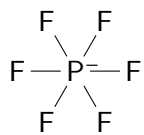
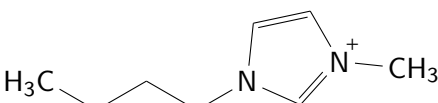
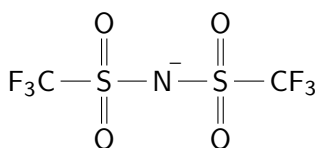
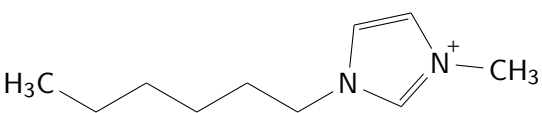
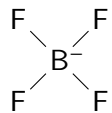
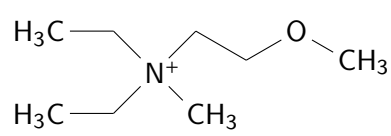
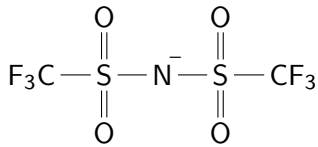
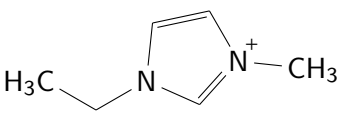
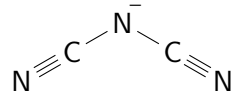
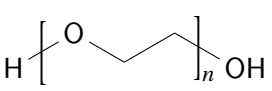



Figure 2.14 – Effect of charging at various charging temperatures, T_{charge} , with DEME-TFSI used as the gate electrolyte. Originally published in [3].

2.2. Experimental Measurements

Table 2.1 – List of gate dielectrics used.

Abbreviation	Name
BMIM-PF ₆	1-butyl-3-methyl-imidazolium hexafluorophosphate
	 
BMIM-Tf ₂ N ^a	1-butyl-3-methyl-imidazolium bis(trifluoromethanesulfonyl)imide
	 
C6MIm-BF ₄	1-N-hexyl-3-methylimidazolium tetrafluoroborate
	 
DEME-TFSI ^a	N,N-diethyl-N-methyl-N-(2-methoxyethyl)ammonium bis(trifluoromethylsulphonyl)imide
	 
EMIM-DCA	1-ethyl-3-methylimidazolium dicyanamide
	 
PEG-NaF	Sodium Fluoride salt dissolved in Polyethylene Glycol
	 

^a Tf₂N and TFSI are synonyms

2.2.7 Summary on Dielectric Gating

EDL gating using ionic liquids is a powerful technique. From our studies with tens of samples, I will resume a few points we have learned, as a starting point for the scientist interested in applying this technique to new systems.

1. Ionic liquids are relatively strong polar solvents. This can be an issue when they enter in contact with some materials such as glues. If bonding is needed, TorrSeal® vacuum equipment high vacuum epoxy from Varian has good chemical inertia. We had good experience with it, even if it is lightly etching copper during the curing time.
2. When the gate voltage is applied, the ionic liquid has the capacity to delaminate most contacts. (See figure 2.11) It can also intercalate itself in some layered materials. It is thus crucial that the contact material is well matched to the sample, and that the voltage limits for a particular combination of ionic liquid, sample and contact material are studied and then respected. In our case, the most frequent case for the sample *death* was a sudden loss of contacts, only rarely was damage to the sample itself visible in post-mortem microscopic observation. Ionic liquids can even be used to exfoliate graphite for forming graphene sheets.[101] In different cases, we tried to protect evaporated gold contacts from the ionic liquid by a lithographically defined isolating layer such as aluminum oxide, but in most cases this was delaminated even before the gold contact. Also often the delaminating started from the corner of contact traces, hinting at some form of edge effect.
3. While there are millions of possible ionic liquids, they are rarely well characterized. Often even the melting point is unknown. It is outside of the scope of this thesis to study a significant number of them. For this reason we focused on a few, such as DEME-TFSI, that were used successfully by several other groups, and had a low melting point of less than 200 K (defined as the temperature where no effective charging was observed).
4. Since the field effect happens on the topmost layer of the sample, it is highly important that the first layer is as clean and as perfect as possible. Any surface contamination will significantly reduce the size of the observed effect.
5. A device can be trained by cycling the gate voltage. After a few of these *cleaning cycles* the amplitude of the effect on the device increases. While I did not studied the reason for this improvement, it could be related to the removal of surface contamination and/or an improvement of the crystallinity of a Helmholtz layer adsorbed to the surface of the sample. This has also been observed by other groups.^f Some explanations for this mechanism can be found in [43].

^f H. T. Yuan, personal communication

6. Most room temperature ionic liquids are compatible with Ultra High Vacuum[102], except a few that decompose into water when exposed to low pressure. Also as polar solvents, they can be strongly hydrophilic. Thus water contamination can be an issue. It can be observed by an increase in the freezing temperature. Overnight baking at low temperature (20 to 80 °C) under vacuum can remove this water contamination from the ionic liquid before it is applied to the sample.
7. For transport measurements, in most cases, one is interested in effects at the interface. It is thus beneficial to start from a relatively insulating sample. In this way, the contribution from the bulk can be neglected. But the sample should not be too insulating, as in this case the time constant for an effective charging of the EDLC increases to the point of becoming impractical. We had good experience with sample geometries resulting in overall resistances of the order of 10 k Ω to 100 k Ω .
8. Most samples show a strong hysteresis, thus the charging history plays an important role in the overall behaviour of the sample. For this reason the gate voltage or even the integrated gate current are relatively weak proxies for the actual induced charge in the sample, and it is better to find an alternative way of estimating the carrier concentration, such as Hall effect.
9. Charging happens only above the melting temperature. This is quite badly defined as the solidification resembles more a glass transition than a crystallisation. Charging time, charging temperature and applied voltage during warm up each play a role with somewhat limited importance. The combination of these parameters has an impact on the voltage at which the sample dies. Consequently it is important to have some level of consistence when changing them and avoid sudden changes. For DEME-TFSI on $\text{La}_{2-x}\text{Sr}_x\text{CuO}_4$ we had good success by applying voltages of $-3\text{V} \leq V_g \leq 3\text{V}$ at charging temperatures in the range $192\text{K} \leq T_{\text{charge}} \leq 230\text{K}$.

3 Field Effect Results

3.1 Field Effect on Underdoped $\text{La}_{2-x}\text{Sr}_x\text{CuO}_4$

It took us quite a long time to find out the optimal sample architecture to study underdoped films. Finally for underdoped $\text{La}_{2-x}\text{Sr}_x\text{CuO}_4$, the films presented here were deposited on single-crystal LaSrAlO_4 substrates cut perpendicular to the (001) direction. The layering structure for most films consisted of (i) 1 unit cell (UC) thick $\text{La}_{2-0.44}\text{Sr}_{0.44}\text{CuO}_4$ buffer layer, (ii) 5 unit cells of insulating La_2CuO_4 , and (iii) 1, 1.5, or 2 UC thick layers of $\text{La}_{2-x}\text{Sr}_x\text{CuO}_4$ with $x = 0.10$ to 0.20 . (See figure 3.1) The first layer (i) is a buffer that facilitates excellent growth of the subsequent La_2CuO_4 and $\text{La}_{2-x}\text{Sr}_x\text{CuO}_4$ layers. While its stoichiometry suggests that it should be metallic, it is in fact insulating as verified by subsequent transport measurements. The reasons for this are not completely understood but may be in part due to the “polarization catastrophe”, i.e., the mismatch in sequences of charges of atomic monolayers in LaSrAlO_4 (+0.5, -1, +0.5) and in $\text{La}_{2-x}\text{Sr}_x\text{CuO}_4$ (+1, -2, +1). High-resolution transmission electron microscopy (TEM) studies have indeed shown that these first 5-6 atomic layers next to the substrate are heavily modified in structure and in stoichiometry. In any case, this buffer is not expected to play a significant role in the transport properties of our devices.^a

A large number of $R(T, V_g)$ curves were recorded, scanning V_g in small steps. In some initially underdoped samples, the data span the superconductor–insulator transition in a broad range, with many curves on both sides; an example is shown in figure 3.2. Such data enable a meaningful scaling analysis that can teach us about the nature of the quantum phase transition (QPT) and the quantum critical behaviour in underdoped films. The theory of continuous phase transitions states that in the critical region physical observables obey scaling laws such that their correlation functions depend on space and time coordinates only in combinations r/ξ_0 and t/τ , where the scales of ξ_0 (correlation length) and τ (correlation time) are determined by microscopic parameters

^a This chapter was adapted from [1].

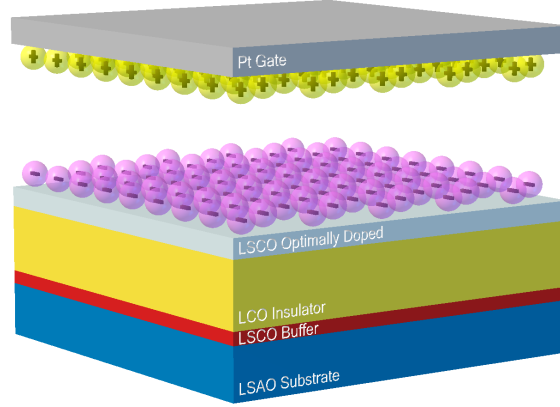


Figure 3.1 – Schematics of a typical $\text{La}_{2-x}\text{Sr}_x\text{CuO}_4$ - La_2CuO_4 heterostructure used to fabricate EDLT devices. For clarity, the polymer electrolyte (or the ionic liquid) is not shown; we just show the anions adsorbed to the film surface and the cations attracted to the negatively charged Pt gate electrode. Originally published in [1], Supplementary Informations.

of the Hamiltonian and diverge at the transition as:

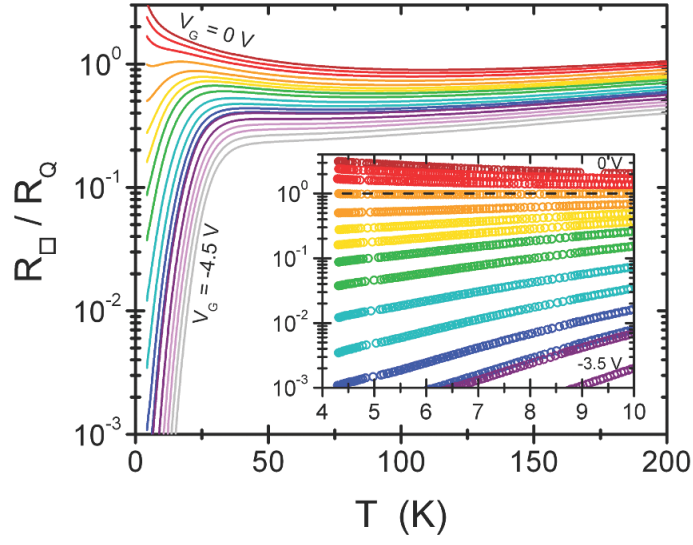
$$\xi_0 \propto |x - x_c|^{-\nu} \quad (3.1)$$

and

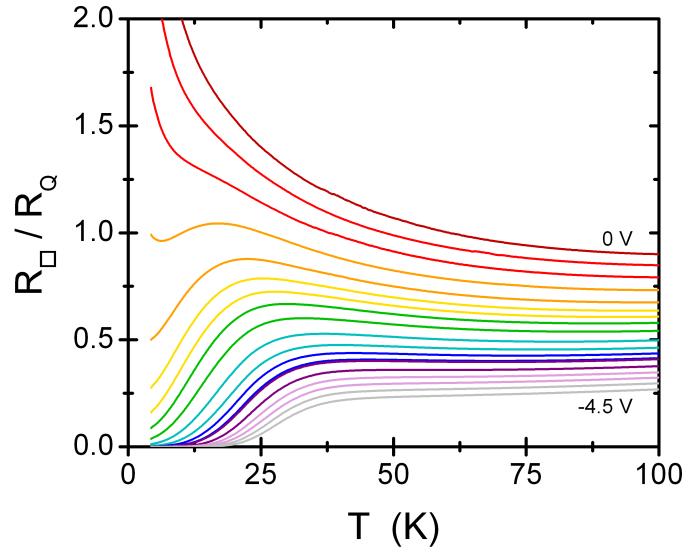
$$\tau \propto \xi_0^z \propto |x - x_c|^{-z\nu} \quad (3.2)$$

The actual scaling functions, together with the exponents ν and z , depend only on the large-scale physics, the universality class being determined by such general properties as the space dimensionality, presence of disorder, and the symmetry of the order parameter manifold. Competition between energy and entropy can drive a classical phase transition at finite temperature $T = T_c$. QPTs, on the other hand, occur at $T = 0$, triggered by a change of some external parameter (pressure, chemical composition, etc.). A quantum critical point separates ground states with different symmetry. The scaling of resistivity near the superconductor-to-insulator transition in (quasi-) two-dimensional systems is of particular interest because two-dimensionality is special (it is the lower critical dimension) for both superconductivity and localisation, and because in two dimensions, the length scale drops out for resistance so that its value at the critical point should be universal. For two-dimensional QPT, the appropriate finite-size scaling is $R_\square(x, T) = R_c F(|x - x_c| T^{-1/z\nu})$, where R_\square is the resistance per square, R_c is the limiting ($x \rightarrow x_c$ and $T \rightarrow 0$) resistance, and $F(u)$ is some universal function of u (≥ 0) such that $F(u) \rightarrow 1$ when $u \rightarrow 0$. The value of R_c , which can be obtained by scaling from data taken at finite T , together with ν and z encode the essential physics of the transition.

In figure 3.3, we replot the same R_{\square} data as a function of a measured quantity, $x = 0.33 \text{ k}\Omega / R_{\square} (T = 180 \text{ K})$, approximately equal to the number of mobile holes per one formula unit. (The precise value of carrier density affects none of our conclusions.) We note that this is the same $R(T, x)$ data matrix as in figure 3.2, but we have inverted it here, that is, we plot $R_{\square}(x)$ for various values of T . All curves are seen to cross at a single point x_c , which corresponds to the separatrix, that is, the $R(T)$ curve that is essentially constant in the temperature interval under study, and which separates insulating from superconducting behaviour. This can be seen directly in the inset of figure 3.2. From figure 3.3, we can read the critical values of x and R_{\square} to be $x_c \simeq 0.06$ and $R_c \simeq 6.45 \pm 0.1 \text{ k}\Omega$. In figure 3.4, we have scaled the abscissa as $u = |x - x_c| T^{-1/z\nu}$. As the result of this scaling, hundreds of curves have collapsed to one, showing at $T = 0$ a bifurcation, or unstable fixed point. The collapse is excellent up to about 10 K for $z\nu = 1.5 \pm 0.1$, and the exponent is identical on both sides of the superconductor-to-insulator transition. This is consistent with a continuous two-dimensional superconductor–insulator QPT, with an extensive region of quantum critical behaviour. The good agreement with a two-dimensional theory suggests that the active part of the film is extremely thin, in contrast to what one would expect in the case of massive interdiffusion or intercalation, for which the active part of the film is certainly deeper and probably fractal-like.



(a)



(b)

Figure 3.2 – Temperature dependence of normalised resistance $r_x(T) = R_\square(x, T)/R_Q$ of a film that was initially heavily underdoped and insulating, on a logarithmic scale. (b) shows the same data on a linear scale. Originally published in [1].

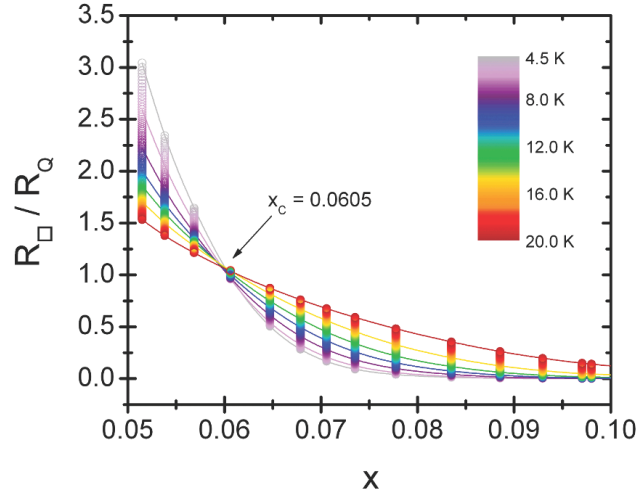


Figure 3.3 – The inverse representation of the data from figure 3.2, that is, the $r_T(x)$ dependence at fixed temperatures below 20 K. Each vertical array of (about 100) data points corresponds to one fixed carrier density, that is, to one $r_x(T)$ curve in figure 3.2. The colours refer to the temperature, and the continuous lines are interpolated for selected temperatures (4.5, 6.0, 8.0, 10.0, 12.0, 15.0 and 20.0 K). The crossing point defines the critical carrier concentration $x_c = 0.06 \pm 0.01$, and the critical resistance $R_c = 6.45 \pm 0.10 \text{ k}\Omega$. Originally published in [1].

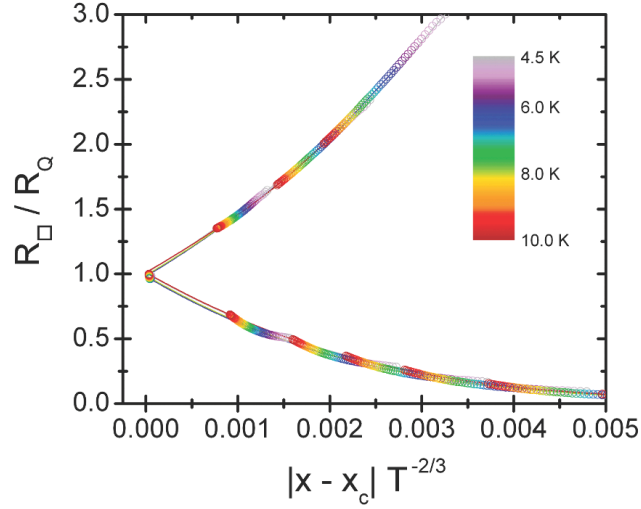


Figure 3.4 – Collapse around the critical point showing the collapse of all the measured curves of this sample on a single double valued function depending only on the distance to the critical point. Originally published in [1].

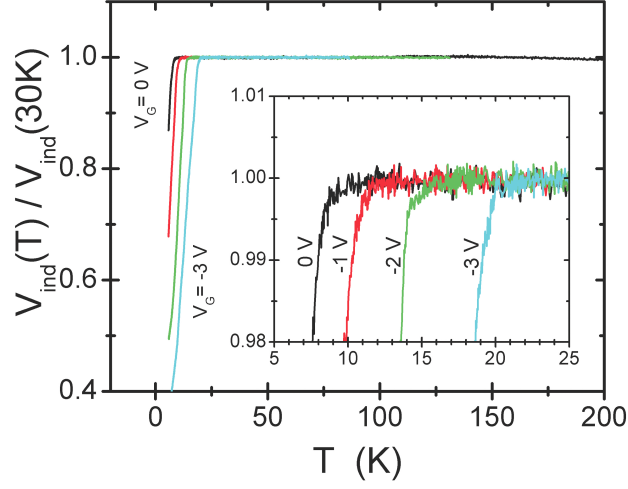


Figure 3.5 – Temperature dependence of mutual inductance for another device using an Au top gate and the ionic liquid electrolyte DEME-TFSI. Originally published in [1].

3.1.1 Magnetic Susceptibility and EDLG

To make sure that the shift in T_c described above was complete, we measured the diamagnetic response of the sample under different V_g . The shift in the onset of the induced signal proves that indeed the onset of superconductivity is changing as a result of EDLG. (See figure 3.5) These measurements were done by Dr. Joonah Yoon.

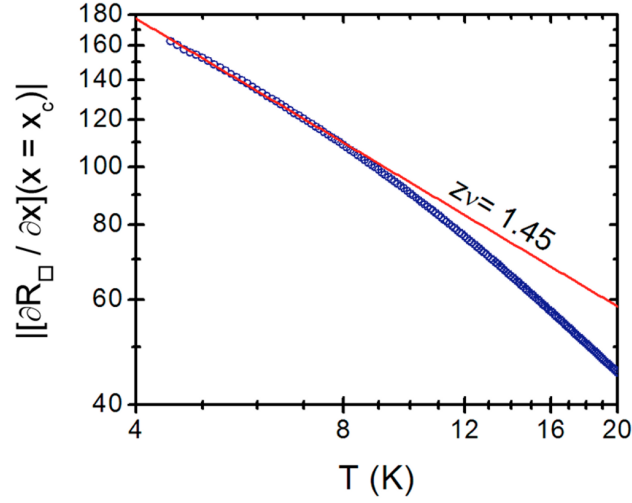


Figure 3.6 – Alternative way of determining $z\nu$ by forcing the scaling, plotting on a logarithmic scale and thus determining the limits of the power-law dependence. Originally published in [1], Supplementary Information.

3.1.2 Alternative Determination of the Critical Exponents $z\nu$

From the scaling of the resistance per square $R_{\square}(x, T) = R_c F(|x - x_c|^{-\frac{1}{z\nu}})$ one can derive an alternative method of determining the value of $z\nu$. [103, 104] We first evaluate the derivative of the resistance per square with respect to x at the critical value x_c :

$$\left. \frac{\partial R_{\square}}{\partial x} \right|_{x=x_c} = R_c F'(0) T^{-\frac{1}{z\nu}} \quad (3.3)$$

where $F'(0)$ is a constant. Then we plot the absolute value of $\left. \frac{\partial R_{\square}}{\partial x} \right|_{x=x_c}$, the slope of $R_{\square}(x)$ at the critical point x_c (See figure 3.3), as a function of T on a log-log scale. (See figure 3.6) Finally, we fit it to a straight line with the slope equal to $-\frac{1}{z\nu}$.^b

$$\log \left| \left. \frac{\partial R_{\square}}{\partial x} \right|_{x=x_c} \right| = \log |R_c F'(0)| - \frac{1}{z\nu} \log T \quad (3.4)$$

^b This paragraph was adapted from [1], Supplementary Information.

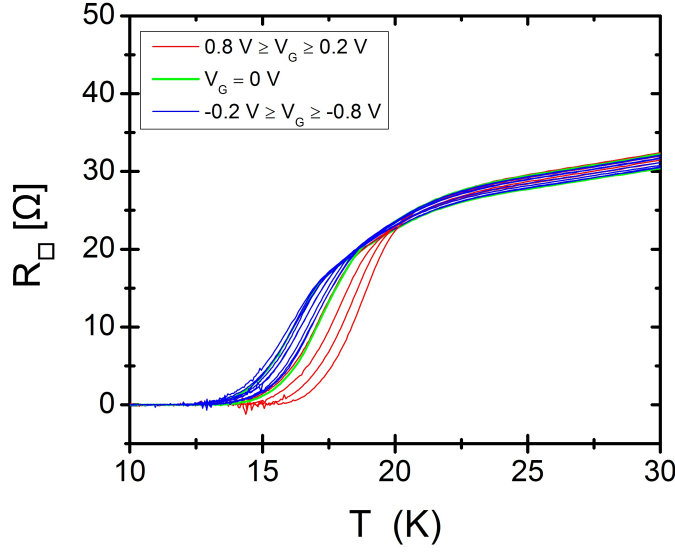


Figure 3.7 – Field effect on overdoped $\text{La}_{2-x}\text{Sr}_x\text{CuO}_4$. Originally published in [3].

3.2 Field Effect on Overdoped $\text{La}_{2-x}\text{Sr}_x\text{CuO}_4$

We did not investigate heavily the overdoped side of $\text{La}_{2-x}\text{Sr}_x\text{CuO}_4$. This has mainly to do with the fact that it is difficult to see T_c reduced in the top layer of a sample when there is shunt with a higher T_c lower in the sample. Nevertheless, in a few cases we could see a gating effect where a positive gate would increase T_c , while also increasing the resistance in the normal state. Here I present the case of an overdoped sample composed of 20 unit cells of metallic buffer and 2 unit cells of $\text{La}_{2-x}\text{Sr}_x\text{CuO}_4$ nominally doped with $x = 0.18$. (See figure 3.7) In this case, the shift in T_c was $\sim 5\text{K}$.

These results can help us to better understand the phenomenon of superconductivity, especially when combined with similar studies on other materials in the cuprate family. This will be discussed in the next chapter.

4 Discussion

While our observation of the pair quantum resistance should be confirmed at lower temperatures, it is worth noting that similar values have been reported earlier by several groups. The superconductor-to-insulator transition (SIT) in cuprates and other superconducting materials has been a subject of great interest and intense research by numerous groups. In these studies, one of the key parameters to be determined from the measured data is the critical resistance separating the two phases. In fact, for thin films, a more informative quantity is the sheet resistance ρ/d_f , where ρ is the material resistivity and d_f the film thickness. Bulk cuprates can be perceived as native superlattices in which metallic copper-oxide layers alternate with insulating layers, so they can also be characterized by the sheet resistance per one metallic layer, $R_{\square} = \rho/d$, where d is the distance between neighbouring metallic layers.^a

It is remarkable that this critical sheet resistance seems to be approximately equal to the quantum resistance for pairs, $R_Q = \frac{h}{4e^2} = 6.5 \text{ k}\Omega$ in a multitude of materials. As shown above, we have observed this in ultra-thin (1 unit cell thick) $\text{La}_{2-x}\text{Sr}_x\text{CuO}_4$ films where the carrier density was tuned and the SIT achieved by an applied electric field. Independently, similar result was obtained in thin $\text{YBa}_2\text{Cu}_3\text{O}_{7-\delta}$ films by Allen Goldman's group.[87] A question can be raised whether these findings may be peculiar to ultra-thin films. But as shown later, reported transport data in bulk single crystals of various cuprates also show the critical sheet resistance close to $6.5 \text{ k}\Omega$.

4.1 Experimental Challenges

Although it may look straightforward at the first glance, it turns out that measuring R_c at the SIT in cuprates is quite demanding. Several approaches have been pursued. The cleanest one may be to vary the carrier density in an ultra-thin film by applying an electric field, like in a field-effect transistor (FET). However, note that ultra-thin

^a This chapter was adapted from [5].

films are rarely grown directly on a substrate; in most cases, a buffer layer is needed to nucleate the growth and alleviate the substrate-film interaction. This buffer layer creates a parallel conductance path, and thus the measured critical resistance is lower than the one in the actual ultra-thin film under study. One could attempt to measure the substrate with a buffer, but without the active film independently and then try to separate the two contributions; however, this procedure is subject to errors of various origins and unknown magnitude. It is thus preferable to use highly resistive substrates and buffers. In fact, at zero gate voltage, the sample should be sufficiently insulating altogether. If R_0 is the resistance of the sample before applying the electric field, and R with the field applied, and if $R \ll R_0$, the error in estimating the change in the resistance of the (topmost) part of the sample that is affected by the field is directly proportional to the fraction R/R_0 , which in a good approximation represents the parasitic shunt resistance of the under-layer.

In the case of $\text{La}_{2-x}\text{Sr}_x\text{CuO}_4$, the dielectric screening length along the c -axis (i.e., perpendicular to the CuO_2 planes) is about $6 \pm 2 \text{ \AA}$; this is roughly equal to the distance between the neighbouring CuO_2 planes. Thus, when the carrier concentration in the first active CuO_2 layer reaches the critical value ($x \approx 0.06$), the second layer, buried half-a-unit-cell deeper, reaches a carrier concentration smaller by a factor of e , i.e. $x \sim 0.02$, and hence does not provide a significant parallel conductance path.[1] Thus, in the absence of conductive buffer layers, one could reasonably equate the measured critical sheet resistance with that in the topmost CuO_2 layer that is tuned through the SIT by the applied electric field - provided that this layer is atomically smooth and perfect. If, on the contrary, surface roughness is significant, this layer may be broken into islands that are disconnected, or weakly (Josephson) coupled. In this case, the cross-section of the metallic and superconducting path can be significantly reduced compared to the assumed ideal case, and one can grossly overestimate the intrinsic critical resistance. The same may happen if the film is granular and disordered, and the (super)conductive path is filamentary and percolative. Even the surface steps that originate from the inevitable substrate miscut may add a series resistance and artificially increase R_c ; to account for this, one may need to orient the device in parallel to the atomic steps induced by the miscut, or measure a set of devices fabricated with different orientations.

Even if the topmost CuO_2 layer is atomically perfect after the film deposition, it may cease to be so once the film is exposed to air, because of surface contamination and chemical reactions such as formation of hydroxides and carbonates. In addition, electronic disorder may be introduced by the adsorbed ions.

The above key sources of over and underestimates of R_c are independent, i.e., they can combine in various ways. Thus, the critical resistance observed at the SIT quantum critical point is inherently “fragile” - the intrinsic value is easy to miss since it can be masked by various extrinsic factors.

Some of the above surface-sensitivity problems can be alleviated by working with thick, bulk, single crystals, and tuning the free carrier density by chemical doping rather than by the field effect. This, however, poses new challenges. In thin-film field-effect studies, one can work with a single sample and tune it through the SIT as finely as desired, by controlling the gate voltage and the charging time. This is not possible in bulk single-crystal studies; rather, for every carrier concentration one must synthesise a separate sample. The question then arises how many samples can one realistically generate and study, how accurately can one measure the sheet resistance (per CuO_2 layer) in samples of irregular shape and contact geometry, and how accurately can one tune and measure the doping level. In practice, in most studies only a small number of crystals is studied, with doping steps of $\delta x = 0.01$ or larger, with about the same uncertainty. For these reasons, in bulk crystal studies, it is very hard (if not impossible) to tune the carrier concentration to precisely the critical point.

The upshot is that by combining the work on thin film and single crystals, one can walk up two independent pathways to the physics of the SIT in cuprates. In what follows, we will show that both point to the same key conclusion: existence of localised pairs on the insulating side of the SIT.

4.2 On Thin Film Studies by Other Groups

In an early work, Walker and coworkers studied single-crystal thin films of $\text{YBa}_2(\text{Cu}_{1-x}\text{Zn}_x)_3\text{O}_{7-\delta}$. [105] With x and/or δ increasing, they observed the SIT when the sheet resistance per one unit cell (i.e., per one copper-oxygen bilayer) reached $R_c \approx R_Q = \frac{h}{4e^2} \approx 6.5 \text{ k}\Omega$, for various combinations of $0 < x < 0.07$ and $0.05 < \delta < 0.67$. (See figure 4.1) The films were grown by pulsed laser deposition on SrTiO_3 substrates from targets with various x and δ compositions. There were no buffer layers between the substrates and the films. The resulting film stoichiometry was determined after growth by electron probe microanalysis. In that paper, the exact film thickness of the films used was not reported, although the authors claimed that the thickness was measured after the growth with an absolute error of about 10–15% and a film-to-film variation of 1%. The measured resistivity was given, from which the sheet resistance was calculated knowing the distance between CuO_2 bilayers. Thus, in a sense, this experiment was more similar to bulk crystal measurements, with the advantage of a better defined geometry, than to the subsequent ultra-thin film measurements described below. Nevertheless, by showing that the SIT occurred invariably at the same sheet resistance, this work strongly hinted that the observation of $R_c \approx R_Q$ was not just a coincidence but rather a signature of some fundamental and universal phenomenon.

Applying the same electric double-layer technique as the one I used in this thesis on ultra-thin $\text{YBa}_2\text{Cu}_3\text{O}_{7-\delta}$ films grown by sputtering, Goldman's group was also able to traverse the SIT at the critical sheet resistance of about $6 \text{ k}\Omega$ (See figure 4.2), a result

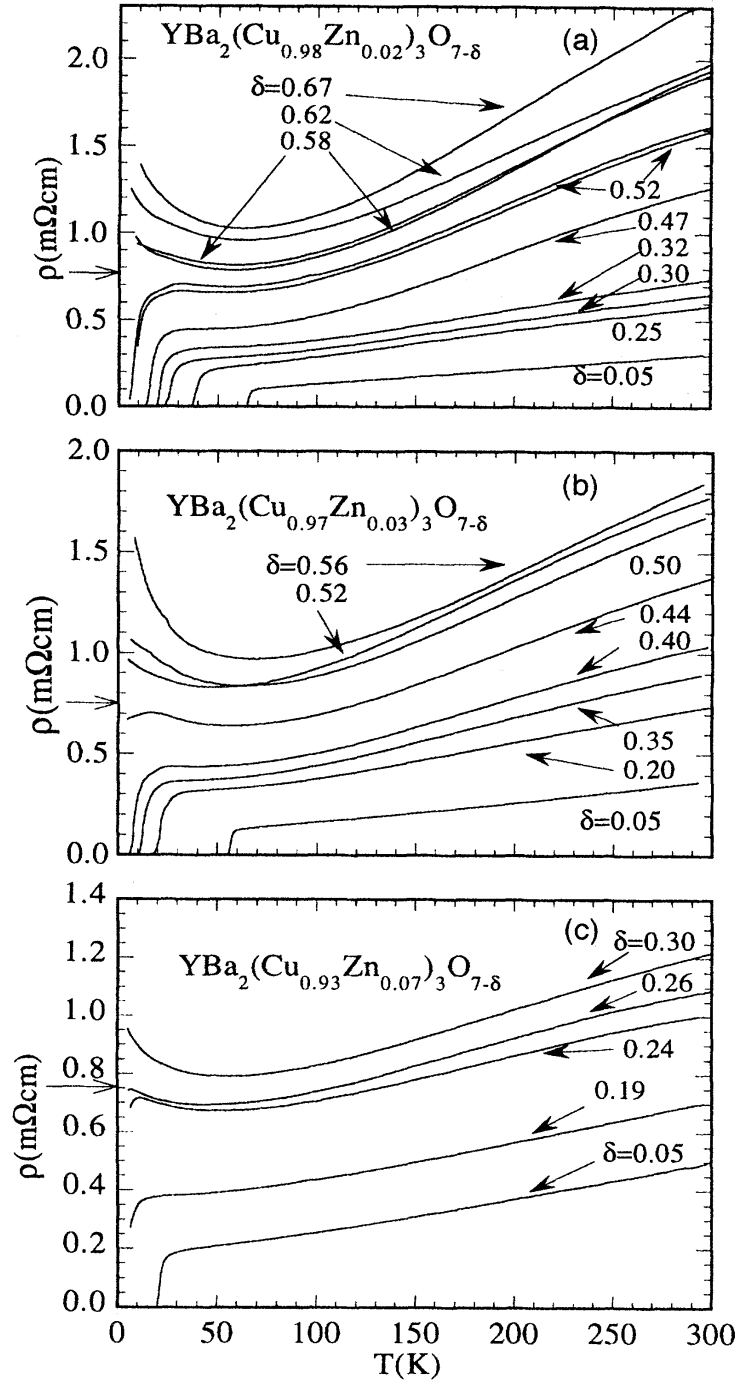


Figure 4.1 – Superconductor-to-insulator transition in $\text{YBa}_2(\text{Cu}_{1-x}\text{Zn}_x)_3\text{O}_{7-\delta}$ occurring at a similar value even if induced by different combinations of x and δ . The arrow on the ordinate indicates the sheet resistance of $h/(2e)^2$ per unit cell. Reprinted from [105]. Copyright 1995 by the American Physical Society.

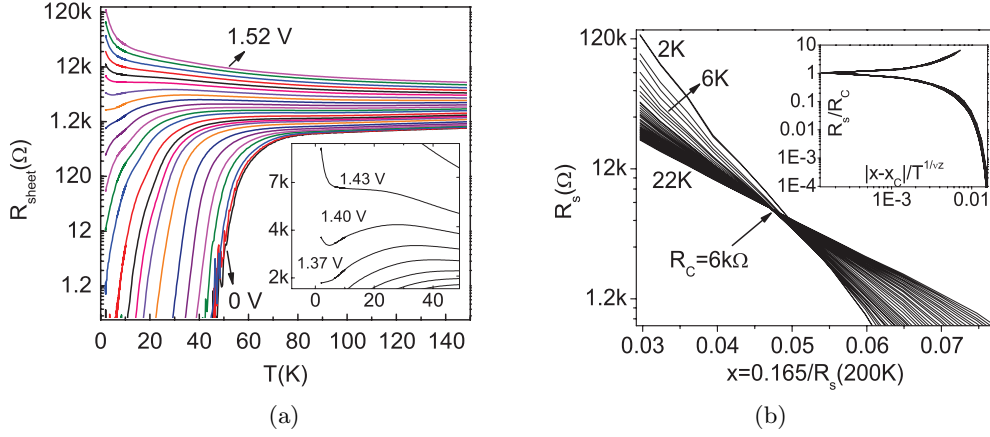


Figure 4.2 – (a) A thin $\text{YBa}_2\text{Cu}_3\text{O}_{7-\delta}$ film is tuned through the SIT by applying a gate voltage between 0 and 1.52 V. It shows a critical point at $R_{\square} = R_c = 6k\Omega$ [87]. (b) Collapse of the resistance data for multiple doping levels, in the temperature range 2 K to 22 K, on a universal double-valued function, showing a quantum critical point at $R_c \approx 6k\Omega$. Reprinted from [87]. Copyright 2011 by the American Physical Society.

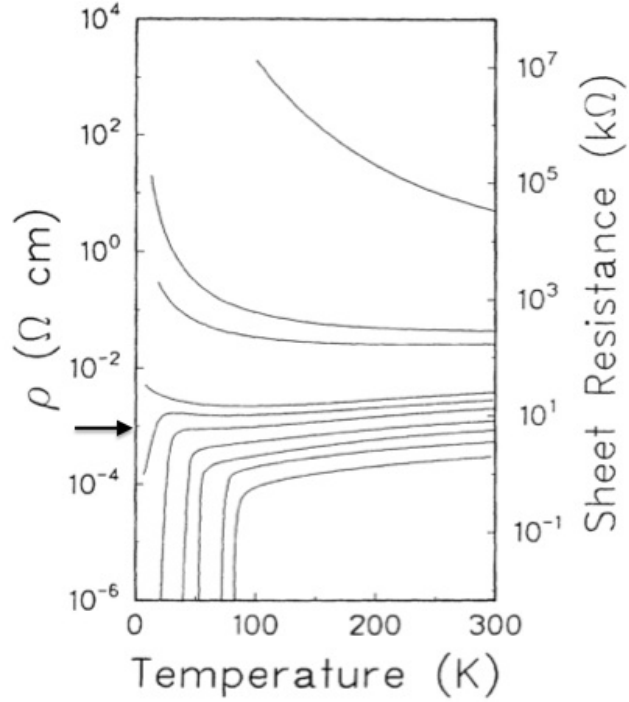


Figure 4.3 – Temperature dependence of the resistivity (left scale) of $\text{Bi}_2\text{Sr}_2\text{Y}_x\text{Ca}_{1-x}\text{Cu}_2\text{O}_8$ single crystals. On the *right scale* is the sheet resistance per CuO_2 double layer. One of the first observations of the critical sheet resistance at around $h/(2e)^2$ (indicated by the arrow). Adapted from [106]. Copyright 1991 by the American Physical Society.

compatible with the quantum resistance of pairs [87]. In this case, the 7 unit-cell thick films were grown using a high-oxygen-pressure sputtering system. Their task was quite difficult, given that $\text{YBa}_2\text{Cu}_3\text{O}_{7-\delta}$ films are very sensitive to atmosphere exposure, so it is quite striking that the critical sheet resistance was again found near R_Q .

Several other studies of SIT in cuprate thin films also showed similar critical sheet resistance, although without particular emphasis on this fact. One example is the work of Oh *et al.* on $\text{Bi}_2\text{Sr}_{2-x}\text{La}_x\text{CaCu}_2\text{O}_{8+\delta}$ thin films [107] where the SIT was approached by La doping $x = 0.44$ and then crossed by precise and reversible oxygen control, with the critical CuO_2 bilayer sheet resistance $R_c \approx 7.7\text{--}9.0\text{ k}\Omega$. Xu *et al.* [108] studied 100 nm thick $\text{Nd}_{1.78}\text{Ce}_{0.22}\text{CuO}_{4\pm\delta}$ films and found $\rho_c \approx 300 \pm 50 \mu\Omega\text{cm}$, corresponding to $R_c \approx 5 \pm 1\text{ k}\Omega$ per CuO_2 plane.

4.3 On Single Crystal Studies by Other Groups

One of the earliest studies in single crystals with doping near the SIT was done by Mandrus *et al.* [106]. Working with a set of $\text{Bi}_2\text{Sr}_2\text{Y}_x\text{Ca}_{1-x}\text{Cu}_2\text{O}_8$ single crystals, with the yttrium content in the range $0 \leq x \leq 0.8$, they measured the temperature dependence of the *ab*-plane electrical transport and spanned the SIT transition from both sides. (See figure 4.3) From the measured resistivity, the sheet resistance was calculated by dividing it by the distance between the CuO_2 bilayers ($d = c/2 = 15.3 \text{ \AA}$). The separatrix between insulating and superconducting sets of curves extrapolated to about $R_c \approx 8\text{ k}\Omega$. From this result, they claimed that the transition is two-dimensional, and that the critical resistance is close to $R_Q \approx 6.5\text{ k}\Omega$, the quantum resistance for pairs.

Working with underdoped $\text{YBa}_2\text{Cu}_3\text{O}_y$ twinned crystals, Semba and Matsuda studied the SIT driven by carrier concentration. They observed the threshold resistivity $\rho_{ab}^{\text{SI}} \approx 0.8\text{ m}\Omega\text{cm}$; considering the bilayer spacing of $d = 11.8 \text{ \AA}$ [109], this corresponds to the critical sheet resistance of $6.5\text{ k}\Omega$ per CuO_2 bilayer. They assumed that the nearest 2 neighbour CuO_2 planes are coherently coupled. (We know from ARPES studies in an analogous material, Bi-2212, that the two proximal CuO_2 planes are strongly coupled and that the relevant electron wave functions overlap, since a significant band splitting is observed between the bonding and anti-bonding combinations [108, 110].) Observing that in a sample just on the insulating side of the transition, the in-plane resistivity ρ_{ab} and the out-of-plane resistivity ρ_c diverge logarithmically down to 4.2 K, while their anisotropy remains almost constant for $T < 100\text{ K}$, they interpreted their findings as pointing to Cooper pair localisation, and to a crossover from a temperature-independent quantum phase-fluctuation region to a temperature-dependent classical phase-fluctuation region.

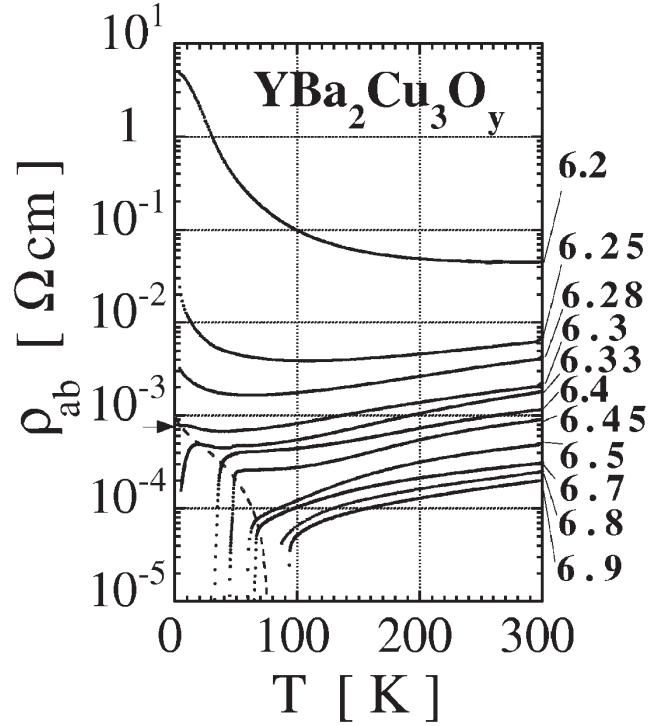


Figure 4.4 – Temperature dependence of the in-plane resistivity at the SIT in $\text{YBa}_2\text{Cu}_3\text{O}_{7-\delta}$ single crystals. The transition takes place at $y \approx 6.3$. The threshold resistivity corresponds to a sheet resistance of $6.5\text{k}\Omega$ per CuO_2 bilayer (indicated by an *arrow*). Reprinted from [109]. Copyright 2001 by the American Physical Society.

4.4 Concluding Remarks and Outlook

I have omitted from this discussion several other papers showing the SIT in cuprates at a different value of sheet resistance. At this point, it is not possible to tell the reason for these discrepancies, other than to repeat that numerous extrinsic factors could shift the apparent R_c in either direction. More work is needed, by different groups, using various techniques and studying different cuprate materials, before all the questions are settled.

Nevertheless, there is already substantial evidence that the quantum resistance for pairs, $R_Q = \frac{h}{4e^2} \approx 6.5\text{k}\Omega$, appears prominently at SIT in several p -doped cuprate superconductors. The key structural element seems to be a single, (quasi) two-dimensional superconducting slab. The detailed structure and thickness of this slab do not seem to play a role: YBCO and Bi-2212, where pairs of proximal CuO_2 planes are strongly coupled and act as a single SC sheet, behave very similar to $\text{La}_{2-x}\text{Sr}_x\text{CuO}_4$ and other cuprates where the CuO_2 planes are isolated or very weakly coupled. This gives more credibility to the hypothesis that pairs exist, although localised, already on the insulating side, and that with increased

doping these preformed pairs become mobile and eventually form a superfluid Bose condensate.

Most of the cuprate studies reviewed here were conducted only above the liquid helium temperature. One could rightfully object that a quantum phase transition (QPT) happens at $T \rightarrow 0\text{K}$, and that 4K is much too high a temperature to claim that a QPT has been observed. Certainly we may learn more about the SIT in cuprates by extending these studies to much lower temperatures. In our own group, experiments are underway now down to liquid ^3He temperature (300mK). Nevertheless, we believe that the unified picture seen by various methods in various cuprates is unlikely to be accidental and is probably pointing to some intrinsic and relevant physics.

5 Other Explored Avenues

5.1 Low Temperature Measurements

After our initial positive results, our main goal was to repeat this experiment at lower temperatures. We are very aware that as soon as there is a fanning of curves or a crossing point, there can be mathematically observed a scaling due to the simple effect of a first order Taylor expansion that has absolutely no physical meaning. The goal should be to observe this scaling over a much broader range of temperatures, ideally several orders of magnitude. This is the only way to validly claim that the scaling in question proves the existence of a quantum critical point in the underdoped limit of the superconducting dome in $\text{La}_{2-x}\text{Sr}_x\text{CuO}_4$, and that it is not just a mathematical artefact. While we immediately started preparing multiple samples for measurements at low sub-kelvin temperatures, we found out the hard way that our gold contacts were not reliable enough to proceed with these experiments. Their breaking point was not predictable, i.e., some samples would survive tens of thermal cycles, while others would break after only a few cycles. This was not acceptable when planning to measure a sample in a ^3He cryostat or a dilution fridge. In this case we need to work with a decent level of confidence that the measurement would succeed. One of the developments resulting from this work was a more compact lithographic pattern (See figure 2.6) with provisions to allow to cut the substrate in four 3mm by 4mm pieces using a diamond dicing saw, without affecting the devices. The printed circuit board sample holder was replaced by a miniaturised version based on a standard 8 pin chip holder. (See figure 5.1) These adaptations were needed in order to be able to fit the sample, with the IL covering it, in the limited space of the dilution fridge we were planing to use.

While we were not able to execute these measurements during the time given for this thesis, we can say that because of the recent break through we got through the use of room temperature sputtered polycrystalline strontium ruthenate as contact material, we are confident that low temperature measurement will be feasible very soon. (See chapter 2.2.5)

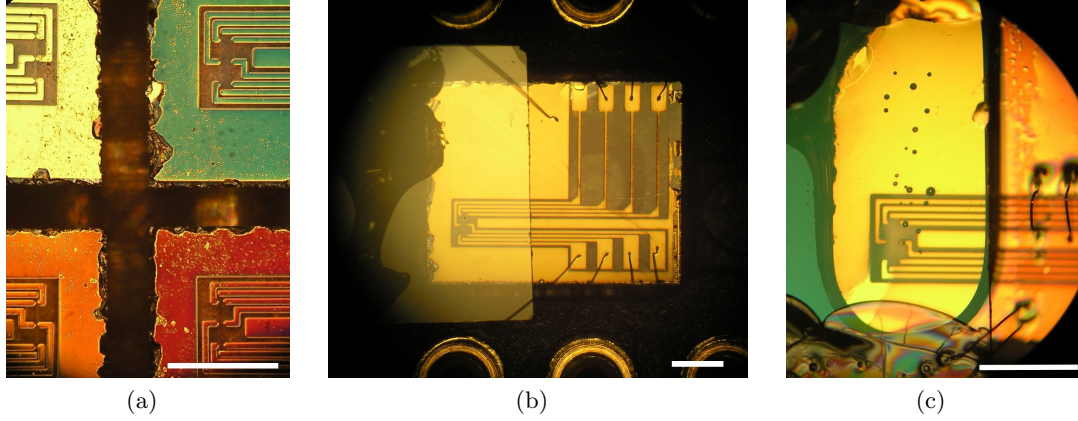


Figure 5.1 – Sample #1173. The white bar indicates 1 mm in each picture for scale. (a) shows the sample after dicing using a diamond blade. Ragged edges, as well as some debris, are clearly visible. Colours are artefacts of the polarising filters used. In (b) one device has been mounted on the miniaturised sample holder. The glass cover slide on the left is there to hold the IL in place (no liquid present yet). (c) IL on the sample. One clearly sees how the edge of the glass cover slide keeps the liquid in place by fixing the meniscus. Over the gate, a few bubbles are visible. They are usually generated when too high gate voltage has been applied.

5.2 Field Effect on other Materials, Illustrated by WO_3

We tried to apply EDLG on other materials, such as FeTe, diamond, graphite, graphene, infinite-layer compound ... In none of these did we have so far any real experimental success that we should report. In the case of diamond, the difficulties were to get a perfectly flat surface, and that, if not initially slightly doped by nitrogen impurities, it was too resistive to allow a buildup of the electric field. Often the measurements were hampered by contact issues. In the case of graphite and graphene, the main issue was the breaking of the contacts when exposed to IL, due to an exfoliating effect of the IL on graphene. Our best success was the metal-to-insulator transition that we induced in WO_3 , as reported next. We chose this material as, when doped with various elements, it can be a superconductor with a T_c of a few kelvin.[111] But what makes this particularly worth investigating under EDLG is that there have been reports of possible 2D surface superconductivity in Na- and H-doped WO_3 at $\sim 90\text{K}$ and $\sim 120\text{K}$, respectively.[112–114]

5.2.1 On WO_3 Sample Preparation

It took considerable experimental effort to improve the sputtering conditions up to the point where atomically flat samples could be grown. This work was done by Dr. Juan Pereiro, Dr. Jure Strle, and later Dr. Xiang Leng, while I focused on the transport measurements. The films were grown on $\text{La}_{0.18}\text{Sr}_{0.82}\text{Al}_{0.59}\text{Ta}_{0.41}\text{O}_4$ and YAlO_3 substrates

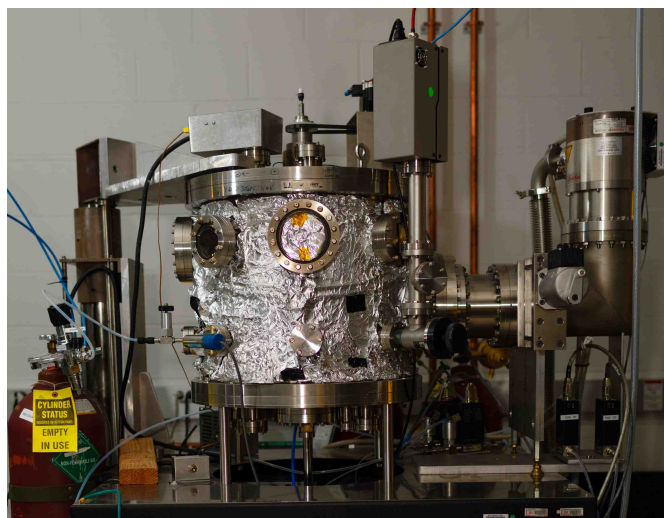


Figure 5.2 – Sputtering chamber used to grow WO_3 films.
Photo credit: Dr. Xi He.

using radio frequency sputtering. This resulted in atomically flat films with a RMS roughness of the order of 0.2nm.

After the films were grown, they were patterned by standard and e-beam lithography. (Done by Dr. Anthony Bollinger and Nicholas Litombe.) For the first samples we used a set of slits of various thicknesses, optimal for high resistivity samples. The contacts were made by evaporated gold, and covered by an insulating amorphous Al_2O_3 layer of several hundred nanometers in thickness. This was a necessary protection against delamination of the gold contacts under the influence of the IL. A small window was kept uncovered to allow electrical connections to the sample. After patterning, the sample was connected to a sample holder by wirebonds and a platinum mesh top gate was placed over the part of the sample to be covered by IL. Initial measurements, without ionic liquid, showed a strongly resistive behaviour.

In later iterations, we found out that we could replace gold contacts by sputtered tungsten. The $\text{W}-\text{WO}_3$ proved to be much more stable than the $\text{Au}-\text{WO}_3$ contacts. With these contacts we were able to design smaller devices. It was decided to reduce the size of the samples down to tens and hundreds of nanometers with the aim of having devices fitting on a single or just a few atomic terraces, respectively. This should enable to maximise any effect. For this reason, we invested time in e-beam lithographic patterning of a few of the WO_3 samples. As a result of this miniaturisation, we also had to adapt the gates. Instead of a coplanar gate, or a platinum mesh top gate, we used a single platinum wire formed in a loop, hovering just above the nanobar, as a top gate. A sub-microliter droplet of IL was then placed on top of this loop, in order to also wet the device. (See figure 5.3) The surface tension of the droplet was sufficient to keep it from moving.

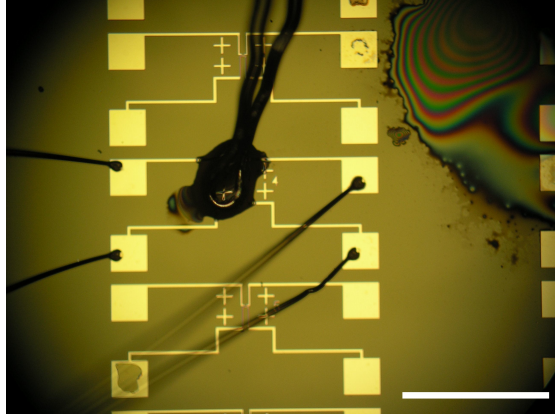


Figure 5.3 – WO_3 nanowire (60nm thick, $2.5\mu\text{m}$ long and 110nm wide), at the centre of the four alignment crosses, near the number 4 mark. On top of the nanowire, one sees a platinum wire loop serving as the gate. This loop is placed so that a minute drop of IL DEME-TFSI is held in place by surface tension alone. In bright yellow one sees the 4 tungsten-gold contacts that are connected through wire-bonds to allow for a 4 point measurement of the resistance. The scale bar is 1mm long.

5.2.2 Transport Results

Our measurements showed initially highly resistive samples, with resistances of the order of $30\text{k}\Omega$ per square at $T = 250\text{K}$. Upon cooling, these uncharged samples rapidly reached resistances too high to be accurately measured with our setup. After applying a positive gate voltage (i.e., inducing negative charges in the sample), the resistance of the sample rapidly fell by a factor of 5 at the charging temperature $T_{\text{charge}} \approx 250\text{K}$. This corresponds to a change of more than 4 orders of magnitude at 4K . While other sample geometries (shorter and wider bar) would have allowed to measure more accurately the resistance of the uncharged sample, the geometry chosen was optimised to measure the low resistance in the metallic state (reached when charging at around $+2\text{V}$, where the resistance was of the order of hundreds of ohms). See figure 5.4 for a detailed resistance measurement. While longer charging times and higher charging temperatures allowed to maximise the induced carrier density, and thus minimise the measured resistivity, a saturation level was reached at which point it was not possible to further reduce the resistance of the samples. Increasing V_g at this point would result in a reversal of the obtained charging effect, and an increase in the resistance of the device. This saturation level depended on the thickness of the sample, indicating that the gating effect is not limited to the surface of the device.

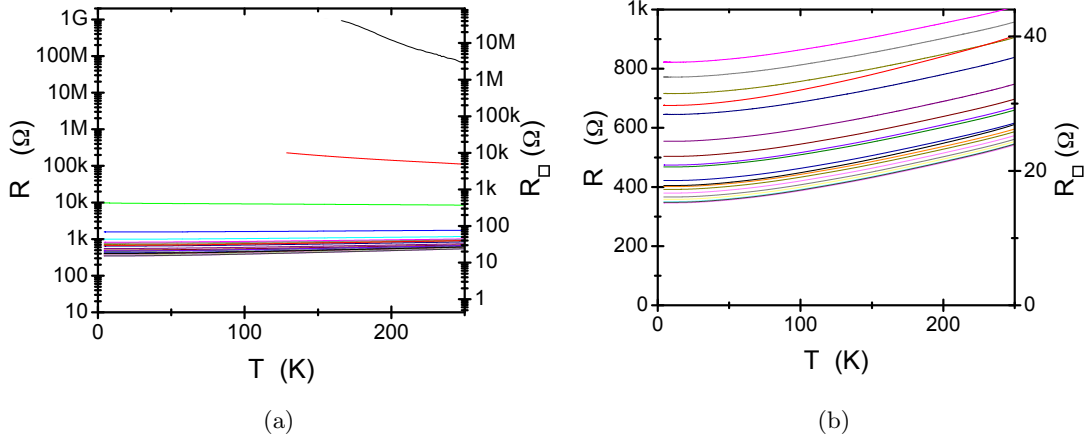


Figure 5.4 – Four point resistance measurement on a WO_3 film, sample S89A4, width 110nm, length $2.5\mu\text{m}$. (b) shows a zoomed in version of (a) on a linear scale that clearly indicates that a metal-to-insulator transition has been induced by EDLG.

5.2.3 Discussion

While our goal to induce superconductivity in WO_3 did not yet succeed, we nevertheless induced a metal-to-insulator transition in this material. At low temperature, a change in conductivity of several decades was observed. We used two gate dielectrics, PEG-NaF and DEME-TFSI. Except for the difference in charging temperature, there was no significant difference in the amplitude of the effect on WO_3 . We also worked with samples of very different sizes, from microscopic to nanoscopic, again without any significant difference in behaviour. Some thickness dependence studies seem to show that in this case the effect of EDLG is not limited to the surface of the film, but extends to the volume of the WO_3 film. More details will be given in a future publication. [Xiang *et al.*, to be published]

I am convinced that EDLG is an invaluable tool that will be helpful to uncover interesting physics, and one of the most striking examples was the superconductivity induced in SrTiO_3 as reported by Ueno *et al.*[45].

5.3 Differential COBRA

After our initial measurements showed such a large effect on $\text{La}_{2-x}\text{Sr}_x\text{CuO}_4$, it was a natural next step to try to understand what exactly is happening at the interface at a microscopic level. While the standard assumption is that EDLG generates a true electronic doping near the surface, similar to a silicon based FET, our results on WO_3 (See section 5.2) indicate that under certain circumstances, or combinations of IL with a particular sample, the electric gating effect can affect the entire volume of the film, even when it is over 50 nm thick. Furthermore, it has been shown that dielectric gating can lead to the formation of oxygen vacancies in VO_2 . [84] It must be noted that in this case, not only did EDLG induce the vacancies deep into the film, but furthermore, this was a reversible effect, with oxygen being exchanged with the surrounding environment. This shows once more how poorly understood the interaction between the IL and the sample still is. The knowledge derived from the study of supercapacitors [115–117] is only of limited help when trying to use the EDLG technique as a physicist’s tool. While in some cases one may indeed have a true textbook electronic doping effect, it is likely that in other cases intercalations of ions into the film, vacancy creation or ionic displacements may be at the core of the effect. Our aim in this experiments was to clarify which of these mechanisms is dominant in the case of EDLG on $\text{La}_{2-x}\text{Sr}_x\text{CuO}_4$. It is particularly important to understand this effect at a microscopic level, now that the ELDG technique has been applied to numerous materials. (See table 1.1)

In an earlier work, Coherent Bragg Rod Analysis (COBRA) had successfully been used to determine the complete atomic structure of $\text{La}_{2-x}\text{Sr}_x\text{CuO}_4$ films [118]. This technique allows to measure the 3 dimensional electron density in thin films. A more refined technique, energy differential COBRA, has also been used on similar films. In this case by measuring the diffraction intensity along the Bragg rod with two X-ray energies bracketing the Sr absorption edge (used as dopant in $\text{La}_{2-x}\text{Sr}_x\text{CuO}_4$), it is even possible to determine the concentration of Sr layer by layer [119]. Thus it is possible to exactly determine the atomic structure of the material. Our goal was to combine this proven technique with EDLG by applying a high electric field using the EDLG in-situ during a COBRA diffraction measurement.

5.3.1 Wet Chemical Sample Cell

First Beamtime

For our first attempt at COBRA combined with EDLG, we used a sample holder similar to the ones we had used for transport measurements. It consisted of a simple PCB board sample holder with a sheet of Kapton (7 μm thick) floating on the drop of IL to hold it down (See figure 5.5 and 5.6). The PCB board was itself fixed to the vacuum chamber using molten wax. The 10 mm by 10 mm sample is cut into two symmetric

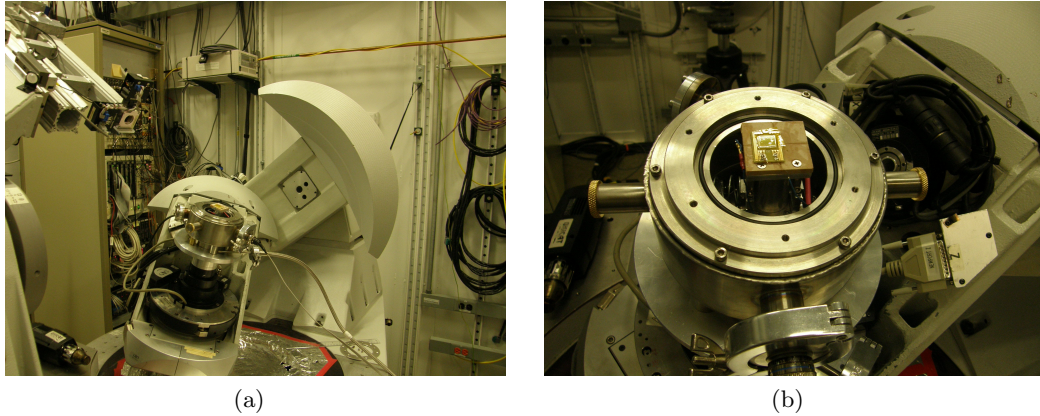


Figure 5.5 – Two views of the sample installed on the goniometer during the first attempt at combining COBRA with EDLG on $\text{La}_{2-x}\text{Sr}_x\text{CuO}_4$. The vacuum chamber is closed by a beryllium dome that has been removed in these pictures to show the sample.

halves (each 5mm by 10mm), with one side playing the role of gate for the other. Each side has a small gold contact (300 μm by 300 μm) that allows to connect to it and apply a gate voltage between them. The relative uniformity of the IL layer was obtained by first placing a few drops of IL on the sample, laying a little piece of Kapton foil on top of these drops, and then pressing the foil on the sample using a piece of polished silicon wafer. In the vacuum chamber, the sample sits on a piezoelectric tilt stage, itself fixed on a linear translation stage that allows for a movement of approximately 3mm to alternatively expose different parts of the sample to the X-ray beam. The tilt stage allows to correct for misalignments between the two end positions of the translational stage. As this piezoelectric stage broke early during this very first beamtime, the actual measurements were done without taking full advantage of this configuration. The sample was held in a fixed position relative to the vacuum chamber. Thus only one side of the sample could be exposed to the X-ray beam, and no position differential measurement was possible.

From this first beamtime, we learned that we need a dedicated wet chemical cell to insure an IL layer as thin and as uniform as possible. Also, it became clear that it would be advantageous to have several contacts to each side of the sample in order to be able to characterise the transport properties in situ. This would be a beneficial diagnostic tool to determine the effect of the applied field on the sample before starting the diffraction measurement. Also, as can be seen in figure 5.6, DEME-TFSI was shown not to resist extended exposure to an intense X-ray beam. While during the first few hours of measurements we were able to observe some changes in the diffracted intensity as a function of the gate voltage, after approximately four hours this signal vanished, and when we opened the vacuum chamber and removed the Kapton tape, the beam damage

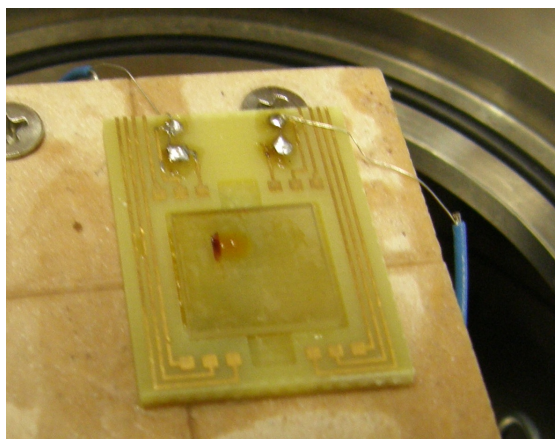


Figure 5.6 – Radiation damage after several hours of exposure to the APS X-ray beam. The brown spot is a solid mass of radiation damaged IL attached to the sample. This showed that the IL DEME-TFSI is not radiation resistant enough to allow the kind of long time measurement envisioned.

to the liquid was clearly visible, as a mass of polymerised IL attached to the sample at the point where the X-ray penetrated the sample.

Second Beamtime

For the second beamtime assigned to this experiment, we designed and built a new dedicated wet chemical cell, based on the lessons learned from the first set of experiments. The details of this design can be found in Appendix B. This new unique design allows to expose the sample (1 cm by 1 cm, 1 mm thick) to EDLG while at the same time keeping the layer of IL to a uniform and minimal thickness. This is critical for diffraction studies, as it allows to work with a uniform and predictable absorption of the intensity of both incident and diffracted beam by the IL. The sample surface is free of any obstacle so as to permit direct access to the beam, even at grazing incidence. The only difficulty is to keep the final connection to the sample surface as shallow as possible. For the spacial configuration of our setup, it was also important to reduce the size of the cell as much as reasonably feasible. A positive side-effect was that this also led to reducing the weight of the complete cell to less than 20 g, thus easing the load on the piezoelectric stage.

The cell body is made out of Kel-F, a material chosen for its chemical inertia and machinability. The cell also allows for two independent in-situ four point measurements. For this purpose, a row of eight holes, along one edge of the sample, in the central part is used to feed through electric wires that are sealed in place using TorrSeal[®] vacuum equipment high vacuum epoxy from Varian. (See figure B.1) This epoxy is chosen for its high chemical inertia and excellent vacuum compatibility. Its only disadvantage is a tendency to etch copper during curing. This is visible as a halo along the edge of the

epoxy where it touches the $\text{La}_{2-x}\text{Sr}_x\text{CuO}_4$ film. But this had no detrimental effect to the electrical connection to the film. The connection to the sample can be done using shallow wire-bonds. After bonding, all the exposed contacts are covered with epoxy for protection. (See figure 5.9a) Some small epoxy drops were also used to blunt the corners of the sample, as they are sharp enough to pierce the Kapton film when vacuum is applied to the cell. (See figure 5.9b) A single separate feed through hole allows to install a platinum wire that can be used as a gate. A Luer-Slip fitting on the side allows to attach a valve and to pull a rough vacuum on the IL; thus creating the uniform layer between the sample and the Kapton film. The vacuum was generated by manually pulling on a syringe and then closing the valve. This low vacuum, in combination with external atmospheric pressure, insures that there is an IL film of minimal thickness ($< 50\mu\text{m}$) covering the sample. Figure 5.9b shows the extent of the uniform layer of IL. Near the epoxy protecting the wire bonds, there is a small zone of non-uniformity that must be avoided by carefully centering the beam. Ideally this cell should be kept in a nitrogen or helium atmosphere during measurements to minimise beam damage to the Kapton film that could lead to a leak. As the current design was still too big to close the beryllium dome of our vacuum chamber, we chose to continuously flow nitrogen through an improvised nozzle on to the Kapton film. (See figure 5.8c) This was successful, as the cell performed well over several days of measurements without the need to restore vacuum, but should be remediated before the next beamtime. The only difficulty with this design was that after a few days of use, the IL film was discontinuous at the edge of the sample, thus opening the circuit applying the gate voltage between the platinum gate and the sample. This could be solved without opening the cell simply by releasing and then restoring the vacuum through the valve, locally redistributing the IL. The design of this cell was inspired by a similar cell ([26] and personal communication from Dr. Hua Zhou). It differs in that it is smaller, lighter and has a provision for in-situ transport measurements.

5.3.2 Experimental Procedure

We studied $\text{La}_{2-x}\text{Sr}_x\text{CuO}_4$ films grown on LaSrAlO_4 substrates by MBE at BNL. These measurements were done with a X-ray photon energy of 16keV. To avoid any effect of non-uniformity due to a not exactly repeatable positioning of the attenuation filters, no data was taken with attenuation filters in the beam. The original plan called for a voltage applied between both sides of the sample. The idea was that in this way the differential signal should be maximised, as both sides are exposed to a gate voltage of the same amplitude but different polarity. The goal was to measure diffraction intensity along a Bragg rod, while switching between both sides of the sample and thus measuring a differential signal. There are a few challenges with this approach:

- The sample needs to be a perfectly uniform single crystal film, so that the diffracted intensity from one side can be meaningfully compared with the diffracted intensity

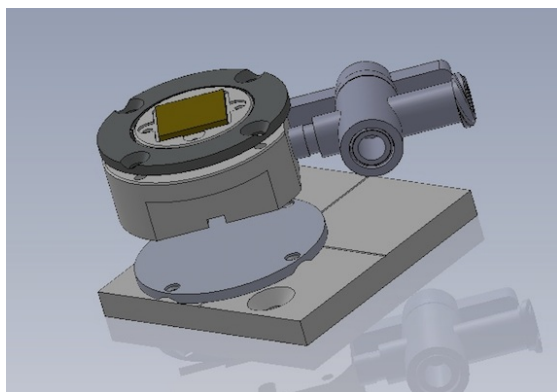


Figure 5.7 – SolidWorks rendering of the Wet Chemical Sample cell built to allow COBRA studies on a sample under EDLG. This cell was tested in our second beamtime. A stainless steel ring (dark grey) is used to push down a Kapton film ($7\mu\text{m}$ thick) not shown in this rendering against a Viton O-ring that insures a rough vacuum sealing. On the right, a PVDF stopcock valve allows to connect to a syringe and pull a rough vacuum on the cell.

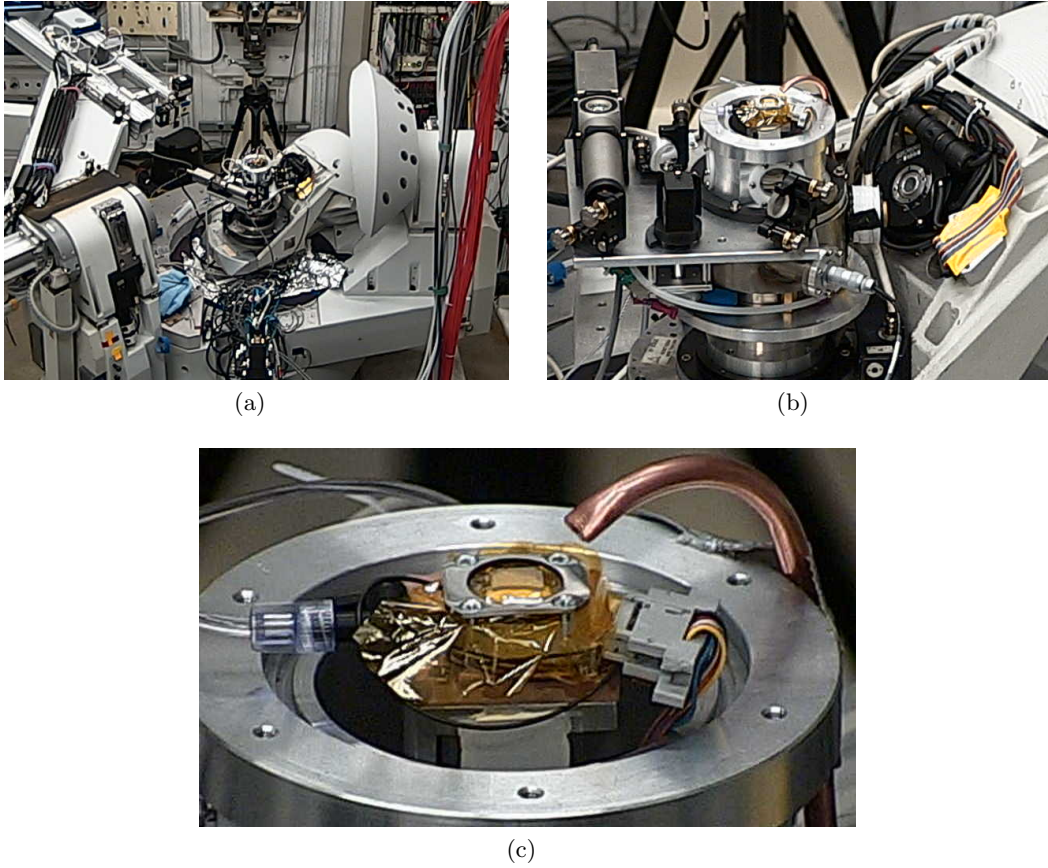


Figure 5.8 – Wet chemical sample cell mounted in the goniometer at the APS beam-line. In (b) one can see the autocollimator and optics used to measure the misalignment of the sample after movement of the translational stage. This is corrected using a tilt stage not visible in this picture. The copper nozzle is used to blow nitrogen on the Kapton film (yellow), to limit radiation damage that could lead to a leak of the cell. The transparent tube on the left of (c) is used to pull a rough vacuum on the cell. On the right, a grey electrical plug is used to connect to the feedthroughs for the gate and the transport measurements.

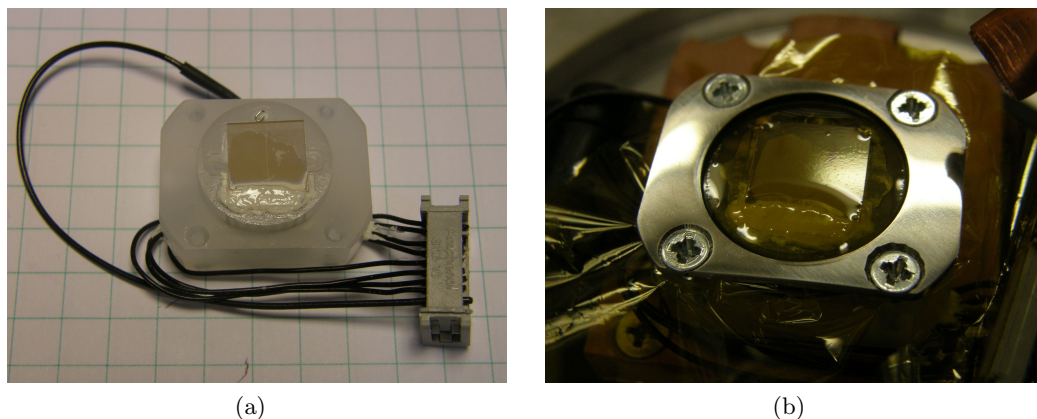


Figure 5.9 – Detailed view of the wet chemical sample cell. (a) before covering with Kapton film. The wire-bonds have just been covered by TorrSeal[®] (glassy white mass at the bottom edge of the sample) to isolate them from the IL. The sample is transparent, and thus some of the epoxy used under it is visible in transparency. One can see the vertical trench in the middle separating the sample in two equal parts. (b) After adding the IL and closing the cell with Kapton film, the rough vacuum is applied. One clearly sees that the IL film is uniform on at least 3/4 of the sample.

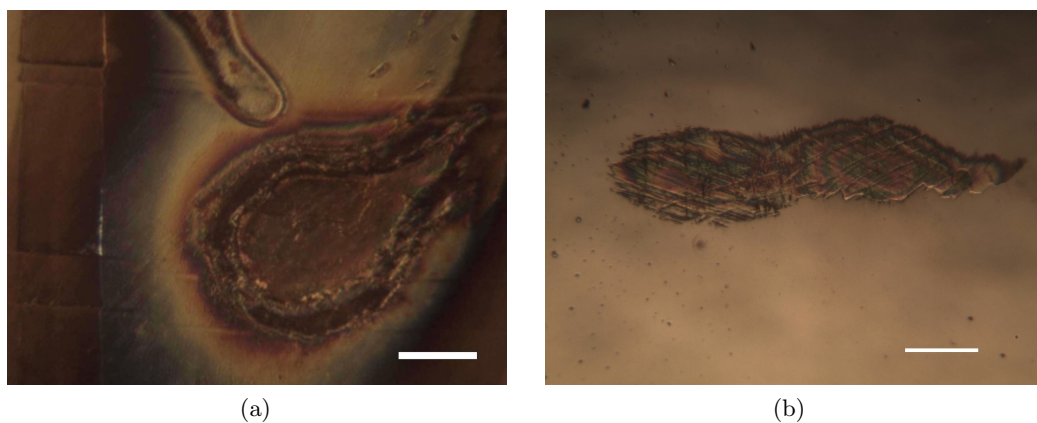


Figure 5.10 – Sample #1531: Beam damage after several hours of exposure to X-ray beam. (a) BMIM-PF₆ is etching a hole in the sample (b) With EMIM-DCA only a very light deposit on the sample is visible after the exposure. (Bar indicates 100 μm)

from the other. This means that the IL film must be as uniform as possible, so that its absorption can be neglected.

- The sample must stay perfectly aligned between two positions. Any imperfection in the linear stage would corrupt the measurement.
- The IL should not degrade under the X-ray radiation, as this would make the effect non reproducible.

During the first beamtime, the alignment error between both positions of the translational stage was assumed to be constant. It was thus decided to use a fixed correction factor between the two positions. The correction was applied to the sample using the piezoelectric tilt stage. The correction factor was determined with the one time use of an autocollimator after sample installation to measure the difference in alignment of the sample in the two positions. For the second beamtime, the chamber was modified so as to add the capability to measure the alignment error between the two positions after each movement of the linear stage with the autocollimator, and adjust the correction of the tilt stage accordingly. In figure 5.8b the autocollimator can be clearly seen on the left. A simple optical path consisting of a few mirrors, a beam splitter and a shutter allows to sequentially measure the angular offset in two different planes. This information can then be fed to the controller of the tilt stage to perfectly compensate misalignment effects due to the linear stage imperfection or due to the torque applied by the weight of the sample stage to the actuator stack that varies with the orientation of the chamber on the goniometer.

During the first beamtime, the tilt stage broke. For this reason, instead of comparing two sides of a sample exposed to a different polarity, we started observing one point on the sample while switching the polarity of the applied gate voltage. For each point along the Bragg rod, the procedure was to apply the gate voltage V_g during 30s and then measure the diffracted intensity by integrating the image over 30s. The next step was to switch the applied voltage to $-V_g$, let the EDLC charge during 30s, and then again integrate the diffracted intensity over 30s. The differential signal was the difference between these two intensities. In an initial measurement using the IL DEME-TFSI, a clear signal was visible during the first 4h of the measurement but then vanished. After cleaning the sample, a visible mass attached to the sample at the point of incidence of the X-ray beam showed that DEME-TFSI is not resistant enough to radiation damage for this experiment. (See figure 5.6) We then changed to another IL, BMIM-Tf₂N. In this case, we were able to observe a nice repeatable signal after several hours of switching gate voltage under X-ray exposure. This showed us that the signal to noise ratio of the differential diffracted intensity was sufficient to allow for a measurement. But it was later reported that BMIM-Tf₂N when exposed to a constant gate voltage over hours and to a high intensity X-ray beam could damage samples (personal communication from Dr. Hua Zhou). It seems that this effect was not visible in our experiment due to the regular switching of the polarity of V_g .

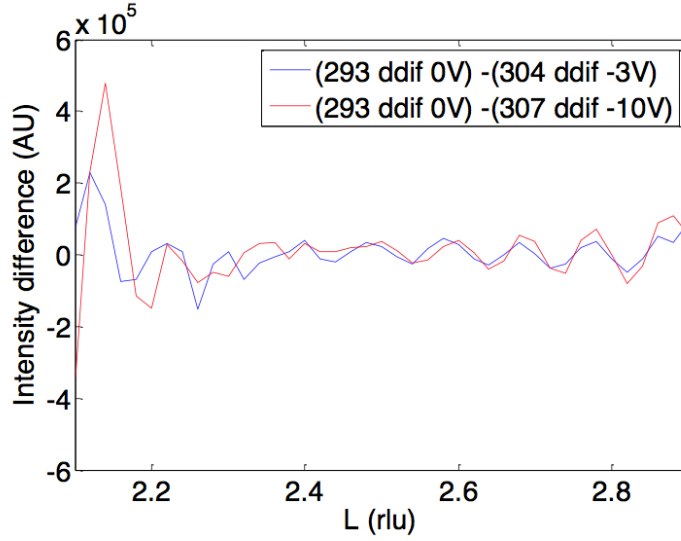


Figure 5.11 – Differential diffracted intensity along a fraction of the $[00L]$ Bragg rod. Difference between diffracted intensity at 0V and $-3V$ (blue), and the difference between 0V and $-10V$ (red).

For the second beamtime, the linear actuator and tilt stage worked as designed. The experimental concept was modified slightly as instead of applying the gate voltage between the two sides of the sample, one of the sides was kept floating while the other side was exposed to a gate voltage applied between the sample and a platinum wire gate. We experimented with two IL, EMIM-DCA and BMIM-PF₆. While the first one behaved nicely, the second one started etching a hole into LaSrAlO₄ immediately upon exposure to gate voltage and X-ray. (See figure 5.10)

During the second beamtime, we took data along a few Bragg rods for different voltages, but were limited by time constraints. While this set of data is insufficient to reconstruct the atomic structure and 3D electron density of the films, it is still a significant preliminary result that indicates that we observe a significant signal and that this measurement is technically feasible. Each gate voltage was applied over a few hours in order to reach a stable point, before the diffraction measurement along a Bragg rod was started. This is a significantly longer charging time than the 30s used during the first beamtime.

5.3.3 Concluding Remarks

While further work is needed in order to resolve the response of the 3 dimensional structure in La_{2-x}Sr_xCuO₄ under high electric field induced by dielectric gating, some significant progress has been made. The radiochemistry of IL in a EDLG configuration showed itself to be quite complex. We had to try several different IL before finding one behaving in a satisfactory manner (EMIM-DCA). Some IL interact directly with the

high intensity X-ray, by polymerising after a few hours exposure to the full intensity beam. This was the case for DEME-TFSI, the IL we had used in most of our cryogenic measurements. Other IL interact only when exposed simultaneously to the gate voltage and the X-ray beam. This gate voltage controlled radiochemistry can be hidden if the voltage applied is reverted regularly. This was the case with BMIM-Tf₂N, that behaved nicely when the gate voltage was inverted every minute, but proved to be attacking the films when the gate voltage was kept constant. Finally, another liquid, BMIM-PF₆, directly started etching into the film and the substrate as soon as it was exposed to the X-ray beam.

In summary:

- We can see a clear signal (See figure 5.11) that shows some change in the structure of the film in response to the EDLG. While our measurements did not give us sufficient data to draw any conclusion about on what is actually happening to the film at the interface with the IL, it is nevertheless a very promising preliminary result that the signal is measurable with our current technique.
- We have found a new IL that has only minimal effect on La_{2-x}Sr_xCuO₄ when exposed over days to X-ray while a gate voltage is applied: EMIM-DCA.
- The custom electrochemical cell developed for our second beamtime worked as expected. But the actual experimental use showed some potential improvements that could be implemented in a next generation of devices. This will allow much easier measurements in future experiments.

6 Conclusions and Outlook

6.1 Conclusions

High temperature superconductivity is still not completely understood. While in recent years the discovery of pnictides[8], a whole new family of iron based high temperature superconducting compounds, has widely opened the field, it is amazing that there is still so much that can be learned from $\text{La}_{2-x}\text{Sr}_x\text{CuO}_4$, a cuprate with a relatively low T_c of around 40 K in single crystals. Working with ultra thin films we succeeded to use the novel technique of electrolyte gating to tune these samples through the superconductor-to-insulator transition. It is striking that a material can be changed from a perfect insulator to a superconductor with a T_c of more than 30K. This is orders of magnitude better than what had been done before. One of the main technical difficulties with this method is the requirement for a single crystal with a surface as perfect as possible. It is also important to note that in the case where we can assume a true physical field effect being at play, only the top most layer of the material is active. For this reason any contamination or dead layer is an impediment to the full deployment of the capacity of the field.

Specifically, our key findings are:

1. The EDLG technique was successfully adapted to high- T_c cuprates, and specifically to $\text{La}_{2-x}\text{Sr}_x\text{CuO}_4$ thin films grown by MBE.
2. Shifts in T_c of up to 30K were induced in these $\text{La}_{2-x}\text{Sr}_x\text{CuO}_4$ films, reversibly driving their state from insulator to superconductor. This allowed preliminary scaling studies that should be extended to lower temperatures.
3. We have seen evidence of a quantum critical point at the underdoped end of the superconducting dome where we observe the quantum resistance for pairs: $R_Q = \frac{h}{(2e)^2} = 6.45\text{k}\Omega$. Similar values have been measured independently by other groups.

4. We extended our studies to other quasi-2D systems: graphene, WO_3 , diamond, FeTe ... and these studies are still very much in progress. However, they already allowed us to make a tremendous progress in understanding the subtleties on how to apply EDLG to a variety of samples, and how to make high quality contacts. This also resulted in several improvements of experimental setups that significantly ease further research.
5. We have also developed a method to apply Coherent Bragg Rod Analysis (COBRA) to our MBE grown $\text{La}_{2-x}\text{Sr}_x\text{CuO}_4$ samples while they are exposed to EDLG. This should eventually allow us to directly determine the effect of EDLG on the $\text{La}_{2-x}\text{Sr}_x\text{CuO}_4$ crystalline structure. Initial results are promising and experiments are still ongoing.

Our results opened a multiplicity of new questions, hence I will now discuss some further research possibilities.

6.2 Outlook for Future Studies

As it is often the case in science, the questions we answered in this work generated a flurry of new questions. From the work on $\text{La}_{2-x}\text{Sr}_x\text{CuO}_4$, observing the critical point on the underdoped side of the superconducting dome using the ionic liquid gating technique brought with it the first obvious avenue: exploring the behaviour of $\text{La}_{2-x}\text{Sr}_x\text{CuO}_4$ around this critical point at sub Kelvin temperatures. While I attempted this during the work for this thesis, various experimental difficulties did not allow for a successful experiment. On the same subject, the next prime experiment that begs to be done is a repetition of the exploration around this critical point without the use of the ionic liquid gating technique. The nicest way to do this would be to use a combinatorial MBE growth technique.[99, 120] Instead of taking a single device and tuning it from insulator to superconductor, it would require growing a single crystal thin film with a strontium doping gradient of up to 4%. While this approach allows a smaller doping range on a single substrate, the main advantage is that it would allow to work with films of greater thickness, and also allow to bury the films under a protective layer so not to be too sensitive to surface related defects. A further avenue that was not studied during this thesis was the Hall effect around this critical point. The instruments and techniques we developed are now ready, and this would be a logical next step.

A simpler next step would be to extend the doping capability of EDLG on $\text{La}_{2-x}\text{Sr}_x\text{CuO}_4$. Now that we have made significant progress with the contacts, it is worth trying to develop a sample structure that will allow to cover the whole superconducting dome from underdoped insulator, to overdoped metal in one single sample. Further more, it would be interesting to combine on these same samples EDLG with conventional back-gating. The later has the advantage that it can be changed at low temperatures. It would thus

be possible to approach the critical point using the EDLG, and then leave the sample at a low temperature while fine tuning it using the back-gate.

A completely different avenue to pursue is the study of how the ionic liquid field effect actually changes the doping in $\text{La}_{2-x}\text{Sr}_x\text{CuO}_4$. There may be significant effects on the crystal structure of the material that have not yet been included in the current simplified models. This is the work that we initiated in our COBRA experiments, and that needs completion. It is important to note the the ionic liquid gating technique can have quite different physical effects depending on the material studied, as it has been shown in the case of vanadium dioxide (VO_2), where “electrolyte gating [...] leads not to electrostatically induced carriers but instead to the electric field-induced creation of oxygen vacancies, with consequent migration of oxygen from the oxide film into the ionic liquid.”[84]

On the front of electrolyte doping of new materials, tungsten oxide (WO_3) was our most promising result, even if it showed no sign of superconductivity. This metal-to-insulator transition opens doped WO_3 to further studies. With the various recent results from other groups this confirms the power of the EDLG method as a new way to dope thin film materials.

Finally there may be some nice surprising results that could arise from the application of the electrolyte gating technique on electron doped superconductors. Also there may be some promise in in-situ deposition of the gate ionic liquid immediately after the growth, while the sample is still in vacuum. This would insure the most perfect possible interface between the gate and the film that needs to be studied.

A Ultra-Stabilization of a Cryocooler

During the experimental work for this thesis, it became rapidly apparent that the use of a closed cycle cryogenic system could have numerous advantages. One important point is that the automated dipstick setups described in chapter 2.2 have a relatively heavy consumption of liquid helium; approximately 1.5 to 2.5 dewars per week when used continuously to cycle samples between 4K and 200K as necessary for the EDLG using the IL DEME-TFSI as gate dielectric. This consumption is even more important when working with gate dielectrics with a higher melting point such as PEG-NaF (melting point of $\sim 300\text{K}$). A closed system would thus be interesting in terms of the economic savings possible once there is no need to buy multiple dewars of liquid helium each week. This economic cost of helium is a particularly important factor at BNL, where we do not have access to a recovery system comparable to the one installed at EPFL. Furthermore a closed system has the advantage that there is no need to plan helium consumption in advance, thus it allows for much more flexibility in its use.^a

Helium with its boiling point of 4.2K at ambient pressure, allows an easy and convenient access to cryogenic temperatures. While it is the second-most abundant element in the universe after hydrogen, it is a rare element on Earth (0.00052% in the atmosphere), as it is too light an element to be trapped on Earth[121]. It is usually co-extracted during natural gas production, where it can represent up to 7% in volume. In the last years, a helium shortage started to appear. While this is due to different economic and political reasons, it is important for scientists that depend on this element to try to reduce this dependence as much as possible. It has been reported that scientists already had to interrupt experiments for days due to this shortage.[122]

While for most cryogenic results presented earlier, we used several dipsticks, a Gifford-McMahon (GM) cryocooler was commissioned. This type of cryocooler is rapidly becoming an interesting alternative to direct liquid helium dipping, as it reliably reaches temperatures of less than 3K. But their intrinsic temperature oscillation of up to 1 K in certain

^a This appendix is adapted from Dubuis, He *et al.*, to be published.

Appendix A. Ultra-Stabilization of a Cryocooler

temperature ranges related to the GM cycle make them less than optimal in situations where temperature stability is critical. These oscillations are amplified for more powerful models that allow faster cooling from room temperature to base temperature. While reducing the cooling power of the cryocooler would reduce these temperature oscillations, this is obviously not an optimal solution when the cooling power is actually needed. For our application, where we want to take transport measurements over the whole temperature range from 4K to room temperature to study superconducting samples, solving this thermal oscillation issue was absolutely critical. Otherwise a cryocooler based system could simply not be considered.

Prior attempts to stabilize such systems can be divided in four categories based on added thermal resistance[123], rare earth alloys[124], pressurized helium vessel[125–127] and long conduction path[128, 129]. Among these concepts, only the last one has reached a commercial application and is currently manufactured by Montana Instruments. The company claims <10mK stability, with the possibility to reach about 1mK. However, this approach needs a specially designed cryocooler, and is unfit for retrofitting on an existing system. According to the patent[129], the thermal damping structure is significantly more complicated than our approach. This results in a commercial product that is significantly more expensive (90'000 \$) than a regular cryocooler (15'000 to 30'000 \$).

Hasegawa *et al.* use two stages of fiber-reinforced plastic dampers to reach peak-to-peak fluctuations of $\sim 2\text{mK}$, but at a cost of highly reduced cooling power, resulting in 6 hours of cooling time from 300K to 4.2K (compared to $< 2.5\text{h}$ with our approach), the need of a second radiation shield also adds complexity and reduces usable sample space.[123] Allwein *et al.* used an Erbium Nickel rare earth alloy plate to reach 14mK fluctuation at 4.2K. This results in fluctuations more than 10 times higher than our approach, and the alloy used is not commonly available.[124] Several groups[125–127] used variations on the idea of a closed helium pot attached to the cold head where the liquefied helium adds thermal capacity to the system. These approaches can yield a thermal stability of up to 10mK, but at the cost of working with a complex highly pressurized gas system (200kPa to 9MPa). They require advanced safety precautions, yielding only a limited time of operation ($\sim 30\text{min}$) or their stabilizing effects are limited to a small operational temperature range ($< 10\text{K}$).

A.1 Technical Realization

The system we present here is a very simple device that damps the temperature oscillations to less than 1mK in the temperature range from 4K to 300K without paying the price of a major increase in base temperature or reduction of cooling power (0.2W at 4K). Our main goal was to stabilize our cryocooler to the point where it could at least be useful for rough characterisation measurements. A first naive attempt was to increase the mass of copper attached to the sample holder on the cold head. Since copper has no significant heat capacity at low temperature this was a futile attempt, but it showed a promising idea: let's find an analogy to a mechanical damper. We also played with various isolating spacers between the cold head and the sample stage. Attempts to actively stabilise the temperature by rapid PID settings were precluded as the sampling frequency of the temperature controller of 20Hz is not fast enough to control the thermal oscillation of the cold head at ~ 1.2 Hz. While this helped with the thermal stability, the resulting increase in base temperature was not acceptable. Then we had a breakthrough idea: let's use the jump in heat capacity in a superconductor at the critical temperature. Since the maximum thermal oscillations appeared at around 5 to 15K, this is the temperature range of T_c that limited our choice of materials. So in the next attempt, using a 1mm niobium plate between the cold head and the copper sample stage was a complete failure. This time the temperature was stabilized to the point where the sample stage was unable to approach a reasonable base temperature of 5K even several hours after the cold head itself had reached its base temperature of ~ 2.9 K. We continued experimenting with other material combinations, directly working on the system without any advanced modeling. Finally a lead based multilayer gave us our *Eureka* moment.

This approach consists of a combination of thin sheets of different materials with contrasting properties: lead, stainless steel and copper. It may be possible to obtain better properties with other materials, but the results were good enough to satisfy our requirement so that we stopped the investigation. We create a thermal buffer block that is placed between the cold head and the sample stage. This buffer acts as a low pass filter for the heat transfer between the sample and the cold head. For temperature control, a heater driven by a commercial temperature controller (LakeShore 340) is mounted on the sample stage. The cryocooler we used is on a 2 stage GM cryocooler from ULVAC technologies Inc., a UR4K03 cold head combined with a C10 compressor, running on 60Hz power. The vacuum enclosure was pumped down to less than $4 \cdot 10^{-6}$ mbar.

In details, for this particular buffer, we combined a number of lead discs with high thermal capacity at low temperature (10 discs, 0.55mm thick) of a diameter equal to the diameter of the cold head (50mm in our instrument). These give a significantly increased thermal mass at low temperature to the buffer. The thermal conductivity is given by adding a continuous ribbon of highly conductive material (such as copper, 12mm wide and 0.03mm thick) that is folded so as to zigzag in between the lead discs. This copper ribbon allows to adjust the thermal conductivity independently from the thermal capacity

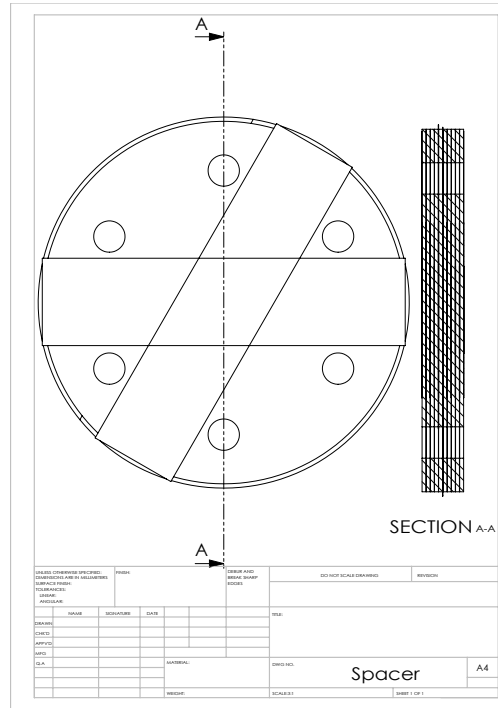


Figure A.1 – Engineering drawing of the damping device.

given by the lead plates. For the final stabilization, we insert partial discs of stainless steel as thermal insulators in the stack. By forcing the heat flow to follow a zigzag path through the stack, from the sample stage to the cold head, along the copper ribbon but around the insulator sheets, we increase the effective distance between the cold head and the sample stage. This renders the heat flow constant despite large temperature oscillations in the cold head. By increasing the number of insulating sheets the stability can be even further increased at the cost of an increased base temperature. In our case, the optimal stack includes 2 sheets of stainless steel as insulator (**0.05mm** thick), 2 copper ribbons and 10 lead discs. See figure A.1 for a technical drawing and figure A.2 for a 3D rendering of the stabilizer. In figure A.3 the stabilizing device installed on the cryocooler is shown. The total dimensions of the cylindrical buffer stack are **5.9mm** in height and **50mm** in diameter. This is significantly smaller than the available sample space (**55mm** height and **50mm** diameter). This gives us 3 degrees of freedom (lead and steel plates, as well as copper ribbon) that can be independently adjusted to optimize the 2 variables: heat capacitance and conductance to achieve optimal base temperature and thermal stability. We can do fine adjustments by varying the force applied to the stack, using a torque wrench to tighten the screws holding the sample stage to the cold head and compressing the stack.

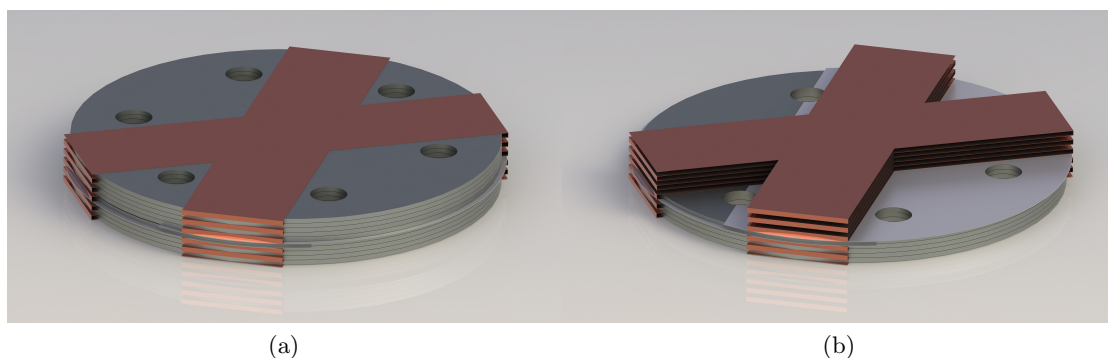


Figure A.2 – 3D rendered drawing of the damping device (a), and of the partial damping device to demonstrate the position of one of the stainless steel spacers in the stack of lead plates (b). In red color the two copper ribbons zigzagging through the stack are shown.

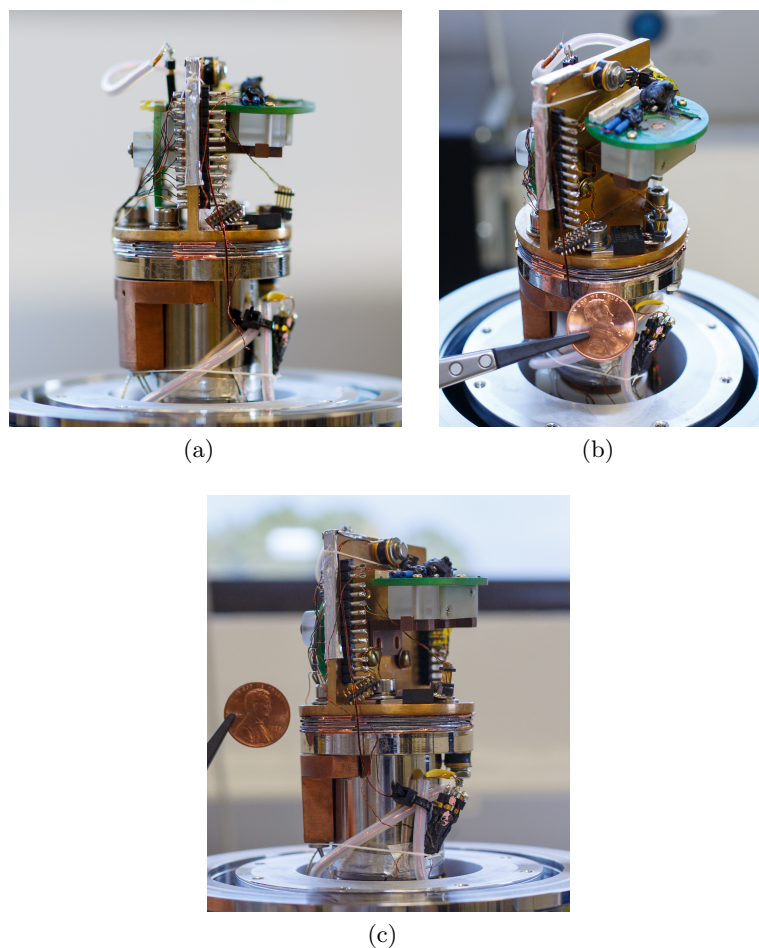


Figure A.3 – Several pictures of the stabilization device installed on our cryocooler. It is installed between the cold head (Chrome plated, on bottom) and the sample holder (Gold plated, on top). Photo credit: Dr. Xi He.

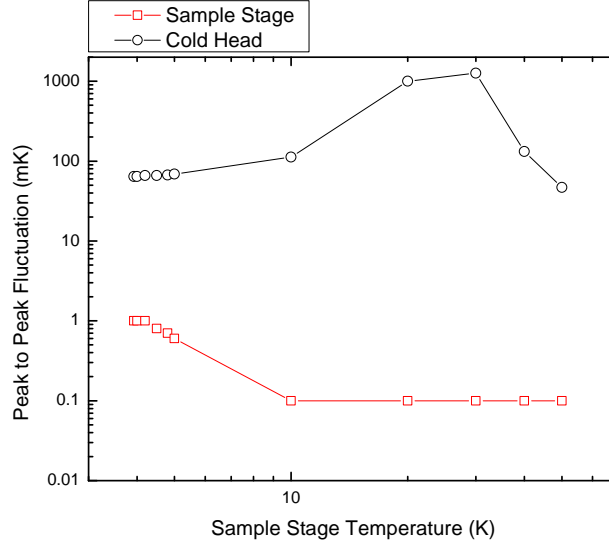


Figure A.4 – Maximal temperature uncertainty envelope of the cryogenic system as function of sample stage temperature. One sees that the thermal oscillations of the sample stage are maximal near the base temperature of 3.9K, and then gradually decrease. Above 10K, 0.1mK oscillation amplitude is a conservative estimate as due to the digitisation noise of the temperature controller we cannot measure temperature differences of less than 1mK. The cold head temperature peak to peak variation shows a dampening effect of 2 orders of magnitude (40dB). Without the damping device, the sample stage temperature and thus its uncertainty envelope is similar to the cold head temperature.

A.2 Experimental Results

After installation of our thermal buffer, we observed a dramatically improved thermal stability of the sample stage with oscillations of less than 1mK over the whole thermal range from $< 4\text{K}$ to 300K . (See figure A.4) At the same time the cooling power was preserved. This results in an initial cooling time from 300K to 4.2K of less than 2.5 hours. After this initial cool down, further thermal cycles controlled by the heater can be more rapid as the thermal shield attached to the first stage of the cryocooler is already at its operating temperature. Figures A.5 shows the damping of the thermal oscillations along the whole temperature range. If the PID controller is used to control the heater, extremely constant cooling rates can be achieved as it is demonstrated in figure A.6. To exactly quantify the effectiveness of our damping device, we stabilized the temperature with the PID controller at different points. Before installation of the damper, the temperatures of the cold head and the sample stage were quasi identical. Installing the damping device also did not change the amplitude of the thermal oscillations of the cold head. This cold head temperature can be used as a good estimation of the sample stage temperature before installing the thermal damper. Figures A.7 and A.8 clearly show the damping behaviour for a few typical points over the temperature range.

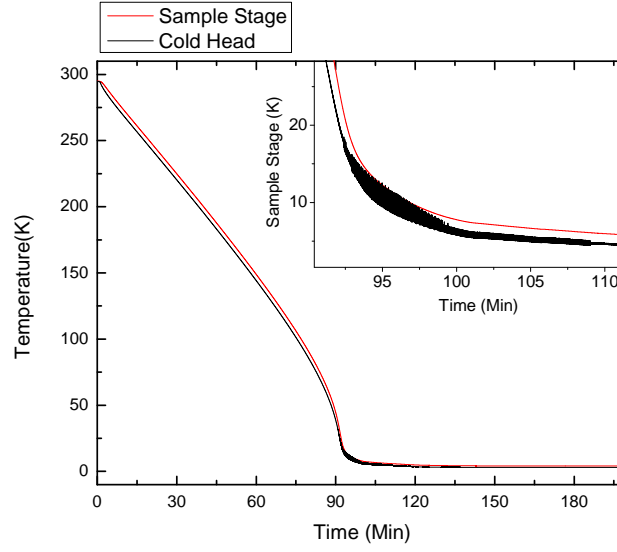


Figure A.5 – Typical initial cooling behaviour of the system. The cold head temperature is slightly lower, and has a zone of high temperature oscillations between 8 and 15 Kelvin, whereas the sample temperature shows no sign of oscillation. The inset shows the zone of maximal temperature instability of the cold head (second stage of the cryocooler), in contrast to the smooth cooling observed on the sample.

A.3 Conclusion

With a very simple device, we were able to dramatically improve the thermal stability of a commercial closed cycle cryocooler. In light of the helium shortage experienced by researchers worldwide, this is a crucial discovery as it notably expands the number of cryogenic experiments that can be performed using a closed cycle system. In our case, this will help us in our transport characterisation measurements. Especially the highly improved control of the cooling rate will allow even better quality of data. It can be assumed that similar cryocoolers with improved thermal stability can be of use for many scientific experiments that need stable cryogenic temperatures.

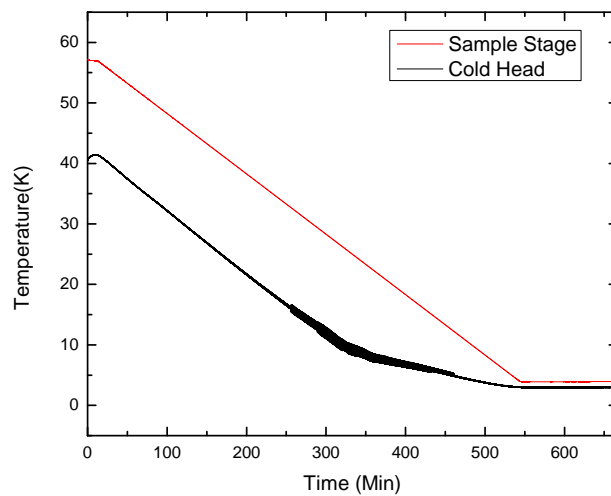
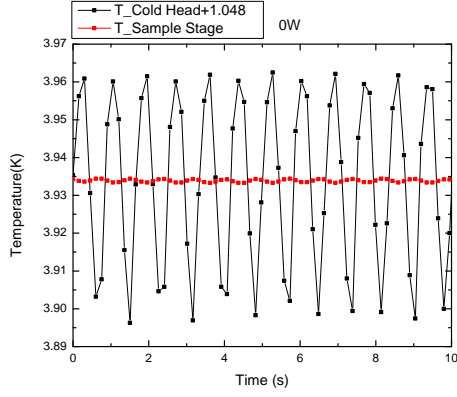
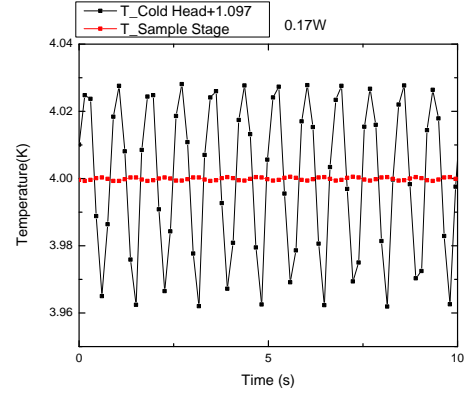


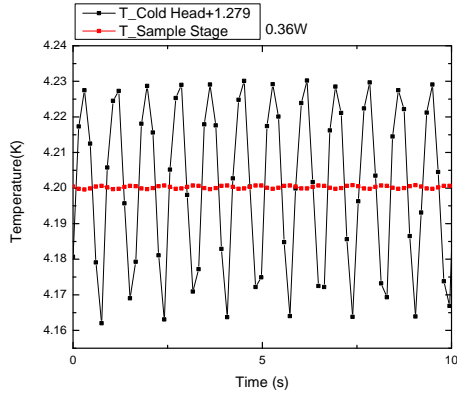
Figure A.6 – In our experiments, we regularly ramp the temperature through a wide range. Here we show how the PID controlled heater, in combination with our stabilized cold head is able to keep a perfectly constant ramping rate while the cold head temperature is oscillating at a frequency of 1.2 Hz, with a particularly significant amplitude in the range between 8 and 15 Kelvin.



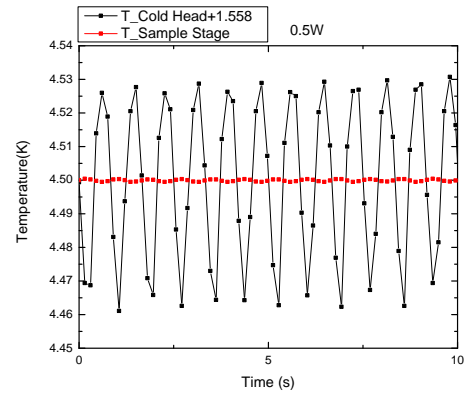
(a) Set temperature: 3.93 K



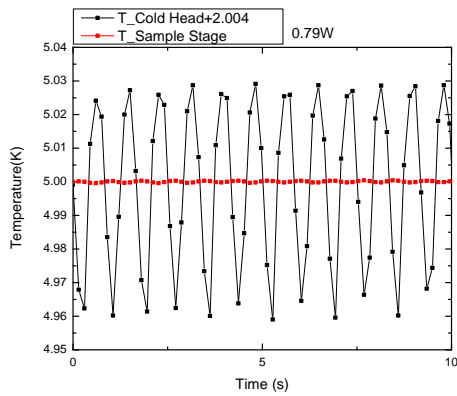
(b) Set temperature: 4 K



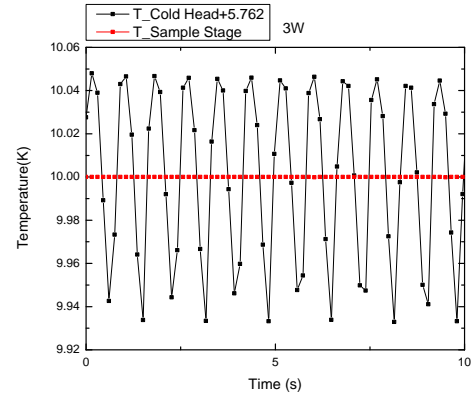
(c) Set temperature: 4.2 K



(d) Set temperature: 4.5 K



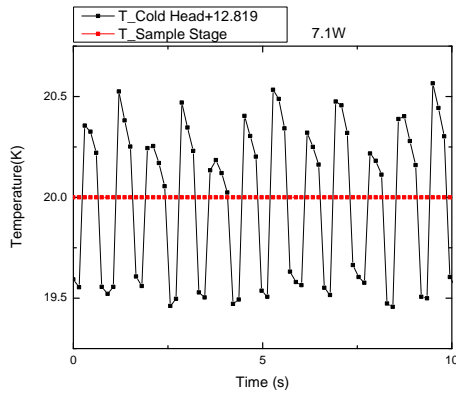
(e) Set temperature: 5 K



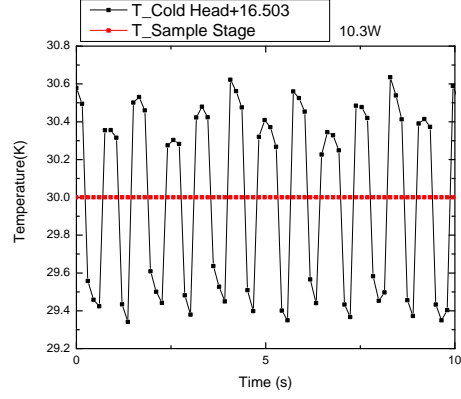
(f) Set temperature: 10 K

Figure A.7 – Damping of the temperature oscillation on the sample stage compared to the cold head temperature for various set sample stage temperatures. The red curve shows the sample stage temperature, while the black curve represents the cold head temperature plus an arbitrary constant in order to fit on the same scale. Panels (a) to (f) show different set temperatures from base temperature to 10 K. For temperatures above 10 K, one sees the digitisation noise, as the temperature controller's resolution is limited to only 6 digits (1 mK for $T \geq 10$ K, 0.1 mK for $T < 10$ K).

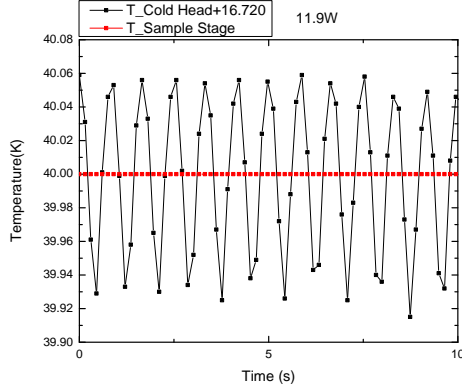
Appendix A. Ultra-Stabilization of a Cryocooler



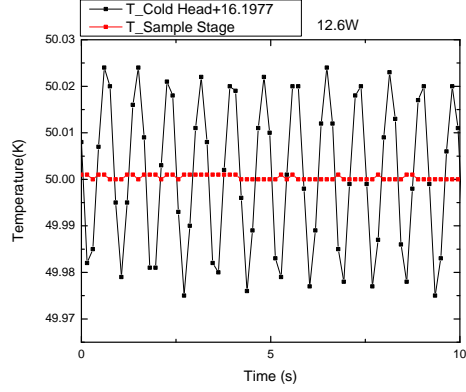
(a) Set temperature: 20K



(b) Set temperature: 30K



(c) Set temperature: 40K



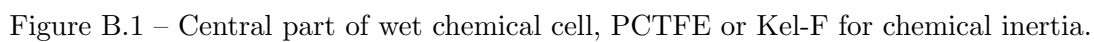
(d) Set temperature: 50K

Figure A.8 – Damping of the temperature oscillation on the sample stage compared to the cold head temperature for various set sample stage temperatures. The red curve shows the sample stage temperature, while the black curve represents the cold head temperature plus an arbitrary constant in order to fit on the same scale. Panels (a) to (d) show different set temperatures from 20K to 50K. For temperatures above 10K, one sees the digitisation noise, as the temperature controller's resolution is limited to only 6 digits (1mK for $T \geq 10$ K, 0.1mK for $T < 10$ K).

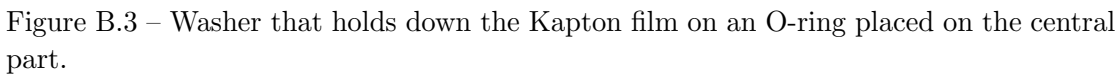
B Wet Chemical Cell: Drawings

In this appendix we present some of the technical drawings related to the design of the wet chemical cell described in 5.3.1.

78



80



Bibliography

- [1] A. T. Bollinger, G. Dubuis, J. Yoon, D. Pavuna, J. Misewich, and I. Božović, “Superconductor-insulator transition in $\text{La}_{2-x}\text{Sr}_x\text{CuO}_4$ at the pair quantum resistance,” *Nature*, vol. 472, no. 7344, pp. 458–460, Apr. 2011.
- [2] A. T. Bollinger, J. N. Eckstein, G. Dubuis, D. Pavuna, and I. Božović, “Atomic-Layer Engineering of Oxide Superconductors,” *Proc. SPIE*, vol. 8263, p. 82631C, Feb. 2012.
- [3] G. Dubuis, A. T. Bollinger, D. Pavuna, and I. Božović, “Electric field effect on superconductivity in $\text{La}_{2-x}\text{Sr}_x\text{CuO}_4$,” *Journal of Applied Physics*, vol. 111, no. 11, p. 112632, Jun. 2012.
- [4] G. Dubuis, A. T. Bollinger, D. Pavuna, and I. Božović, “On field effect studies and superconductor-insulator transition in high- T_c cuprates,” *The European Physical Journal Special Topics*, vol. 222, no. 5, pp. 1217–1221, Jul. 2013.
- [5] G. Dubuis, A. T. Bollinger, D. Pavuna, and I. Božović, “Critical Resistance at the Superconductor-Insulator Transition in Hole-Doped Cuprates,” *Journal of Superconductivity and Novel Magnetism*, vol. 26, no. 4, pp. 749–754, Apr. 2013.
- [6] R. J. Cohn, “Record superconductor at 22.3 K,” *Physics Today*, vol. 26, no. 10, pp. 17–18, Oct. 1973.
- [7] J. R. Gavaler, “Superconductivity in Nb-Ge films above 22 K*,” *Applied Physics Letters*, vol. 23, no. 8, p. 480, Oct. 1973.
- [8] Y. Kamihara, H. Hiramatsu, M. Hirano, R. Kawamura, H. Yanagi, T. Kamiya, and H. Hosono, “Iron-Based Layered Superconductor: LaOFeP ,” *Journal of the American Chemical Society*, vol. 128, no. 31, pp. 10012–10013, Aug. 2006.
- [9] D. van Delft and P. Kes, “The discovery of superconductivity,” *Physics Today*, vol. 63, no. 9, pp. 38–43, Sep. 2010.
- [10] W. Meissner and R. Ochsenfeld, “Ein neuer Effekt bei Eintritt der Supraleitfähigkeit,” *Die Naturwissenschaften*, vol. 21, no. 44, pp. 787–788, Nov. 1933.

Bibliography

- [11] H. Kamerlingh Onnes, "Further experiments with Liquid Helium G. On the electrical resistance of Pure Metals etc. VI. On the Sudden Change in the Rate at which the Resistance of Mercury Disappears," *Koninklijke Nederlandse Akademie van Wetenschappen Proceedings Series B Physical Sciences*, vol. 14 II, no. 1911-1912, pp. 818–821, 1912.
- [12] F. London and H. London, "The Electromagnetic Equations of the Supraconductor," *Proceedings of the Royal Society of London. Series A - Mathematical and Physical Sciences*, vol. 149, no. 866, pp. 71–88, Mar. 1935.
- [13] J. Bardeen, L. N. Cooper, and J. R. Schrieffer, "Theory of Superconductivity," *Physical Review*, vol. 108, no. 5, pp. 1175–1204, Dec. 1957.
- [14] N. Barišić, M. K. Chan, Y. Li, G. Yu, X. Zhao, M. Dressel, A. Smontara, and M. Greven, "Universal sheet resistance and revised phase diagram of the cuprate high-temperature superconductors," *Proceedings of the National Academy of Sciences of the United States of America*, vol. 110, no. 30, pp. 12 235–12 240, Jul. 2013.
- [15] M. Oda, N. Momono, and M. Ido, "Electronic phase diagram of $\text{La}_{2-x}\text{Sr}_x\text{CuO}_4$," *Journal of Physics and Chemistry of Solids*, vol. 65, no. 8-9, pp. 1381–1390, Aug. 2004.
- [16] I. Božović, G. Y. Logvenov, I. Belca, B. Narimbetov, and I. Sveklo, "Epitaxial Strain and Superconductivity in $\text{La}_{2-x}\text{Sr}_x\text{CuO}_4$ Thin Films," *Physical Review Letters*, vol. 89, no. 10, p. 107001, Aug. 2002.
- [17] C. H. Ahn, J.-M. Triscone, and J. Mannhart, "Electric field effect in correlated oxide systems," *Nature*, vol. 424, no. 6952, pp. 1015–1018, Aug. 2003.
- [18] J. E. Lilienfeld, "Method and apparatus for controlling electric currents," U.S. Patent US1 745 175 A, Jan., 1930.
- [19] The Nobel Prize in Physics 1956. [Online]. Available: http://www.nobelprize.org/nobel_prizes/physics/laureates/1956/index.html
- [20] H. von Helmholtz, "Ueber einige Gesetze der Vertheilung elektrischer Ströme in körperlichen Leitern mit Anwendung auf die thierisch-elektrischen Versuche," *Annalen der Physik*, vol. 165, no. 6, pp. 211–233, 1853.
- [21] H. von Helmholtz, "Ueber einige Gesetze der Vertheilung elektrischer Ströme in körperlichen Leitern, mit Anwendung auf die thierisch-elektrischen Versuche (Schluss.)," *Annalen der Physik*, vol. 165, no. 7, pp. 353–377, 1853.
- [22] K. B. Oldham, "A Gouy–Chapman–Stern model of the double layer at a (metal)/(ionic liquid) interface," *Journal of Electroanalytical Chemistry*, vol. 613, no. 2, pp. 131–138, Feb. 2008.

- [23] A. A. Kornyshev, "Double-Layer in Ionic Liquids: Paradigm Change?" *Journal of Physical Chemistry B*, vol. 111, no. 20, pp. 5545–5557, May 2007.
- [24] R. Atkin and G. G. Warr, "Structure in Confined Room-Temperature Ionic Liquids," *The Journal of Physical Chemistry C*, vol. 111, no. 13, pp. 5162–5168, Apr. 2007.
- [25] R. Hayes, N. Borisenko, M. K. Tam, P. C. Howlett, F. Endres, and R. Atkin, "Double Layer Structure of Ionic Liquids at the Au(111) Electrode Interface: An Atomic Force Microscopy Investigation," *The Journal of Physical Chemistry C*, vol. 115, no. 14, pp. 6855–6863, Apr. 2011.
- [26] H. Zhou, M. Rouha, G. Feng, S. S. Lee, H. Docherty, P. Fenter, P. T. Cummings, P. F. Fulvio, S. Dai, J. McDonough, V. Presser, and Y. Gogotsi, "Nanoscale Perturbations of Room Temperature Ionic Liquid Structure at Charged and Uncharged Interfaces," *ACS Nano*, vol. 6, no. 11, pp. 9818–9827, Oct. 2012.
- [27] I. Engelhardt, R. Speck, J. Inche, H. S. Khalil, M. Ebert, W. J. Lorenz, G. Saemann-Ischenko, and M. W. Breiter, "Low-Temperature Electrochemistry on High T_c Superconductors," in *Electrochimica Acta*. Univ Erlangen Nurnberg, Inst Phys, W-8520 Erlangen, Germany, 1992, pp. 2129–2136.
- [28] S. R. Peck, L. S. Curtin, J. T. McDevitt, R. W. Murray, J. P. Collman, W. A. Little, T. Zetterer, H. M. Duan, C. Dong, and A. M. Hermann, "Response of the Double-Layer Capacitance of a High-Temperature Superconductor/Fluid Electrolyte Interface to the Onset of Superconductivity," *Journal of the American Chemical Society*, vol. 114, no. 17, pp. 6771–6775, 1992.
- [29] S. G. Haupt, D. R. Riley, J. Zhao, and J. T. McDevitt, "Contact Resistance Measurements Recorded at Conductive Polymer High-Temperature Superconductor Interfaces," *Journal of Physical Chemistry*, vol. 97, no. 30, pp. 7796–7799, 1993.
- [30] S. G. Haupt, D. R. Riley, C. T. Jones, J. Zhao, and J. T. McDevitt, "Reversible Modulation of T_c in Conductive Polymer/High Temperature Superconductor Assemblies," *Journal of the American Chemical Society*, vol. 115, pp. 1196–1198, 1993.
- [31] S. G. Haupt, D. R. Riley, and J. T. McDevitt, "Conductive polymer/high-temperature superconductor composite structures," *Advanced Materials*, vol. 5, no. 10, pp. 755–758, Oct. 1993.
- [32] J. T. McDevitt, D. R. Riley, and S. G. Haupt, "Electrochemistry of high-temperature superconductors. Challenges and opportunities," *Analytical Chemistry*, vol. 65, no. 11, pp. 535–545, 1993.
- [33] S. J. Green, D. R. Rosseinsky, and D. C. Sinclair, "A liquid-electrolyte voltammetric probe of superconducting oxocuprates through the transition temperature T_c ,"

Bibliography

- Journal of the Chemical Society, Chemical Communications*, no. 12, pp. 1421–1422, 1994.
- [34] S. G. Haupt, D. R. Riley, J. Zhao, J.-P. Zhou, J. H. Grassi, and J. T. McDevitt, “Reversible modulation of superconductivity in $\text{YBa}_2\text{Cu}_3\text{O}_{7-\delta}$ /polypyrrole sandwich structures,” *Proc. SPIE*, vol. 2158, pp. 238–249, 1994.
- [35] S. G. Haupt, D. R. Riley, J. H. Grassi, R.-K. Lo, J. Zhao, J.-P. Zhou, and J. T. McDevitt, “Preparation and Characterization of $\text{YBa}_2\text{Cu}_3\text{O}_{7-\delta}$ /Polypyrrole Bilayer Structures,” *Journal of the American Chemical Society*, vol. 116, no. 22, pp. 9979–9986, 1994.
- [36] J. C. Phillips, “Charge transfer and superconductor-metal-insulator transitions in high- T_c superconductors,” *Physical Review B*, vol. 51, no. 21, pp. 15 402–15 406, Jun. 1995.
- [37] M. B. Clevenger, C. E. Jones, S. G. Haupt, J. Zhao, and J. T. McDevitt, “Organic conductor/high- T_c superconductor bilayer structures,” *Proc. SPIE*, vol. 2697, pp. 508–519, 1996.
- [38] R.-K. Lo, J. E. Ritchie, J.-P. Zhou, J. Zhao, J. T. McDevitt, F. Xu, and C. A. Mirkin, “Polypyrrole growth on $\text{YBa}_2\text{Cu}_3\text{O}_{7-\delta}$ modified with a self-assembled monolayer of *N*-(3-aminopropyl)pyrrole: Hardwiring the “electroactive hot spots” on a superconductor electrode,” *Journal of the American Chemical Society*, vol. 118, no. 45, pp. 11 295–11 296, 1996.
- [39] J. T. McDevitt, C. A. Mirkin, R.-K. Lo, K. Chen, J.-P. Zhou, F. Xu, S. G. Haupt, J. Zhao, and D. C. Jurbergs, “Molecular Level Control over the Surface and Interfacial Properties of High- T_c Superconductors,” *Chemistry of materials*, vol. 8, no. 4, pp. 811–813, 1996.
- [40] J. T. McDevitt, J. E. Ritchie, M. B. Clevenger, R.-K. Lo, J.-P. Zhou, and C. A. Mirkin, “Molecular engineering of organic conductor/high- T_c superconductor assemblies,” *Synthetic metals*, vol. 84, no. 1-3, pp. 407–408, 1997.
- [41] J. T. McDevitt, C. E. Jones, S. G. Haupt, J. Zhao, and R.-K. Lo, “Conductive polymer/high- T_c superconductor bilayer structures,” *Synthetic metals*, vol. 85, no. 1-3, pp. 1319–1322, 1997.
- [42] S. J. Green, D. R. Rosseinsky, D. R. Rosseinsky, A. L. Kharlanov, and J. P. Attfield, “A new probe of superconductivity: quantitative measurements on defined electron transfer with solute at the interface between liquid electrolyte and oxocuprate electrode in the superconducting state,” *Chemical Communications*, no. 11, pp. 1215–1216, 1998.
- [43] J. E. Ritchie, W. R. Murray, K. Kershan, V. Diaz, L. Tran, and J. T. McDevitt, “Surface Cleaning and Adsorbate Layer Formation: Dual Role of Alkylamines in the

- Formation of Self-Assembled Monolayers on Cuprate Superconductors,” *Journal of the American Chemical Society*, vol. 121, no. 32, pp. 7447–7448, 1999.
- [44] H. Shimotani, H. Asanuma, A. Tsukazaki, A. Ohtomo, M. Kawasaki, and Y. Iwasa, “Insulator-to-metal transition in ZnO by electric double layer gating,” *Applied Physics Letters*, vol. 91, no. 8, p. 082106, Aug. 2007.
- [45] K. Ueno, S. Nakamura, H. Shimotani, A. Ohtomo, N. Kimura, T. Nojima, H. Aoki, Y. Iwasa, and M. Kawasaki, “Electric-field-induced superconductivity in an insulator,” *Nature Materials*, vol. 7, pp. 855–858, Nov. 2008.
- [46] M. Kimata, T. Ishihara, and H. Tajima, “Electrostatic Charge Carrier Injection into the Charge-Ordered Organic Material α -(BEDT-TTF) $_2$ I $_3$,” *Journal of the Physical Society of Japan*, vol. 81, no. 7, p. 073704, Jun. 2012.
- [47] R. Atkin, S. Z. E. Abedin, R. Hayes, L. H. S. Gasparotto, N. Borisenko, and F. Endres, “AFM and STM Studies on the Surface Interaction of [BMP]TFSA and [EMIm]TFSA Ionic Liquids with Au(111),” *The Journal of Physical Chemistry C*, vol. 113, no. 30, pp. 13 266–13 272, Jul. 2009.
- [48] J. G. Checkelsky, J. Ye, Y. Onose, Y. Iwasa, and Y. Tokura, “Dirac-fermion-mediated ferromagnetism in a topological insulator,” *Nature Phys.*, vol. 8, pp. 729–733, Aug. 2012.
- [49] S. Shimizu, R. Yoshimi, T. Hatano, K. S. Takahashi, A. Tsukazaki, M. Kawasaki, Y. Iwasa, and Y. Tokura, “Gate control of surface transport in MBE-grown topological insulator (Bi $_{1-x}$ Sb $_x$) $_2$ Te $_3$ thin films,” *Physical Review B*, vol. 86, no. 4, p. 045319, Jul. 2012.
- [50] Y. Onose, R. Yoshimi, A. Tsukazaki, H. Yuan, T. Hidaka, Y. Iwasa, M. Kawasaki, and Y. Tokura, “Pulsed Laser Deposition and Ionic Liquid Gate Control of Epitaxial Bi $_2$ Se $_3$ Thin Films,” *Applied Physics Express*, vol. 4, no. 8, p. 083001, Jul. 2011.
- [51] P. Zareapour, A. Hayat, S. Y. F. Zhao, M. Kreshchuk, A. Jain, D. C. Kwok, N. Lee, S.-W. Cheong, Z. Xu, A. Yang, G. D. Gu, S. Jia, R. J. Cava, and K. S. Burch, “Proximity-induced high-temperature superconductivity in the topological insulators Bi $_2$ Se $_3$ and Bi $_2$ Te $_3$,” *Nature Communications*, vol. 3, p. 1056, Sep. 2012.
- [52] J. Ye, Y. J. Zhang, Y. Kasahara, and Y. Iwasa, “Interface transport properties in ion-gated nano-sheets,” *The European Physical Journal Special Topics*, vol. 222, no. 5, pp. 1185–1201, Jul. 2013.
- [53] H. Yuan, H. Liu, H. Shimotani, H. Guo, M. Chen, Q. Xue, and Y. Iwasa, “Liquid-Gated Ambipolar Transport in Ultrathin Films of a Topological Insulator Bi $_2$ Te $_3$,” *Nano letters*, vol. 11, no. 7, pp. 2601–2605, Jul. 2011.

- [54] K. Segawa, Z. Ren, S. Sasaki, T. Tsuda, S. Kuwabata, and Y. Ando, “Ambipolar transport in bulk crystals of a topological insulator by gating with ionic liquid,” *Physical Review B*, vol. 86, no. 7, p. 075306, Aug. 2012.
- [55] K. Shimamura, D. Chiba, S. Ono, S. Fukami, N. Ishiwata, M. Kawaguchi, K. Kobayashi, and T. Ono, “Electrical control of Curie temperature in cobalt using an ionic liquid film,” *Applied Physics Letters*, vol. 100, no. 12, p. 122402, Mar. 2012.
- [56] M. Dankerl, M. V. Hauf, M. Stutzmann, and J. A. Garrido, “Diamond solution-gated field effect transistors: Properties and bioelectronic applications,” *Physica Status Solidi A: Application and Materials science*, vol. 209, no. 9, pp. 1631–1642, Aug. 2012.
- [57] M. Dankerl, M. Tosun, M. Stutzmann, and J. A. Garrido, “Solid polyelectrolyte-gated surface conductive diamond field effect transistors,” *Applied Physics Letters*, vol. 100, no. 2, p. 023510, Jan. 2012.
- [58] M. Endo, D. Chiba, H. Shimotani, F. Matsukura, Y. Iwasa, and H. Ohno, “Electric double layer transistor with a (Ga,Mn)As channel,” *Applied Physics Letters*, vol. 96, no. 2, p. 022515, Jan. 2010.
- [59] F. Chen, Q. Qing, J. Xia, J. Li, and N. Tao, “Electrochemical Gate-Controlled Charge Transport in Graphene in Ionic Liquid and Aqueous Solution,” *Journal of the American Chemical Society*, vol. 131, no. 29, pp. 9908–9909, Jul. 2009.
- [60] Y. Sui and J. Appenzeller, “Screening and Interlayer Coupling in Multilayer Graphene Field-Effect Transistors,” *Nano letters*, vol. 9, no. 8, pp. 2973–2977, Aug. 2009.
- [61] E. Uesugi, H. Goto, R. Eguchi, A. Fujiwara, and Y. Kubozono, “Electric double-layer capacitance between an ionic liquid and few-layer graphene,” *Scientific Reports*, vol. 3, p. 1595, Apr. 2013.
- [62] A. Allain, Z. Han, and V. Bouchiat, “Electrical control of the superconducting-to-insulating transition in graphene–metal hybrids,” *Nature Materials*, vol. 11, no. 7, pp. 590–594, Jul. 2012.
- [63] R. Misra, M. McCarthy, and A. F. Hebard, “Electric field gating with ionic liquids,” *Applied Physics Letters*, vol. 90, p. 052905, Jan. 2007.
- [64] K. Ueno, S. Nakamura, H. Shimotani, H. Yuan, N. Kimura, T. Nojima, H. Aoki, Y. Iwasa, and M. Kawasaki, “Discovery of superconductivity in KTaO_3 by electrostatic carrier doping,” *Nature Nanotechnology*, vol. 6, no. 7, pp. 408–412, Jun. 2011.

-
- [65] A. S. Dhoot, I. Casey, X. Moya, N. D. Mathur, and R. H. Friend, “Large electric field effect in electrolyte-gated manganites,” *Physical Review Letters*, vol. 102, no. 13, p. 136402, Mar. 2009.
- [66] J. Garcia-Barriocanal, A. Kobrinskii, X. Leng, J. Kinney, B. Yang, S. Snyder, and A. M. Goldman, “Electronically driven superconductor-insulator transition in electrostatically doped $\text{La}_2\text{CuO}_{4+\delta}$ thin films,” *Physical Review B*, vol. 87, no. 2, p. 024509, Jan. 2013.
- [67] A. K. Mishra, A. J. Darbandi, P. M. Leufke, R. Kruk, and H. Hahn, “Room temperature reversible tuning of magnetism of electrolyte-gated $\text{La}_{0.75}\text{Sr}_{0.25}\text{MnO}_3$ nanoparticles,” *Journal of Applied Physics*, vol. 113, no. 3, p. 033913, Jan. 2013.
- [68] J. Ye, Y. J. Zhang, R. Akashi, M. S. Bahramy, R. Arita, and Y. Iwasa, “Superconducting Dome in a Gate-Tuned Band Insulator,” *Science*, vol. 338, no. 6111, pp. 1193–1196, Nov. 2012.
- [69] K. Taniguchi, A. Matsumoto, H. Shimotani, and H. Takagi, “Electric-field-induced superconductivity at 9.4 K in a layered transition metal disulphide MoS_2 ,” *Applied Physics Letters*, vol. 101, no. 4, p. 042603, Jul. 2012.
- [70] S. Asanuma, P.-H. Xiang, H. Yamada, H. Sato, I. H. Inoue, H. Akoh, A. Sawa, K. Ueno, H. Shimotani, H. Yuan, M. Kawasaki, and Y. Iwasa, “Tuning of the metal-insulator transition in electrolyte-gated NdNiO_3 thin films,” *Applied Physics Letters*, vol. 97, p. 142110, Oct. 2010.
- [71] R. Scherwitzl, P. Zubko, I. G. Lezama, S. Ono, A. F. Morpurgo, G. Catalan, and J.-M. Triscone, “Electric-Field Control of the Metal-Insulator Transition in Ultrathin NdNiO_3 Films,” *Advanced Materials*, vol. 22, no. 48, pp. 5517–5520, Oct. 2010.
- [72] T. Hatano, Y. Ogimoto, N. Ogawa, M. Nakano, S. Ono, Y. Tomioka, K. Miyano, Y. Iwasa, and Y. Tokura, “Gate Control of Electronic Phases in a Quarter-Filled Manganite,” *Scientific Reports*, vol. 3, p. 2904, Oct. 2013.
- [73] S. Ono, S. Seki, R. Hirahara, Y. Tominari, and J. Takeya, “High-mobility, low-power, and fast-switching organic field-effect transistors with ionic liquids,” *Applied Physics Letters*, vol. 92, no. 10, p. 103313, Mar. 2008.
- [74] A. Tardella and J.-N. Chazalviel, “Highly accumulated electron layer at a semiconductor electrolyte interface,” *Physical Review B*, vol. 32, no. 4, pp. 2439–2448, Aug. 1985.
- [75] H. Benisty, P. Colomban, and J.-N. Chazalviel, “Electron accumulation layer at n -Si/non-liquid electrolyte interfaces,” *Applied Physics Letters*, vol. 51, no. 14, pp. 1121–1123, Aug. 1987.

- [76] T. Yanase, T. Shimada, and T. Hasegawa, "Electric Double Layer Gate Field-Effect Transistors Based on Si," *Japanese Journal Of Applied Physics*, vol. 49, no. 4, p. 04DK06, Apr. 2010.
- [77] P.-H. Xiang, S. Asanuma, H. Yamada, H. Sato, I. H. Inoue, H. Akoh, A. Sawa, M. Kawasaki, and Y. Iwasa, "Electrolyte-Gated SmCoO_3 Thin-Film Transistors Exhibiting Thickness-Dependent Large Switching Ratio at Room Temperature," *Advanced Materials*, vol. 25, no. 15, pp. 2158–2161, Feb. 2013.
- [78] H. Yuan, M. Toh, K. Morimoto, W. Tan, F. Wei, H. Shimotani, C. Kloc, and Y. Iwasa, "Liquid-gated electric-double-layer transistor on layered metal dichalcogenide, SnS_2 ," *Applied Physics Letters*, vol. 98, no. 1, p. 012102, Jan. 2011.
- [79] K. Ueno, H. Shimotani, Y. Iwasa, and M. Kawasaki, "Electrostatic charge accumulation versus electrochemical doping in SrTiO_3 electric double layer transistors," *Applied Physics Letters*, vol. 96, no. 25, p. 252107, Jun. 2010.
- [80] M. Li, W. Han, X. Jiang, J. Jeong, M. G. Samant, and S. S. P. Parkin, "Suppression of Ionic Liquid Gate-Induced Metallization of $\text{SrTiO}_3(001)$ by Oxygen," *Nano letters*, vol. 13, no. 10, pp. 4675–4678, Oct. 2013.
- [81] S. S. P. Parkin, T. D. Schladt, T. Graf, M. Li, N. Aetukuri, X. Jiang, and M. Samant, "Electrolyte Gate Induced Metallization of Several Facets (101, 001, 110 and 100) of Rutile TiO_2 and (001) SrTiO_3 ," in *Frontiers in Electronic Materials: A Collection of Extended Abstracts of the Nature Conference Frontiers in Electronic Materials, June 17 to 20 2012, Aachen, Germany*, J. Heber, D. G. Schlom, Y. Tokura, R. Waser, and M. Wuttig, Eds. Weinheim, Germany: Wiley-VCH Verlag GmbH & Co. KGaA, Apr. 2013, pp. 42–43.
- [82] T. D. Schladt, T. Graf, N. B. Aetukuri, M. Li, A. Fantini, X. Jiang, M. G. Samant, and S. S. P. Parkin, "Crystal-Facet-Dependent Metallization in Electrolyte-Gated Rutile TiO_2 Single Crystals," *ACS Nano*, vol. 7, no. 9, pp. 8074–8081, Sep. 2013.
- [83] Y. Yamada, K. Ueno, T. Fukumura, H. Yuan, H. Shimotani, Y. Iwasa, L. Gu, S. Tsukimoto, Y. Ikuhara, and M. Kawasaki, "Electrically Induced Ferromagnetism at Room Temperature in Cobalt-Doped Titanium Dioxide," *Science*, vol. 332, no. 6033, pp. 1065–1067, May 2011.
- [84] J. Jeong, N. Aetukuri, T. Graf, T. D. Schladt, M. G. Samant, and S. S. P. Parkin, "Suppression of Metal-Insulator Transition in VO_2 by Electric Field-Induced Oxygen Vacancy Formation," *Science*, vol. 339, no. 6126, pp. 1402–1405, Mar. 2013.
- [85] M. Nakano, K. Shibuya, D. Okuyama, T. Hatano, S. Ono, M. Kawasaki, Y. Iwasa, and Y. Tokura, "Collective bulk carrier delocalization driven by electrostatic surface charge accumulation," *Nature*, vol. 487, no. 7408, pp. 459–462, Jul. 2012.

-
- [86] M. Nakano, K. Shibuya, N. Ogawa, T. Hatano, M. Kawasaki, Y. Iwasa, and Y. Tokura, "Infrared-sensitive electrochromic device based on VO_2 ," *Applied Physics Letters*, vol. 103, no. 15, p. 153503, Oct. 2013.
- [87] X. Leng, J. Garcia-Barriocanal, S. Bose, Y. Lee, and A. M. Goldman, "Electrostatic Control of the Evolution from a Superconducting Phase to an Insulating Phase in Ultrathin $\text{YBa}_2\text{CaCu}_3\text{O}_{7-x}$ Films," *Physical Review Letters*, vol. 107, no. 2, p. 027001, Jul. 2011.
- [88] T. Nojima, H. Tada, S. Nakamura, N. Kobayashi, H. Shimotani, and Y. Iwasa, "Hole reduction and electron accumulation in $\text{YBa}_2\text{Cu}_3\text{O}_y$ thin films using an electrochemical technique: Evidence for an n -type metallic state," *Physical Review B*, vol. 84, no. 2, p. 020502, Jul. 2011.
- [89] A. S. Dhoot, S. C. Wimbush, T. Benseman, J. L. MacManus-Driscoll, J. R. Cooper, and R. H. Friend, "Increased T_c in Electrolyte-Gated Cuprates," *Advanced Materials*, vol. 22, no. 23, pp. 2529–2533, May 2010.
- [90] J. Ye, S. Inoue, K. Kobayashi, Y. Kasahara, H. Yuan, H. Shimotani, and Y. Iwasa, "Gate induced superconductivity in layered material based electronic double layer field effect transistors," *Physica C: Superconductivity and its applications*, vol. 470, no. Supplement 1, pp. S682–S684, Oct. 2009.
- [91] Y. Kasahara, T. Nishijima, T. Sato, Y. Takeuchi, J. Ye, H. Yuan, H. Shimotani, and Y. Iwasa, "Electric-Field-Induced Superconductivity Detected by Magnetization Measurements of an Electric-Double-Layer Capacitor," *Journal of the Physical Society of Japan*, vol. 80, no. 2, p. 023708, Feb. 2011.
- [92] J. Ye, S. Inoue, K. Kobayashi, Y. Kasahara, H. Yuan, H. Shimotani, and Y. Iwasa, "Liquid-gated interface superconductivity on an atomically flat film," *Nature Materials*, vol. 9, no. 2, pp. 125–128, Feb. 2010.
- [93] J. Ye, Y. J. Zhang, Y. Matsushashi, M. F. Craciun, S. Russo, Y. Kasahara, A. F. Morpurgo, and Y. Iwasa, "Gate-Induced Superconductivity in Layered-Material-Based Electric Double Layer Transistors," *Chinese Physics C*, vol. 400, no. 2, p. 022139, Dec. 2012.
- [94] H. Yuan, H. Shimotani, A. Tsukazaki, A. Ohtomo, M. Kawasaki, and Y. Iwasa, "High-Density Carrier Accumulation in ZnO Field-Effect Transistors Gated by Electric Double Layers of Ionic Liquids," *Advanced Functional Materials*, vol. 19, no. 7, pp. 1046–1053, Feb. 2009.
- [95] H. Yuan, H. Shimotani, A. Tsukazaki, A. Ohtomo, M. Kawasaki, and Y. Iwasa, "Hydrogenation-Induced Surface Polarity Recognition and Proton Memory Behavior at Protic-Ionic-Liquid/Oxide Electric-Double-Layer Interfaces," *Journal of the American Chemical Society*, vol. 132, no. 19, pp. 6672–6678, Apr. 2010.

Bibliography

- [96] A. M. Gozar, G. Y. Logvenov, L. F. Kourkoutis, A. T. Bollinger, L. A. Gianuzzi, D. A. Muller, and I. Božović, “High-temperature interface superconductivity between metallic and insulating copper oxides,” *Nature*, vol. 455, no. 7214, pp. 782–785, Oct. 2008.
- [97] G. Y. Logvenov, A. M. Gozar, and I. Božović, “High-Temperature Superconductivity in a Single Copper-Oxygen Plane,” *Science*, vol. 326, no. 5953, pp. 699–702, Oct. 2009.
- [98] S. Smadici, J. C. T. Lee, S. Wang, P. Abbamonte, G. Y. Logvenov, A. M. Gozar, C. Deville Cavellin, and I. Božović, “Superconducting Transition at 38 K in Insulating-Overdoped La_2CuO_4 - $\text{La}_{1.64}\text{Sr}_{0.36}\text{CuO}_4$ Superlattices: Evidence for Interface Electronic Redistribution from Resonant Soft X-Ray Scattering,” *Physical Review Letters*, vol. 102, no. 10, p. 107004, Mar. 2009.
- [99] I. Božović, “Atomic-Layer Engineering of Superconducting Oxides: *Yesterday, Today, Tomorrow*,” *IEEE Transactions on Applied Superconductivity*, vol. 11, no. 1, pp. 2686–2695, Mar. 2001.
- [100] J. A. Clayhold, O. Pelleg, A. T. Bollinger, G. Y. Logvenov, B. M. Kerns, M. D. Schroer, D. W. Rench, and I. Božović, “Statistical Characterization and Process Control for Improved Growth of $\text{La}_{2-x}\text{Sr}_x\text{CuO}_4$ Films,” *Journal of Superconductivity and Novel Magnetism*, vol. 22, no. 8, pp. 797–804, Jun. 2009.
- [101] N. Liu, F. Luo, H. Wu, Y. Liu, C. Zhang, and J. Chen, “One-Step Ionic-Liquid-Assisted Electrochemical Synthesis of Ionic-Liquid-Functionalized Graphene Sheets Directly from Graphite,” *Advanced Functional Materials*, vol. 18, no. 10, pp. 1518–1525, May 2008.
- [102] O. Aschenbrenner, S. Supasitmongkol, M. Taylor, and P. Styring, “Measurement of vapour pressures of ionic liquids and other low vapour pressure solvents,” *Green Chemistry*, vol. 11, no. 8, pp. 1217–1221, Jun. 2009.
- [103] N. Marković, C. Christiansen, A. M. Mack, W. H. Huber, and A. M. Goldman, “Superconductor-insulator transition in two dimensions,” *Physical Review B*, vol. 60, no. 6, pp. 4320–4328, Aug. 1999.
- [104] A. F. Hebard and M. A. Paalanen, “Magnetic-Field-Tuned Superconductor-Insulator Transition in Two-Dimensional Films,” *Physical Review Letters*, vol. 65, no. 7, pp. 927–930, Aug. 1990.
- [105] D. J. C. Walker, A. P. Mackenzie, and J. R. Cooper, “Transport properties of zinc-doped $\text{YBa}_2\text{Cu}_3\text{O}_{7-\delta}$ thin films,” *Physical Review B*, vol. 51, no. 21, pp. 15 653–15 656, Jun. 1995.

-
- [106] D. Mandrus, L. Forró, C. Kendziora, and L. Mihaly, “Two-dimensional electron localization in bulk single-crystals of $\text{Bi}_2\text{Sr}_2\text{Y}_x\text{Ca}_{1-x}\text{Cu}_2\text{O}_8$,” *Physical Review B*, vol. 44, no. 5, pp. 2418–2421, Aug. 1991.
- [107] S. Oh, T. A. Crane, D. J. Van Harlingen, and J. N. Eckstein, “Doping Controlled Superconductor-Insulator Transition in $\text{Bi}_2\text{Sr}_{2-x}\text{La}_x\text{CaCu}_2\text{O}_{8+\delta}$,” *Physical Review Letters*, vol. 96, no. 10, p. 107003, Mar. 2006.
- [108] S. V. Borisenko, A. A. Kordyuk, S. Legner, T. K. Kim, M. Knupfer, C. M. Schneider, J. Fink, M. S. Golden, M. Sing, R. Claessen, A. Yaresko, H. Berger, C. Grazioli, and S. Turchini, “Circular dichroism and bilayer splitting in the normal state of underdoped $(\text{Pb,Bi})_2\text{Sr}_2(\text{Ca}_x\text{Y}_{1-x})\text{Cu}_2\text{O}_{8+\delta}$ and overdoped $(\text{Pb,Bi})_2\text{Sr}_2\text{CaCu}_2\text{O}_{8+\delta}$,” *Physical Review B*, vol. 69, no. 22, p. 224509, Jun. 2004.
- [109] K. Semba and A. Matsuda, “Superconductor-to-Insulator Transition and Transport Properties of Underdoped $\text{YBa}_2\text{Cu}_3\text{O}_y$ Crystals,” *Physical Review Letters*, vol. 86, no. 3, pp. 496–499, Jan. 2001.
- [110] Y.-D. Chuang, A. D. Gromko, A. V. Fedorov, Y. Aiura, K. Oka, Y. Ando, M. Lindroos, R. S. Markiewicz, A. Bansil, and D. S. Dessau, “Bilayer splitting and coherence effects in optimal and underdoped $\text{Bi}_2\text{Sr}_2\text{CaCu}_2\text{O}_{8+\delta}$,” *Physical Review B*, vol. 69, no. 9, p. 094515, Mar. 2004.
- [111] C. J. Raub, A. E. Sweedler, M. A. Jensen, S. Broadston, and B. T. Matthias, “Superconductivity of Sodium Tungsten Bronzes,” *Physical Review Letters*, vol. 13, no. 25, pp. 746–747, Dec. 1964.
- [112] S. Reich and Y. Tsabba, “Possible nucleation of a 2D superconducting phase on WO_3 single crystals surface doped with Na^+ ,” *European Physical Journal B: Condensed Matter and Complex Systems*, vol. 9, no. 1, pp. 1–4, May 1999.
- [113] A. Shengelaya, S. Reich, Y. Tsabba, and K. A. Müller, “Electron spin resonance and magnetic susceptibility suggest superconductivity in Na doped WO_3 samples,” *European Physical Journal B: Condensed Matter and Complex Systems*, vol. 12, no. 1, pp. 13–15, Oct. 1999.
- [114] S. Reich, G. Leitus, R. Popovitz-Biro, A. Goldbourt, and S. Vega, “A Possible 2D H_xWO_3 Superconductor with a T_c of 120 K,” *Journal of Superconductivity and Novel Magnetism*, vol. 22, no. 4, pp. 343–346, May 2009.
- [115] T. Sato, G. Masuda, and K. Takagi, “Electrochemical properties of novel ionic liquids for electric double layer capacitor applications,” *Electrochimica Acta*, vol. 49, no. 21, pp. 3603–3611, May 2004.
- [116] M. Galiński, A. Lewandowski, and I. Stępnia, “Ionic liquids as electrolytes,” *Electrochimica Acta*, vol. 51, no. 26, pp. 5567–5580, Apr. 2006.

Bibliography

- [117] B. Skinner, M. S. Loth, and B. I. Shklovskii, “Capacitance of the Double Layer Formed at the Metal/Ionic-Conductor Interface: How Large Can It Be?” *Physical Review Letters*, vol. 104, no. 12, p. 128302, Mar. 2010.
- [118] H. Zhou, Y. Yacoby, V. Y. Butko, G. Y. Logvenov, I. Božović, and R. Pindak, “Anomalous expansion of the copper-apical-oxygen distance in superconducting cuprate bilayers,” *Proceedings of the National Academy of Sciences of the United States of America*, vol. 107, no. 18, pp. 8103–8107, May 2010.
- [119] Y. Yacoby, H. Zhou, R. Pindak, and I. Božović, “Atomic-layer synthesis and imaging uncover broken inversion symmetry in $\text{La}_{2-x}\text{Sr}_x\text{CuO}_4$ films,” *Physical Review B*, vol. 87, no. 1, p. 014108, Jan. 2013.
- [120] J. Wu, O. Pelleg, G. Y. Logvenov, A. T. Bollinger, Y.-J. Sun, G. S. Boebinger, M. Vanević, Z. Radović, and I. Božović, “Anomalous independence of interface superconductivity from carrier density,” *Nature Materials*, vol. 12, no. 10, pp. 877–881, Aug. 2013.
- [121] M. Fernandez, “A Helium Shortage Leads to Fewer Balloons in the Sky,” *The New York Times*, Dec. 2012.
- [122] W. J. Nuttall, R. H. Clarke, and B. A. Glowacki, “Resources: Stop squandering helium,” *Nature*, vol. 485, no. 7400, pp. 573–575, May 2012.
- [123] Y. Hasegawa, D. Nakamura, M. Murata, H. Yamamoto, and T. Komine, “High-precision temperature control and stabilization using a cryocooler,” *Review of Scientific Instruments*, vol. 81, no. 9, p. 094901, Sep. 2010.
- [124] K. Allweins, L. M. Qiu, and G. Thummes, “Damping of intrinsic temperature oscillations in a 4 K pulse tube cooler by means of rare earth plates,” *ADVANCES IN CRYOGENIC ENGINEERING: Transactions of the Cryogenic Engineering Conference - CEC, Vol 52*, vol. 985, pp. 109–116, 2008.
- [125] M. J. Smith and J. Jennings, “Cryogenic Temperature Stabilization of the Daikin 308 Cryocooler,” in *ASME 2011 International Mechanical Engineering Congress & Exposition*. ASME, 2011, pp. 679–684.
- [126] K. Okidono, T. Oota, H. Kurihara, T. Sumida, T. Nishioka, H. Kato, M. Matsumura, and O. Sasaki, “Temperature oscillation suppression of GM cryocooler,” *Journal of Physics: Conference Series*, vol. 400, no. 5, p. 052026, Dec. 2012.
- [127] B. J. Haid, “Helium Pot System for Maintaining Sample Temperature after Cryocooler Deactivation,” in *ADVANCES IN CRYOGENIC ENGINEERING: Transactions of the Cryogenic Engineering Conference - CEC, Vol 52*, Keystone, CO, United States, Aug. 2005, pp. 147–155.

- [128] L. Mauritsen, D. Snow, A. Woidtke, M. Chase, and I. Henslee, “Low Vibration, Low Thermal Fluctuation System for Pulse Tube and GiffordMcMahon Cryocoolers,” in *Cryocoolers 15*, S. D. Miller and R. G. Ross, Eds., Oct. 2008, pp. 581–585.
- [129] D. Snow, M. Chase, A. Woidtke, L. Mauritsen, I. Henslee, P. B. Sellin, and K. Merkel, “Apparatus and methods for improving vibration isolation, thermal dampening, and optical access in cryogenic refrigerators,” U.S. Patent 12/461,529, 2010.



Photographic Credits

Photographic credit for figures 2.4, 5.2, A.3a, A.3b, A.3c : Dr. Xi He.

D.o.B.: 19.8.1981
Nationality: CH (Savièse + Sierre) & D
Marital Status: Single

Dubuis Guy
Rte du stade 5
1974 Arbaz
Switzerland

+41 (0)76 747 5333
guy.dubuis@gmail.com

Résumé

Summary of qualifications

- PhD in physics EPFL, 2 years of non academic work experience.
- Project experience in cryogenics, material research, IT consulting, environmental engineering and polar scientific research.
- Speaking French, German and English.
- Looking for a new challenge at the crossroad of science and industry, in an innovative environment.
- Interested in material physics, climate science, sustainability and renewable energies.



Professional Experience

PhD studies in physics at EPFL, CH and BNL, USA

2009-now

- Developed a method to effectively tune the charge carrier density in thin films resulting in massive changes of the critical temperature in superconducting films. Advanced experience with cryogenics and sensitive electronic characterization measurements.
- Experimental work done at Brookhaven National Laboratory (4 years)

Analyst at Accenture AG, Zurich, CH

2008-2009

- Worked on different internal and client projects. Project experience in reorganization of the IT of a reinsurance company.
- Analyzed the Environmental Impact of Accenture Switzerland, crafted measures to improve it and found savings potential of up to 2 mio. CHF. (16 months)

Physicist at UMTEC Institute, Hochschule für Technik, Rapperswil, CH

2007-08

- Created a Finite Element Model of a viscoelastic flow including dripping. (4 months)

Civil Service at UMTEC Institute, Hochschule für Technik, Rapperswil, CH

2007

- Collaborated to different research project in environmental engineering. (2 months)

Diploma thesis at the University of Alaska, Fairbanks, USA

2006-07

- Studied the physics of sea ice, in the lab and on the field. First mid-term experience in an Anglophone environment. Discovered the effects of climate change on real life. (6 months)

Internship at Paul Scherrer Institut, Villigen, CH

2005

- Analyzed chemical traces in glacier ice cores using mass spectrometry.
- Introduction to climate physics. (2 months)

Organized and led a 1-month class trip in Burkina Faso

2004

- with the NGO Nouvelle Planète. Build and installed solar water heaters in village nursing stations, in interaction and with the participation of members of the local communities.

Education

Master's in physics

2001-07

at Ecole Polytechnique Fédérale in Lausanne, CH

Maturité C (scientific high school diploma), mention bilingual

1996-01

at Lycée Collège des Creusets in Sion, CH

D.o.B.: 19.8.1981
Nationality: CH (Savièse + Sierre) & D
Marital Status: Single

Dubuis Guy
Rte du stade 5
1974 Arbaz
Switzerland

+41 (0)76 747 5333
guy.dubuis@gmail.com

Languages

- Bilingual French and German
- Fluent English (written and spoken)

Computer Skills

LaTeX, Matlab, Mathematica, LabView, COMSOL and common office software

Other Interest

- Music: studied trombone at Conservatoire of Sion and Lausanne and played with a half-dozen music ensembles.
- Sports: Rowing, Sport climbing, Mountaineering, Telemark skiing

Publications

1. Pringle, D. J., Dubuis, G. & Eicken, H. Instruments and Methods Impedance measurements of the complex dielectric permittivity of sea ice at 50 MHz: pore microstructure and potential for salinity monitoring. *J. Glaciol.* **55**, 81–94 (2009).
2. Bollinger, A. T. *et al.* Superconductor-insulator transition in $\text{La}_{2-x}\text{Sr}_x\text{CuO}_4$ at the pair quantum resistance. *Nature* **472**, 458–460 (2011).
3. Bollinger, A. T., Eckstein, J. N., Dubuis, G., Pavuna, D. & Božović, I. Atomic-Layer Engineering of Oxide Superconductors. *Proc. SPIE* **8263**, 82631C (2012).
4. Dubuis, G., Bollinger, A. T., Pavuna, D. & Božović, I. Electric field effect on superconductivity in $\text{La}_{2-x}\text{Sr}_x\text{CuO}_4$. *J. Appl. Phys.* **111**, 112632 (2012).
5. Dubuis, G., Bollinger, A. T., Pavuna, D. & Božović, I. On field effect studies and superconductor-insulator transition in high- T_c cuprates. *Eur. Phys. J. Spec. Top.* **222**, 1217–1221 (2013).
6. Dubuis, G., Bollinger, A. T., Pavuna, D. & Božović, I. Critical Resistance at the Superconductor-Insulator Transition in Hole-Doped Cuprates. *J. Supercond. Novel Magn.* **26**, 749–754 (2013).